Tracking Summer Extra-Tropical Storms:

A Climatological Overview and Variability in the Northern Hemisphere

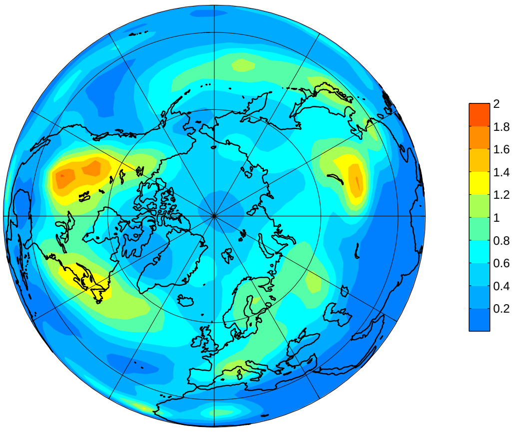

Candidate for a Master's of Science in
Geophysics - Climatology

Michel dos Santos Mesquita
Geophysical Institute, University of Bergen - Norway
May 2006

If nature were not beautiful, it would not be worth studying it. And life would not be worth living.

- Henry Poincare

Acknowledgments

The advisor of this master thesis has been professor Nils Gunnar Kvamstø from the University of Bergen. I would like to thank him for the supervision, the important comments on my work and for the motivation given under my master's degree studies. The co-supervisor has been Dr. Asgeir Sorteberg from the Bjerknes Centre for Climate Research, I would also like to thank him for the help using the different softwares and the dataset, the comments during the research process and during my two presentations at the AGU (American Geophysical Union) in San Francisco 2004/2005.

I would like to thank Dr. David Stephenson, Dr. David Atkinson and MSc. Øyving Byrkjedal for the help and comments related to the storm track theory and the thesis itself.

Special thanks to: Professor Sigbjørn Grønås for the important classes on baroclinic instability, potential vorticity thinking and synoptic meteorology; and the memorable professor Elmer Raustein who introduced me to the dynamics of the atmosphere.

I would like to dedicate this thesis to Mrs. Pedrina dos Santos Mesquita (my mother), to my family in Brazil and to Frank Tessem. Thank you so much for the support during this important journey.

Michel dos Santos Mesquita
4th May 2006
Bergen, Norway

Contents

1 Introduction 1

2 Theory Background 7

2.1 Baroclinic Instability 7

2.2 On the Baroclinic Instability in the Summer 9

2.2.1 The Rayleigh Theorem 9

2.2.2 Some Energy Considerations 11

3 Extra-Tropical Winter Storm Tracks 13

3.1 References 13

3.2 Methods 13

3.2.1 The Definition of Storm Tracks 15

3.2.2 The Dynamics of Storm Tracks 17

3.2.3 Tracking the Storms 18

3.3 Mean Structural and Temporal Characteristics 19

3.4 Geographical Distribution of the Tracks 20

3.5 Relation to the Large-Scale Flow 25

4 Methodology 27

4.1 The Dataset 27

4.2 The Tracking Algorithm 28

4.2.1 Using the Dataset to Track Storms 29

4.2.2 Output from the Tracking Algorithm 30

4.3 Selected Regions 32

4.4 Relation to the Large-Scale Flow 33

5 Climatology 35

5.1 Climatology of the Main Variables 35

5.2 Difference Between Summer and Winter 44

6 Variability 55
6.1 Is the Number of Storms Changing? 55
6.2 Are the Storms Intensifying? 59
6.3 Statistical Modeling of Selected Variables 62
  6.3.1 Pattern Characteristics 63
  6.3.2 Selected Models 68

7 Discussion and Concluding Remarks 83
7.1 Climatology 83
7.2 Variability 84
7.3 Relation to the Large-Scale Flow 86
7.4 Final Remarks 88

A The cost Function 89

B The Normal Probability Plots 91
B.1 Checks for Normality 91
B.2 The Normal Probability Plots 92

C Criteria for Comparing the Regression Models: R^2 and the AIC 97

D Average and Standard Deviation of the Main Variables 99

E Contributions of the Explanatory Variables to the Regression Models 101

F Statistically Significant Regression Models 105
F.1 Track Density Anomaly 105
F.2 Track Intensity 107

Chapter 1

Introduction

Mankind has always worried about the weather, especially when it comes to storms. Before the advent of meteorological studies, storms were seen as something magical and mystical: "To our ancestors,...the coming of rain and snow determined the growth of crops and feed farms. Hail storms could wipe out entire crops and heavy rains could flood farmland for miles. The weather was mysterious and all powerful" (Williams 2002). Hence, myths were created in order to explain this potent phenomenon: "Wind was not only powerful, but unpredictable, changing directions and speed randomly, reflecting anger or the displeasure of the early Gods" (Williams 2002).

Early meteorological studies shed some light on the understanding of cyclones. For example, during the mid-nineteenth century[1], scientists started to classify and plot the individual storms. These plots started when synoptic weather maps were systematically prepared in the 1850s and 1860s (Bergeron 1950; Barry and Carleton 2001). For example, this is seen in an illustration (Figure 1.1) from 1888 of the frequency distribution as viewed at that time (Chang et al. 2002). Figure 1.2 also shows the amount of 'summer hurricanes' from 1887-1923 as reproduced from Bergeron (1950). Other examples of early investigations are the ones performed by H. Mohn (1870) for Norway, E. Loomis (1874) for North America, V. Koppen (1880) and J. van Bebber (1891) for Europe and North America, and Rykachev (1896) for Europe (including European Russia), as reported by Barry and Carleton (2001).

Later on, the famous School of Bergen, a scientific group in the beginning of the twentieth century, revolutionized modern meteorology by introducing the description of the life-cycle of a cyclone: "Only by studying the dynamics of baroclinic motions, is it possible to understand real atmospheric circulations" - this was a powerful sentence in

---

[1] The identification and tracking of storm systems over the tropical oceans began during this time as well. Barry and Carleton (2001) report on important scientists who were engaged in this task, such as W.C. Redfield (1831) who traced the paths of hurricanes, Henry Piddinton (1842) who documented the motion of some tropical storms and who introduced the term *cyclone* (from the Greek *kyklon*, which means revolving). The term *anticyclone* was first introduced by Francis Galton in 1863.

Vilhelm Bjerknes' mind for many years (Grønås 2005). The ideas fundamented by the famous Norwegian meteorologists and also the ones that were part of the Bergen School helped shape modern meteorology to a large extent. Barry and Carleton (2001) point out that the "characteristics and life cycle of frontal cyclones were not described until 1919 by the 'Bergen school' of meteorologists in Norway" and this was also confirmed by Bergeron (1950). Hence, tracking storms effectively is possible due to the concepts of the life-cycle of a cyclone, first introduced by these meteorologists.

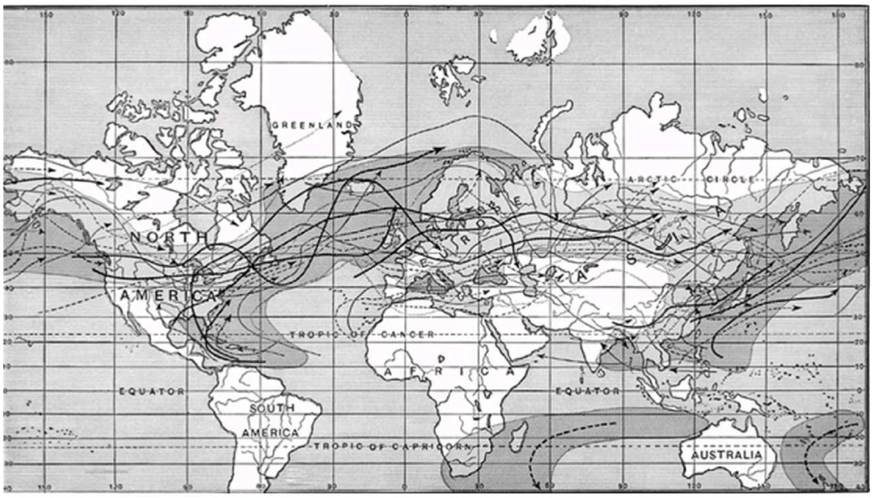

Figure 1.1: *"A figure from an 1888 geography text showing storm frequency distribution as viewed in the mid-nineteenth century. The stipling denotes high storm frequency, while the arrows indicate individual storms. Reproduced from Hinman (1888)." From: Edmund Chang et al. (2002).*

Even though the first to assemble information on cyclone paths over the northern hemisphere was Loomis, in 1885, a comprehensive analysis was only possible in the mid-twentieth century by the papers of Petterssen (1950)[2] and Klein (1957). Thus, from the end of the 19th century to the advent of the computer, storms were tracked by relating their position with time and using statistical methods. Later, with the introduction of the 'Numerical Weather Prediction' (NWP), using gridded analysis and modern computers, a more global approach started being implemented. It applied statistical methods on the synoptic scale through the so-called 'synoptic objective analysis' (Murray and Simmonds 1991; Jones and Simmonds 1993; Serreze et al. 1993; Hoskins and Hodges 2002). This type of analysis made it possible, for example, to employ

---

[2] Barry and Carleton (2001) point out that: "Petterssen drew attention to the importance of the zones where there is a high rate of alternation between high and low-pressure centers, which he termed pressure ducts."

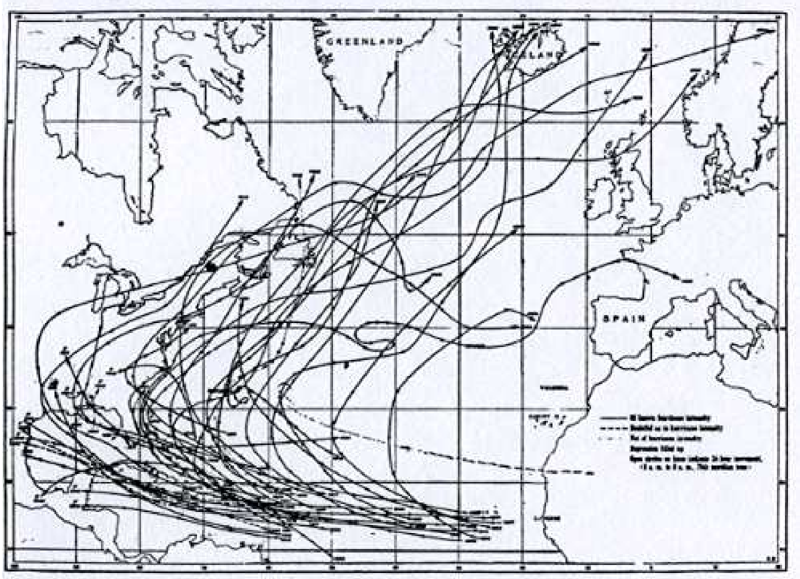

Figure 1.2: *Different plots of hurricane tracks during August from 1887-1923. Reproduced from Bergeron (1950).*

algorithms to identify local minima/maxima within blocks of grid points.

Numerous studies have been conducted related to understanding and describing the behavior of winter storm tracks (Cai and van der Dool 1991; Chang and Orlanski 1992; Gulev et al. 2001; Byrkjedal 2002; Chang et al. 2002; Chang and Fu 2002; Hoskins and Hodges 2002; Chang 2004; Sorteberg et al. 2004), whereas the summer season seems to have been neglected. Why is it so? There are many reasons why the wintertime has been so much researched, perhaps the most important one is related to what human beings perceive or observe in nature: the idea that winter storms are stronger and more numerous. Some scientific facts about winter and summer storms are:

(i) The average pole to equator temperature "gradient in the Northern Hemisphere is much larger in winter than in summer" (Holton 2004);

(ii) Ice-ocean and ocean-air temperature contrasts are weak in summer (Serreze 1995);

(iii) The baroclinicity[3] is enhanced during winter (Chang et al. 2002);

(iv) Summer systems are everywhere quite weak, generally averaging over 995mb, in the Arctic region (Serreze 1995);

---

[3] Refer to Chapter 2 for more information on the baroclinic instability theory.

(v) There is a connection between the winter cyclogenesis and the large-scale flow[4] (Chang et al. 2002; Sorteberg et al. 2004);

(vi) "...the synoptic-scale storm track activity is largest" during the winter (Chang et al. 2002), and many others.

However, the extra-tropical summer storm tracks have not yet been studied so much, there is a void in the literature when it comes to summer storm track research.

Some summer storms have caused serious damage to crop and property, and have acted as dangerous killers as well. A severe summer storm devastated part of the SERC[5] forest in the United States (Smith 2002):

> On the evening of June 5th, 2002, warm summer breezes passed though the SERC forest as the setting sun met a leafy horizon. This peaceful mixed-deciduous forest, however, was about to experience a destructive summer storm. Just before 9 p.m. high winds and heavy rains crashed into the area and quickly passed through. Numerous limbs were torn from trunks and healthy live trees were snapped off or ripped from the ground, leaving large openings in the canopy.

Another example of a summer storm was 'The Fastnet Race Disaster'[6] on August 13-14th, 1979, where many competitors on a yacht race lost their lives due to severe storm (Lamb 1991). In Norway, extra-tropical cyclones have taken many people's lives and destroyed properties, crops and oil platforms. Grønås et al. (1994) report on a storm which numerical models failed to predict: on August 27-28, 1989, "...an unusual mesoscale storm struck the area between Hamburg and Kiel in Germany". This "unexpected" summer storm was of great proportions: 100 mm of precipitation in 24 hours with mean winds more than 25 m/s. These are just some of many cases of the extensive damage caused by extra-tropical summer storms. Lamb (1991) provides other examples of storm records from 1509 to 1990. Table 1.1 summarizes three of the summer storms reported in his book.

Many oil industries, air companies, farms and tourism depend on weather forecasting and climatological studies for their activities throughout a year, the summer season is not an exception. Doing research on the summer season is also important for science: Chang et al. (2002) mentioned that the different characteristics for describing cyclogenesis "...remains a topic of extreme relevance to the science and practice of weather forecasting" (Chang et al. 2002). Hence, the aim of this research is to study the extra-

---

[4] For example, according to (Chang et al. 2002), storm tracks are important for the maintenance of the extra-tropical westerlies against surface dissipation.

[5] SERC is an acronym for the Smithsonian Environmental Research Center.

[6] See table 1.1 for more information.

Table 1.1: Examples of severe summer storms. From Lamb (1991).

Date	Area	Meteorology	Extra Information
29 July 1956	Southern England and Wales and the Channel.	Storm caused by a depression, which had been centred near 47°N 28°W. It deepened below 980 mb as it advanced. (See figure 1.3).	"...at least 500 trees, bushes and foliage" were damaged near the south coast. This storm was described as a " ...violent gale which cost many lives in shipwrecks and caused widespread damage inland in Southern Britain."
23-25 August 1957	The British Isles, near-lying waters, the whole southern North Sea, southern Danish waters and the southwest Baltic.	The depression centre of 998mb deepened to 965mb. "Coalescence of lows from different origins" (Lamb 1991).	Widespread damage due to this storm and the "Barometric pressure fell to 966mb at Cape Wrath...new low record for the British Isles in August."
13-14 August 1979	"Southwestern approaches to the British Isles. (The Fastnet race disaster)."	Depression with central pressure 1002mb, filled to 1006mb and deepened to 978mb.	"The biennial Fastnet yacht race saw 303 yachts leaving Cowes, Isle of Wight...On the night of the 13-14th a great storm struck the competitors,...24 yachts were abandoned, 15 of the crew were drowned, and only 85 of the starters were able to finish the race."

tropical summer[7] storm tracks from 1948 to 2002, with focus on climatology, variability and relation to the large-scale flow. The grasping of processes during the summer season may not only provide a better knowledge of the behavior of storm tracks but also give a better understanding of the processes behind summer cyclogenesis. Chang et al. (2002) point out that "...a systematic shift in either their geographical location or the level of storm activity will lead to substantial precipitation anomalies with consequent impacts on regional climates." Thus, a good knowledge of the present summer storm track behavior is relevant for the verification of GCMs[8] and the identification of their future climate projections as well.

In this paper, data from the NCEP/NCAR reanalysis provided by the NOAA-CIRES Climate Diagnostics Center (Kalnay et al. 1996; Kistler et al. 2001) have been used for the Northern Hemisphere (NH) summer (JJA). Results will be shown from the application of statistical tracking techniques to the positive 850-hPa relative vorticity field. The study is based on 54 years NCEP/NCAR reanalysis data from 1948 to 2002. Chapter 2 will analyze the theoretical background, including the definition of baroclinic instability and the dynamics of extra-tropical summer storms, while chapter

---

[7] The period that corresponds to the summer season here comprehends the months June, July and August, and they will be referred as the acronym JJA in the text.

[8] GCM stands for Global Climate Models.

3 will discuss the main findings for the extra-tropical *winter* storm tracks. Chapter 4 will describe the methodology used in this research and the track algorithm idealized by Hodges (Hodges 1994; Hodges 1995; Hodges 1996; Hodges 1999); chapter 5 will present the results: climatology, differences between summer and winter; chapter 6 will focus on the variability and the statistical analysis for the North Atlantic and the Arctic region. Finally, chapter 7 will summarize and discuss the main results.

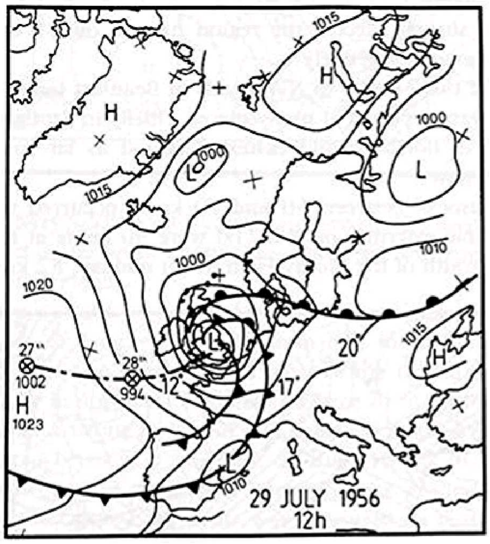

Figure 1.3: The storm of 29 July 1956 caused by a depression which was centered near 47°N 28°W on the 27th and it deepened and curved to the northeast over England on the 29th. This system developed not because of the surface temperatures which ‘were not extreme’, but it drew its energy “in a long stream of direct Arctic air from the northeast Greenland-Spistbergen-Barents Sea...” From Lamb (1991).

Chapter 2

Theory Background

Before we deal with the ensemble of storm tracks, we will discuss the baroclinic instability theory and the role of the ageostrophic wind to the development of individual cyclones. The second part will apply the baroclinic instability to the summer season by discussing the Rayleigh theorem and the role played by the latent heat.

The general *winter* storm track theory will be analyzed in chapter 3. Some concepts such as the definition of storm tracks and the concepts of *baroclinic generation zone* and *downstream development* will be also tackled there. The objective of this chapter is to present the general baroclinic instability theory and to focus on possible explanations for it during the summer season, since there seems to be only a few papers written on this subject.

2.1 Baroclinic Instability

The meridional cross section of longitudinally and time-averaged zonal wind indicates that the maximum zonal wind speed (the mean jetstream axis) is found below the tropopause and it is located at around 30° N in the winter and it moves poleward to $40° - 45°$ N in the summer (Holton 2004). How is this related to baroclinicity? What is baroclinic instability?

Holton (2004) points out that synoptic-scale disturbances develop “preferencially in the regions of maximum time-mean zonal winds associated with the western Pacific and western Atlantic jets and to propagate downstream[1] along storm tracks that approximately follow the jet axes.”

Moreover, the polar frontal zone is the place where the **axis of the jetstream is normally located**. This is the zone which separates the cold from the warm air[2]. Due to the thermal wind balance, an intense jet core is found just above this

---

[1] The downstream development concept will be discussed in the next subsection.

[2] The average temperature gradient between the equator and the pole and the maximum zonal wind speed are larger in the winter season than the summer in the Northern Hemisphere (Holton

zone of large potential temperature gradients. These jets are unstable with respect to small perturbations. When such disturbances are introduced into the jet, they amplify by getting their energy from the jet itself. This instability is called **baroclinic instability**[3] (Holton 2004; Barry and Carleton 2001).

The baroclinic wave development is also dependent on the secondary circulation. Holton (2004) observes that without a secondary divergent circulation, "geostrophic advection tends to destroy the thermal wind balance." It is also through this ageostrophic circulation that cold advection causes the geopotential height to fall, intensifying the horizontal ($N-S$ direction) pressure gradient. Hence, the wind becomes subgeostrophic and is accelerated towards lower pressure, crossing the isobars. This ageostrophic flow is associated with conversion of energy from potential energy to kinetic energy. Thus, the ageostrophic circulation plays an important role in the development of cyclones (Barry and Carleton 2001).

However, for the conversion of APE[4] into kinetic energy to take place, there must be a tilt of the perturbation with height. Holton (2004) considers that:

> ...for quasi-geostrophic perturbations, a westward tilt of the perturbation with height implies both that the horizontal temperature advection will increase the available potential energy of the perturbation and that the vertical circulation will convert perturbation available potential energy to perturbation kinetic energy.

The height of the perturbation tilts when there is a poleward transport of warm air (air rising) and equatorward transport of cold air (air sinking). This process "lowers the center of mass...corresponding to the creation of kinetic energy with time at the expense of a corresponding decrease in potential energy" (Carlson 1991). Thus, the baroclinic instability tends to reduce the pole-to-equator gradient of temperature.

The tilt mechanism is illustrated in figure 2.1, that is, for a perturbation to extract potential energy from the mean flow, the perturbation parcel trajectories must slope less than the slopes of the potential temperature surfaces. Therefore, a temperature gradient is needed to promote baroclinic instability, but is it always like that? What about the summer season when the temperature gradient at the surface is less than the winter one? The next subsection will answer these questions.

2004; Barry and Carleton 2001).

[3] Barry and Carleton (2001) describe that the concept of baroclinic instability was formulated by Charney in 1947, and Eddy in 1949.

[4] The APE (Available Potential Energy) is defined as "the difference between the total potential energy of a closed system and the minimum total potential energy that could result from an adiabatic redistribution of mass" (Holton 2004), or "the difference between existing potential energy and that which would result if the temperature field were adiabatically rearranged to become that of the mean state" (Carlson 1991).

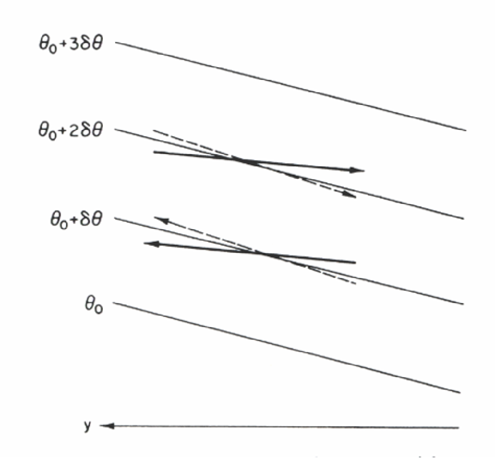

Figure 2.1: *The solid arrows represent the slope that the parcel trajectories have relatively to the potential temperature, for a baroclinically unstable disturbance to occur. The dashed arrows represent a baroclinically stable disturbance. From Holton (2004).*

2.2 On the Baroclinic Instability in the Summer

Due to the fact that the meridional gradient of temperature is not so enhanced during the summer season, which is a condition for baroclinic instability (as seen in the previous subsection), other possible explanations for the summer baroclinicity are presented here. First, the Rayleigh theorem, based on the gradient of potential vorticity and the thermal wind relation, will be used to show that there is a situation in which a temperature gradient at the surface is not needed for baroclinic instability to happen. This could be the case for the summer season, and that is why it is tackled here. Then the role of the latent heat will be pointed out due to the fact that extra insolation in the summer leads to extra evaporation, contributing to the energetics of storm tracks (Barry and Carleton 2001), and the latent heat release during precipitation (Grønås et al. 1994) is an important energy input for baroclinic systems.

2.2.1 The Rayleigh Theorem

The Rayleigh theorem (equation 2.3) discusses conditions for baroclinic instability using the mean meridional gradient of potential vorticity and the thermal wind realation (the variation of **u** in $z*$). The log-pressure coordinate, $z*$, is used instead of z so as to facilitate the derivation of the Rayleigh theorem. This coordinate is defined as

$$z* \equiv -H \ln\left(\frac{p}{p_s}\right) \tag{2.1}$$

where p_s is the standard reference pressure[5] and H is the scale height, given by[6]:

$$H \equiv \frac{RT_s}{g} \tag{2.2}$$

In an isothermal atmosphere, z* is equal to the geometric height. This theorem assumes a continuously stratified atmosphere on the midlatitude β plane and it also applies necessary boundary conditions at lower and upper boundary pressure surfaces. One obtains the Rayleigh theorem by considering a linear boundary value problem, using the quasi-geostrophic equation, applying the perturbation method and boundary conditions in the basic flow. After that, normal mode solutions are obtained and energy considerations are made. Thus, applying these assumptions and simplifying the equations, the final form of the Rayleigh theorem (Holton 2004) is given by:

$$C_i \left[\int_{-L}^{+L} \int_{0}^{\infty} \frac{\partial \overline{q}}{\partial y} \frac{\rho_0 |\Psi|^2}{|u - c|^2} dy dz^* - \int_{-L}^{+L} \varepsilon \frac{\partial \overline{u}}{\partial z^*} \frac{\rho_0 |\Psi|^2}{|\overline{u} - c|^2} |_{z^*=0} dy \right] = 0 \tag{2.3}$$

where C_i represents the growth rate of the amplitude, and $|\Psi|^2 = \Psi_r^2 + \Psi_i^2$ is the disturbance amplitude squared, $\frac{\partial \overline{q}}{\partial y}$ is the potential vorticity (the gradient towards north), $\frac{\partial \overline{u}}{\partial z*}$ is the vertical shear of the wind (in log-pressure coordinates). Finally, $\varepsilon \equiv \frac{f_0^2}{N^2}$, which is the ratio between *f*, the planetary vorticity and N, the buoyancy frequency[7].

For the baroclinic instability to happen, C_i, that is, the growth rate, must be different than zero. In other to achieve that, the values inside the square brackets [ ] must be equal to zero so as to satisfy the equation. Since the two main elements inside the square brackets for the discussion of baroclinic instability are: $\frac{\partial \overline{q}}{\partial y}$ and $\frac{\partial \overline{u}}{\partial z^*}$, there are three cases in which their summation could be zero, according to Holton (2004):

(i) If there is no meridional temperature gradient at the surface, then $\frac{\partial \overline{u}}{\partial z^*}$ at $z^* = 0$ would be equal to zero. Then the Rayleigh necessary condition says that $\frac{\partial \overline{q}}{\partial y}$ must be zero somewhere, since there is a shift of the PV gradient at the surface (towards the South) to a PV gradient towards North at higher levels;

(ii) If $\frac{\partial \overline{u}}{\partial z^*} \geq 0$ everywhere, $\frac{\partial \overline{q}}{\partial y}$ must be > 0 somewhere at the lower boundary for $C_i > 0$;

(iii) If $\frac{\partial \overline{q}}{\partial y} > 0$ everywhere at $z^* = 0$, then $\frac{\partial \overline{u}}{\partial z^*} < 0$ somewhere.

Case **ii** is the one which happens more often. But which one could be better related to the summer season? Since the temperature gradient during summer is not

---

[5] Normally taken at 1000 hPa.

[6] T_s is the global average temperature and R is the gas constant for dry air.

[7] Normally referred to as the $Brunt - V\ddot{a}is\ddot{a}l\ddot{a}$ frequency.

so enhanced, case **i** could be an explanation for the summer baroclinic instability in the NH. That means: it is not necessary to have a temperature gradient at lower levels for the baroclinic instability to happen. But, are there other driving forces in the summer baroclinic instability storm tracks? And, what about case **iii**? The influence of the latent heat may be also related to case **iii** and to the baroclinic instability in the summer.

2.2.2 Some Energy Considerations

Many driving forces may be accounted for the baroclinic instability in the summer, such as strong surface heating, convective instability, reduced static stability, increased moisture availability and the latent heat. Here, only the contributions of the latent heat are presented: first, because it is one of the most powerful driving forces in the summer due to the enhanced evaporation; second, because it is a powerful element for the development of frontogenesis as well.

During the summer season, the maximum solar energy received in the N.H. summer is not all available for kinetic energy transformation. Therefore, the N.H. winter is the season in which there is a maximum kinetic energy (Hartmann 1994; Chang et al. 2002). So, if the kinetic energy during the summer is not at its maximum and if the gradient of temperature during the NH Summer is not high, what does drive the baroclinic instability during the NH summer season?

The **latent heat** may be another answer for the baroclinic instability in summer since it is one of the most powerful driving forces during this season. Serreze et al. (1990) pointed out that "surface heat fluxes associated with areas of more open ice cover - forced in part by the cyclone activity - may provide a feedback to help maintain the cyclone." Besides that, the latent heat released during the rising air over the warm sector of cyclones acts as an additional energy source to the eddies within the storm tracks, whereas the surface sensible heat fluxes, mainly over the oceans, act as an energy sink: they reduce temperature perturbations close to the surface (Branscome et al. 1989).

Several case studies have shown that latent heat plays a major role in summer cyclogenesis (Kristjansson 1990; Uccellini 1990; Grønås et al. 1994). By using a case study of a summer storm which hit Germany in August, 1989, Grønås et al. (1994) showed that the latent heat release was responsible for strengthening a dying out storm. The authors proved that during the latent heat release, on the occlusion side of that storm, a positive anomaly of potential vorticity formed under the LH release zone and a negative anomaly above it. This PV anomaly strengthened the existing PV anomaly. This case is different from what normally happens, that is, the PV distribution "...will typically deform along the fronts and might be advected away from its source...this way the effect of the heat release will be spread around the cyclone..."

In summary, there is a void in literature with respect to the dynamics of storm tracks during the summer season. Most of the theory found in literature is about the general theory and most of the examples are related to winter. Therefore, in order to build a basis to which we could work on this thesis, theoretical assumptions were taken so as to guide us during the research process. These approaches form the pilars of this thesis and are summarized here:

(i) Baroclinic instability is also possible without a temperature gradient at the surface, following the Rayleigh theorem (Holton 2004);

(ii) Latent heat plays an important role for summer storms, especially because it strengthens weak storms by 'creating' a positive PV anomaly at the surface (Grønås et al. 1994; Kristjansson 1990; Uccellini 1990);

(iii) Summer storms may be related to the large-scale flow, which could contribute for their growth and development;

(iv) Convection and diabatic heating, due to open sea-ice areas and warm western bounday currents (Hoskins and Valdes 1990) could promote extra energy to summer storms.

These four pilars serve only as a theoretical guidance through the thesis. However, our intention with this research is to 'map' the climatology of summer storms and investigate their variability and relation to the large-scale flow. So far, a discussion of the baroclinic instability and the application of the theory to the summer season were presented. The next chapter discusses the *winter* storm track theory and findings.

Chapter 3

Extra-Tropical Winter Storm Tracks

3.1 References

Many papers have been written with respect to the winter season, thus, in this chapter, a brief description of the main findings in the vast literature related to winter storm tracks is presented. It will also discuss some important concepts related to the general storm track theory: the definition of storm tracks, methods used for tracking storms, the preferred geographical distribution of the tracks and considerations on their dynamical features.

Some aspects such as the method and level dependence that have been used for winter studies will be also discussed. This will be done in order to clarify the selection made under this research. The relation to the large-scale flow will be mentioned, emphasizing the importance of the NAO to winter storms, this will provide an insight into the findings related to summer tracks in chapter 6.

This chapter will not provide an extensive description of all aspects related to the general theory of storm tracks during wintertime, but it will focus on their main characteristics so as to serve as a guide to the comparison between the summer and the winter storm tracks in later chapters.

3.2 Methods

There are a number of methods and meteorological parameters that have been used for analyzing the storm tracks. Here, a description of the most used ones are mentioned. Sorteberg et al. (2004), in a paper about winter storm tracks, emphasize that quantitative comparisons with other papers are difficult to be made, and this is due to the fact that there are many different ways of tracking storms.

Hoskins and Hodges (2002), in their study about the Northern Hemisphere winter storm tracks from 1979 to 1994, point out that the selection of the method for analyzing storm tracks is important, as well as the choice of meteorological parameter. They mention that there have been two main approaches for tracking storms: one which considers the weather systems, tracks their positions with time and produces statistics for their distributions (Murray and Simmonds 1991; Jones and Simmonds 1993; Serreze et al. 1993; Sinclair 1994; Anderson et al. 2003); the second which determines simple statistics at a set of grid points, for example, the variance in a frequency band associated with the synoptic time-scales (Cai and van der Dool 1991; Chang and Fu 2002; Hoskins and Hodges 2002). These authors argue that this class of method does not tell everything one wants to know about the types of systems: several storm attributes can only be *speculated* from such statistics.

Therefore, Hoskins and Hodges (2002) emphasize the importance of the use of automated methods which allow for the exploration of storm track activity. They fill in the gap the other methods could not accomplish. These objective methods make use of the nearest neighbor approach[1] with simple grid box statistics; or the more sophisticated approaches of tracking and statistical estimation.

In relation to the meteorological parameter, Hoskins and Hodges (2002) also discuss the different fields that have been used and tested for tracking storms, such as: the MSLP, geopotential at 500hPa, the lower tropospheric vorticity and others. They point out that there are drawbacks in the use of some of these fields, for example, the MSLP is an extrapolated field and may be sensitive to: how the extrapolation is performed; and the representation of the orography in the model. It is also influenced by large spatial scales, for example, by the Icelandic low and strong background flows. The unfiltered MSLP tends to be dominated by large-scale features and biased towards the slower moving systems[2].

The 500hPa geopotential height presents similar problems, since it is also dominated by large spatial scales. However, vorticity has been found to be a better field for identifying synoptic systems and it is less influenced by the background flow. Hoskins and Hodges (2002) also removed the background field as an approach to identify mid-latitude synoptic features in order to look for extrema in the field. Even though these assumptions were made in relation to the winter season, they will also be applied in this thesis, that is, the field chosen to be analyzed is the positive vorticity at 850hPa, which was also used by Byrkjedal (2002) and Sorteberg et al. (2004), for example.

---

[1] See section 4.2 for more information on the nearest neighbor approach.

[2] Gulev et al. (2001) use an alternative approach. They do not use the band-passed statistics to identify storm tracks, but they track storms using sub-daily SLP analysis. It is based on the computer animation of SLP fields and it combines numerical and manual approaches.

3.2.1 The Definition of Storm Tracks

This subsection and the next present the definition and the dynamics of storm tracks. It also considers the relation between **the baroclinic generation source** and **the wave packets**: two important concepts for understanding the transient eddies in mid-latitude.

The weather in mid-latitudes is affected considerably by synoptic-scale low pressure systems. These systems are organized geographically, they have relative frequency of occurrence and they also have 'preferred' paths in which they travel, called 'storm tracks'.

Wallace and Blackmon (1983) analyzed the northern hemisphere daily 500 mb height data for winters 1962 to 1979-80 to study their spatiotemporal characteristics. They were able to isolate "three time scales" (Barry and Carleton 2001) for the general circulation in the Northern Hemisphere based on filtered data[3]. These time scales are named after the type of filter used, they are described below and represented in figure 3.1:

(i) *A Band-pass filter* - it distinguishes baroclinic waves and "it depicts a zone resembling that of storm tracks over the oceans" (Barry 2001);

(ii) *A low-pass filter* - it emphasizes fluctuations longer than ten days;

(iii) *A thirty-day average* - both numbers (ii) and (iii) describe high variance (from the original unfiltered data) in regions of the North Atlantic, North Pacific, and Siberian Artic that have been identified as centers of blocking activity.

Since item (i) resembles the storm tracks, it is therefore used for their identification and conceptualization. Barry and Carleton (2001) considered that "the geographical pattern of variance of (ii) and (iii) is reasonably constant at time scales beyond 10 days" and that the baroclinic waves **do not contribute** as much to the total variance as the low-frequency components (item ii) do. Based on that, Chang et al. (2002) define storm tracks on the **bandpass** transient variances. The variance amplitudes (of the variance of the different atmospheric fields such as the geopotential height, the poleward fluxes of heat, momentum, etc.) extend approximately from the western North Pacific, across North America and the North Atlantic, into northern Europe.

In summary, the band-pass variance delimits regions of high cyclone frequency and it "is oriented along the paths of phase and group propagation of synoptic transients." Hoskins and Hodges (2002) also argued that "...the filtered variance should really be considered as a baroclinic wave-guide since the temporal filtering tended to turn weather systems that on a mean sea-level pressure (MSLP) map moved eastwards and either polewards (cyclones) or equatorwards (anticyclones) into alternating

---

[3] The filtering process was done in order to isolate and distinguish the three different time scales.

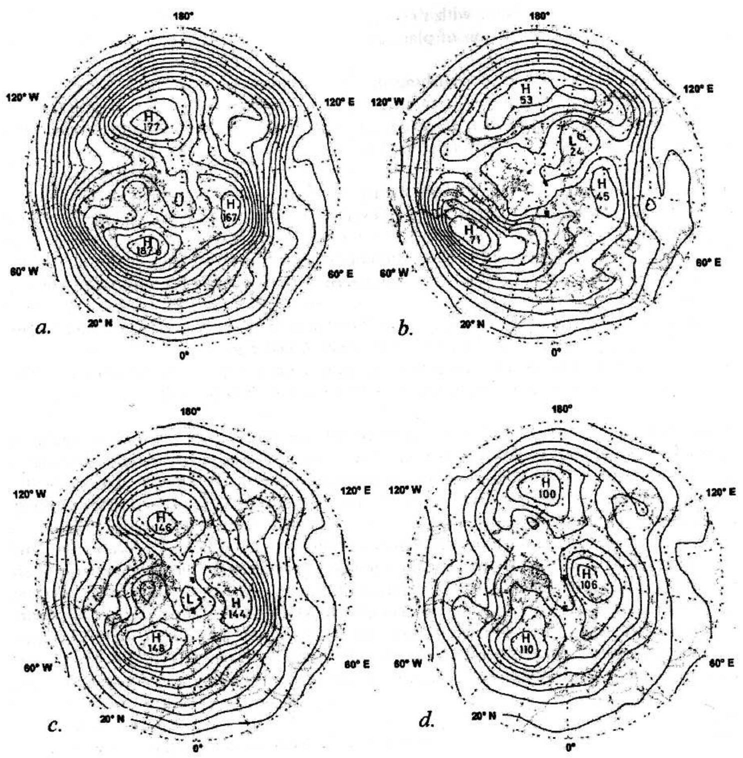

Figure 3.1: Variance of 500 mb height for winters 1962/63-1979/80 (10m contour intervals). (a) Unfiltered twice daily data; (b) Band-pass filtered to show two and a half to six-day baroclinic waves; (c) Low-pass filtered for periods over ten days; (d) Thirty-day mean value. The contribution of the mean annual cycle to the December-February values has been removed. From Wallace and Blackmon (1983).

features moving eastwards along the waveguide." Hence, the band-pass variance (i) characterizes the term "storm tracks."

3.2.2 The Dynamics of Storm Tracks

Storm tracks are associated with baroclinic generation[4], that is, the conversion of APE (Available Potential Energy) related to poleward and upward motion of warm air and the equatorward and downward motion of cold air within the baroclinic waves and frontal cyclones. Thus, baroclinic instability is responsible for the observed mid-latitude cyclogenesis.

Hoskins and Valdes (1990) proposed a threefold process which allows for the enhanced baroclinicity over the storm track entrance regions in the Northern Hemisphere:

(i) Storm track eddies in general are vigorous downstream of the regions of maximum baroclinicity, and the mixing of temperature by eddies is better where the baroclinicity is largest;

(ii) Storm tracks are self-maintained due to the fact that diabatic heating maxima are caused by the eddies themselves. The enhanced baroclinicity itself is actively maintained by condensational heating over the storm track entrance region;

(iii) The warm western boundary currents in the ocean are driven by the wind stress of the low-level flow induced by the eddies, which in turn, establishes zones of high baroclinicity due to land-sea temperature contrasts.

The second idea behind the threefold process is though questioned by Lee and Mak (1996). In their view, storm tracks are not completely self-maintained. They showed that enhanced baroclinicity over the storm track entrance region could also be maintained by stationary waves induced by mountains alone, without the need for diabatic heat sources near the storm track entrance regions.

There are also some important concepts related to the definition of storm tracks and the use of the band-pass variance (Chang and Orlanski 1992):

(i) The storm tracks start in a region called *baroclinic generation zone*;

---

[4] The Eady growth rate is a means to achieve a better understanding of the process of baroclinicity. It can be used to localize baroclinic zones: this is important since “regions of high baroclinicity over the mean Northern Hemisphere winter conditions correlate well with regions of high eddy activity” (Chang and Orlanski 1992). It is defined as (Chang and Orlanski 1992): $\sigma_{BI} = 0.31\frac{f}{N}|\frac{\partial \mathbf{v}}{\partial z}|$, where f is the Coriolis parameter, N is the Brunt-Väisällä frequency, z is the vertical distance and $\mathbf{v}$ is the wind vector. However, Chang and Orlanski (1992) argue that in spite of the fact the Eady growth rate can localize baroclinic zones, it does not relate to the location of the eddies. These eddies or baroclinic waves are found downstream of the source baroclinic region and they develop in groups (the groups are called wave packets and the process is called “downstream development of baroclinic waves”), through radiation of energy. Chang and Orlanski (1992) have also shown that the ageostrophic geopotential fluxes by an upstream eddy acts as a trigger for the development of downstream cyclones. Thus, the ageostrophic fluxes contribute to the growth and decay rates in the nonlinear life cycles of individual cyclones, since they act as a source of energy for the growth of the next downstream wave (Orlanski and Katzfey 1991).

(ii) The tracks develop eastwards from the baroclinic generation area in a process called *downstream development*;

(iii) Storm tracks may be considered an ensemble of wave packets.

The last item in the list above is an important concept reported by Chang et al. (2002): storm tracks transients may be considered "an ensemble of wave packets with wave growth and decay occurring over all portions of the storm track," and these waves propagate eastwards. These wave packets[5] are also characterized by a developed group velocity which "coincides with the general direction of the storm track axes, while the group speed is on the order of the speed of the jet itself."

The storm track development may also be illustrated from an energetic point-of-view (Orlanski and Katzfey 1991; Chang and Orlanski 1992; Chang et al. 2002). First, there is baroclinic generation of energy over the storm track entrance regions (*baroclinic generation zone*). Then eddy energy is dissipated over the downstream area (*downstream development*) by barotropic conversion (which may serve as a fuel to the neighbouring eddies), and surface friction over the continents (*dissipation*). The concepts of *baroclinic generation zone*, *downstream development* and *dissipation* are illustrated by figure 3.2, which shows a numerical model of the eddy kinetic energy along a channel (Chang and Orlanski 1992). First, waves develop via baroclinic conversion on the left side of the channel. Then, the waves develop downstream via ageostrophic geopotential fluxes which provide energy for the next downstream wave to grow.

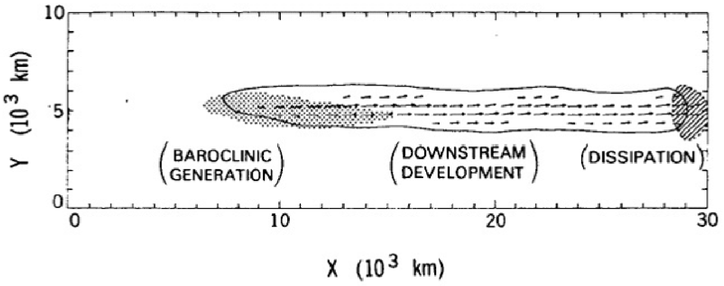

Figure 3.2: A numerical model of the eddy kinetic energy (solid contour) along a channel. The dotted region is the baroclinic generation region and the hatched region is the dissipation. The arrows represent the ageostrophic geopotential flux vectors. From Chang and Orlanski (1993).

3.2.3 Tracking the Storms

The approaches for tracking storms may be divided into two kinds: manual techniques and automated detection. Early manual attempts were done by Streten and Troup

---

[5] The individual synoptic eddies, within the nonlinear wave packets, decay by transferring their energy to their neighbor eddies downstream, a process called *downstream development*.

(1973), Akyildiz (1984) who used data for the North Atlantic and constructed appropriate statistics, Reed et al. (1986), and others. These attempts were important, but limited, both in space and time. With the development of high speed computers and satellite technology many researchers started using satellite images (pattern recognition, cross-correlation techniques) for tracking storms: Endlich et al. (1971), Leese and Novak (1971). Automated detection started with Williamson (1981), who identified anomalies in the 500-mb geopotential height. Later, Le Treut and Kalany (1990) and Murray and Simmonds (1991) used pressure data to track storms.

Hodges (1994, 1995, 1996, 1999) developed a synoptic objective analysis method, which is an automatic approach based on ensemble statistics and the use of a cost function that tracks storms with greater confidence. This technique "...enables synoptic climatologies to be constructed and compared efficiently for different models and satellite data" (Hodges 1999). Subsection 4.2 will describe the method used by Hodges as well as the cost function needed to track the storms within the different frames and subsection 4.2.1 will explain in more details how the algorithm is applied to the dataset.

3.3 Mean Structural and Temporal Characteristics

Numerous studies use different altitude levels for studying the winter storm tracks. For example, Hoskins and Hodges (2002), when referring to upper pressure levels, mention that the standard tropospheric variance diagnostic is most applied for the 250hPa height. They point out that the 250hPa vorticity (ξ_{250}) and 330K potential vorticity (PV_{330}) fields yield very similar results.

However, they describe an advantage of working with the 850hPa level, which is the fact that the positive meridional wind can be associated with the warm sectors of storms and negative meridional wind with the cold air behind the systems, at this level. They also examined that the "most surprising aspect of the T_{850} diagnostics is the contrasting picture it paints of the two major storm tracks," that is the Pacific one seems to have small amplitude meridional displacements of the oceanic baroclinic region. Besides that, the Atlantic track has cold air systems over North America which decay on the coast or as they flow over the warm waters interacting with the warm anomalies in air from the Sargasso Sea region.

Key and Chan (1999) used the NCEP reanalysis data from 1958-97 in the northern hemisphere and found out, for $60° - 90°N$, that closed lows increased in frequency at 1000 mb in all seasons and decreased at 500 mb, except in winter. However, in mid-latitudes (between 30° and 60°), the frequency of lows decreased at 1000 mb and increased at 500 mb, except in winter.

Figure 3.3 shows sections of the seasonal variations of the baroclinic wave amplitude in 300-hPa for different longitude bands and the vertical shear of the zonal wind between

500-and 925-hPa. It is observed that the maximum values are not in the summer season, but concentrated between November and April. Chang et al. (2002) show that "the association of storm tracks with mid-latitude baroclinic zones suggests that storm tracks, like the zonal mean pole-to-equator temperature gradient, will experience a pronounced annual cycle." Figure 3.3 a,b shows that the Atlantic and Pacific storm tracks shift equatorward in step with the jet stream from fall to midwinter, and then migrate poleward after January. The Pacific storm is strongest during fall and spring with a minimum in eddy amplitude during midwinter. However, the Atlantic storm tracks have their maximum amplitude around midwinter. Figure 3.3 c shows that there is a greater zonal wind shear over the Pacific during midwinter than in fall or spring.

Hoskins and Hodges (2002) summarize that many "interesting speculations can be made by focussing on the track of cyclonic features as given by negative θ_{PV2} and positive ξ_{850}," for example, the band starting in the sub-tropical eastern North Atlantic and spiralling around the hemisphere in the upper troposphere could provide a source of perturbations that amplify through the depth when the *lower tropospheric* conditions are favorable. Many other researchers have used the positive 850hPa vorticity ξ_{850} for analyzing the winter storm tracks (Hoskins and Hodges 2002; Sorteberg et al. 2004; Byrkjedal 2002), and it was thus selected as the level to be studied in this thesis as well.

3.4 Geographical Distribution of the Tracks

Most tracks extend their location from the east coast of the Northern Hemisphere continents to north-eastward across the oceans. For instance, in the North Atlantic, systems either turn northward into Baffin Bay or more frequently, continue northeastward to Iceland and the Norwegian-Barents Sea. Many of the winter tracks are found "between Greenland and Iceland...area identified as a region of orographic cyclogenesis, associated with the lee of southern Greenland" (Serreze 1995). In the North Pacific, systems move from eastern Asia towards the Gulf of Alaska[6]. They form or redevelop east of the Rocky Mountains in Alberta and Colorado and move eastward towards the Great Lakes and Newfoundland before turning northward towards Greenland and Iceland (Murray and Simmonds 1991; Jones and Simmonds 1993; Serreze et al. 1993; Barry and Carleton 2001).

Bluestein (1993) mentions three regions of relatively frequent cyclogenesis in the United States:

(i) The lee of the Rocky Mountains from Alberta through Montana;

(ii) The lee of the southern Rocky Mountains, including southeastern Colorado, west-

---

[6] See figure 3.4 which shows physical maps of North America and Europe, respectively.

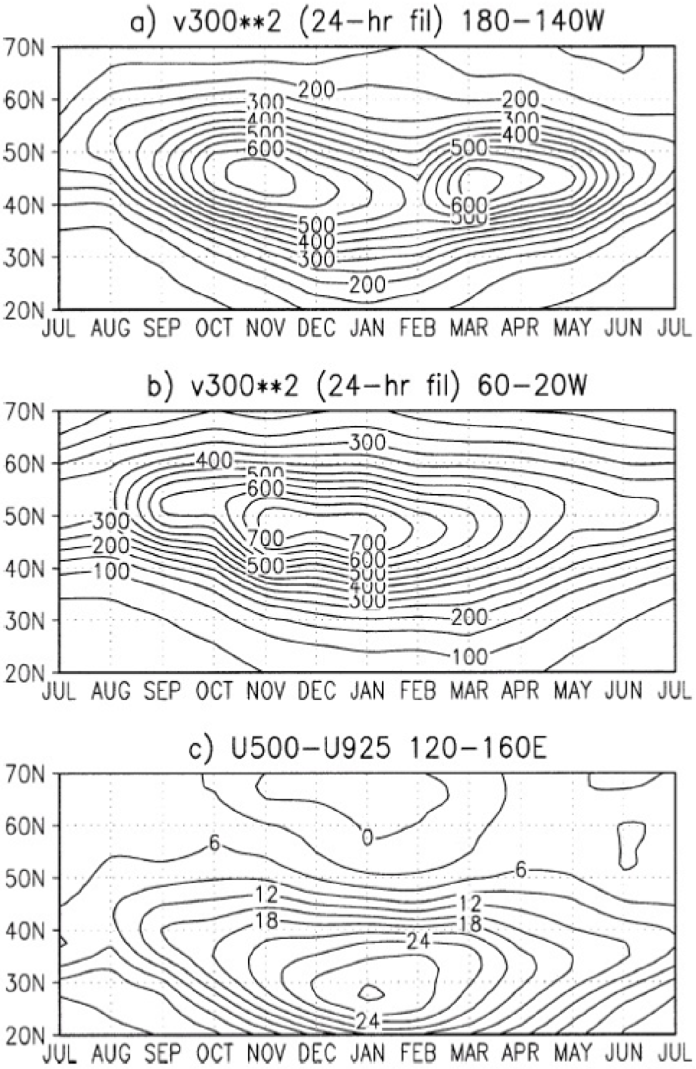

Figure 3.3: *(a)The Latitude versus time sections of the seasonal variations of the baroclinic wave amplitude in 300-hPa* v^2*, averaged over the longitude band* $180° - 140°W$*; (b) The same as in (a) but for the longitude band* $60° - 20°W$*; (c) The vertical shear of the zonal wind between 500-and 925-hPa levels over the longitude band* $120° - 160°E$*. From Chang et al. (2002)*

ern Kansas, northeastern New Mexico, the Oklahoma Panhandle, and the northern Texas Panhandle;

(iii) Offshore from the Mid-Atlantic states and southern New England.

The mean climatological number of cyclones over the Northern Hemisphere is 234 per winter. On average, 99 of them were generated and propagated over the Pacific sector, and about 130 over the Atlantic sector including the Arctic (50 cyclones).

The modal hemispheric life time is 2-3 days and 50% of all cyclones exist from one to

Figure 3.4: *The physical North America and Europe maps, respectively, for location of some of the descriptions used in this research. Source: http : //worldatlas.com*

four days (Gulev et al. 2001). However 17% of cyclones are long-living, with lifetimes longer than seven days. More than 60% of cyclones in the Atlantic exist from 2 to 6 days with the mean lifetime of about four days. The Arctic region is characterized by the shortest cyclone lifetimes with a mean of less than three days. For the Northern Hemisphere the total number of cyclones has a downward tendency of 12 cyclones per decade. However, Hoskins and Hodges (2002) found that the mean lifetimes of features, in the Atlantic, are between 4 to 5 days, which is quite different from what was found by Gulev et al. (2001), mentioned before.

Hoskins and Hodges (2002) analyzed the Northern Hemisphere winter storm tracks in a period which goes from 1979 to 1994 with respect to different synoptic fields. Besides the similar places mentioned before, they also suggest the existence of a third one: Siberian storm track near $60^\circ N, 60^\circ - 90^\circ E$. They also identify some synoptic activity in the Mediterranean area. They point out the identification of the track density maxima across the Pacific and from east of the Rockies to Iceland, and a third weather maximum east of the Urals. Another region of maximum is found east of Japan and in the central Pacific. They mention some genesis[7] activity north-east of Cape Hatteres, in the Iceland and Norwegian Sea regions, western Mediterranean, the Caspian Sea and north of Greenland, which they report as being possibly associated with katabatic winds[8] which are known to be associated with the generation of vorticity and meso-cyclones on the slopes of high orography in polar regions.

---

[7] See subsection 4.2.2 for the definition of *genesis* density.

[8] Katabatic winds refer to winds which flow down a topographic incline (e.g.: moutains) and are cooler than their surroundings.

The main cyclolysis[9] areas are on the northern side of the Pacific storm track and a strong double maximum on the west coast of North America, near Vancouver Island and the Gulf of Alaska. Hoskins and Hodges (2002) say that there is a maximum in the Gulf of California as well, and it is associated with cut-off lows. Another cyclolysis region is from the eastern Great Lakes to the Hudson Bay and extending to Iceland, the north-east coast of Canada, on the southern tip of Greenland and south of Iceland, in the Norwegian Sea and in Siberia.

Sorteberg et al. (2004) investigated the winter storm tracks and they assessed their importance for the upper ocean circulation in the Nordic Seas. Among the same regions mentioned before, they also identify the band density which goes from Newfoundland across the North Atlantic into northern Europe as the most pronounced features. Serreze (1995) showed that local peaks in the cyclone frequency and pronounced deepening rates[10] are found between Greenland and Iceland (the Icelandic Low). Other common areas are over Baffin Bay / Davis Strait, south of Baffin Island and in the Norwegian and Kara Seas.

Hoskins and Valdes (1990) used the wintertime dataset (DJF) from a 6-year climatology of ECMWF and found out that "...the crucial ingredient in the existence of mean conditions suitable for the existence of the two Northern storm-tracks is the mean diabatic heating in the region of the storm-tracks, off the east coast of the continents." They also argue that the North Atlantic and Pacific storm tracks are self-maintaining, due to the fact that the diabatic heating maxima in the storm-track regions are caused by horizontal displacements of individual storms. They consider that the warm oceans off the east coasts of the cold North American and Asian continents provide the conditions in which storm tracks are inevitable, which can also contribute to the self-maintenance of the storm tracks and for driving ocean currents (Hoskins and Valdes 1990):

> The low-level mean flows induced by all the eddy effects... have wind-stress curls that are in the sense of driving the warm Gulf Stream and Kuroshio. Thus, the storm-tracks act to drive the warm western boundary currents, which in turn are crucial to the existence of the storm-tracks.

Serreze et al. (1993) and Serreze (1995) examined the cyclone maximum of the winter months from 1973 to 1992 and found out that the cyclone maximum near Iceland moves northeastward into the Norwegian-Barents Sea. In the summer half-year[11] this tendency is almost absent. Besides that, Hoskins and Valdes (1990) used the Eliassen-Palm flux to explain the SW-NE tilt of storm tracks.

---

[9] See subsection 4.2.2.

[10] Serreze (1995) explains that for the Arctic Ocean and land regions, the mean maximum deepening rates are greater in summer than winter, but with smaller standard deviations.

[11] From April to September.

Figure 3.5 shows the cyclone frequency in the Northern Hemisphere from 1958 to 1977 by Whittaker and Horn (1984). In the wintertime (January), the highest values are mainly found over the Hudson Bay, over most of the North Atlantic and the North Pacific as well. During the summer season (July), similar features are observed, such as high frequency over the Hudson Bay and through parts of Canada, and over the North Pacific. However, the maximum over the North Atlantic in the wintertime is not so intense during the summer season.

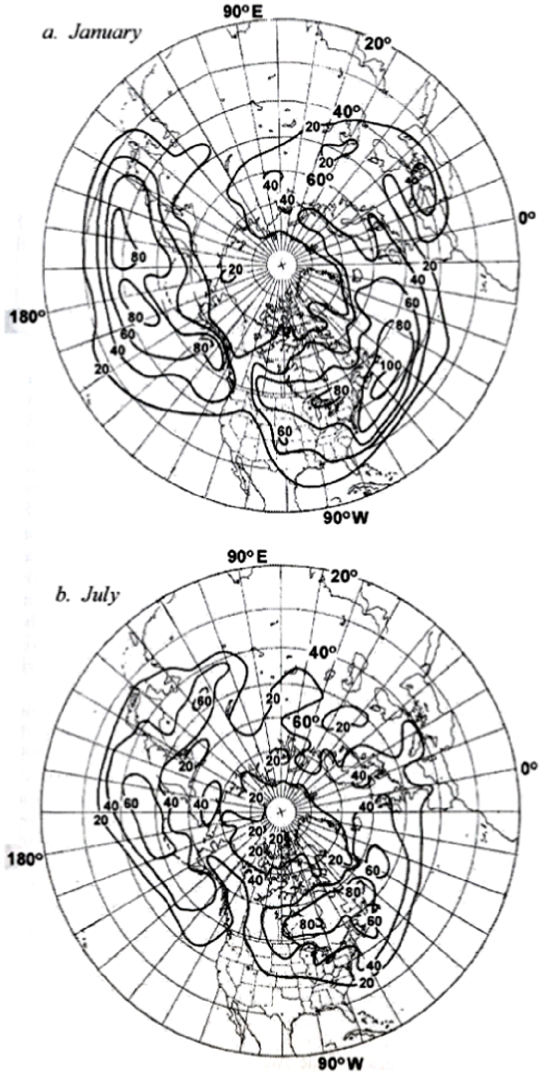

Figure 3.5: *Mean frequency of cyclogenesis in the Northern Hemisphere from 1958 to 1977 for (a) January; and (b) July. From Whitaker and Horn 1984.*

3.5 Relation to the Large-Scale Flow

Extra-tropical synoptic-scale motions may be characterized by the so-called quasi-geostrophic theory, since the velocity of these motions is nearly geostrophic. Due to the different land-ocean distribution and orography, the mean horizontal atmospheric circulation do not appear perfectly zonally symmetric, but instead, an asymmetry in the flow is observed when looked at weather maps[12].

Gulev et al. (2001) and Hoskins and Hodges (2002) considered that the storm track activity over the Northern Hemisphere is connected to the dominant patterns of atmospheric variability, such as the NAO and the North Pacific Oscillation (PNA). Positive anomalies of the NAO index are associated with the strengthening of the mid-latitudinal westerly flow over the North Atlantic, and should lead to the intensification and poleward deflection of the North Atlantic mid-latitudinal storm track. The Atlantic cyclone frequency demonstrates a high correlation with NAO and reflects the NAO shift in the mid 1970s, associated with considerable changes in European storm tracks.

Sorteberg et al. (2004) confirmed that the storm track activity in the Northern Hemisphere is closely connected to the NAO index and the PNA (the North Pacific Oscillation) as well. They also stated that:

> Positive anomalies of the NAO index... are associated with a strengthening of the mid-latitude westerly flow over the North Atlantic. This strengthening manifests itself as an intensification and poleward deflection of the North Atlantic mid-latitudinal storm track. It has been found... that the increase in number of positive NAO winters/years has led to a two-fold increase in the occurrence of cyclones during the period 1964-1993 in the Icelandic Low region.

They also show strong interannual (2.5-year) and decadal (7-12-year) fluctuations in the number and intensity of the mean Nordic Sea cyclones with peaks in the early 1970s, 80s and 90s. They finally point out that "...the number and intensity of the Nordic Seas cyclone variability are linked to the NAO and AO with a slightly stronger correlation with the AO due to the reduced NAO correlation in the 1960s."

This chapter has focused on the main aspects of the winter storm track theory related to recent findings. It discussed the methods that have been used, for example, the application of the positive relative vorticity instead of the MSLP (Hoskins and Hodges 2002); it also emphasized the definition of storm tracks based on the band-pass filter (Wallace and Blackmon 1983), and talked about their dynamics under a different

---

[12] In synoptic systems, the horizontal scale is of about 1000-2000 km and the lifetime is of five to seven days. In mid-latitudes, a weak low pressure system has a central MSL pressure of less than about 1008 mb and a high pressure system, a central MSL pressure, of greater than 1016 mb (Barry and Carleton 2001).

perspective (Chang and Orlanski 1992); it discussed the mean structural and temporal characteristics of the tracks; it showed their main geographical distribution; and finally, it presented their relation to the large-scale flow (Sorteberg et al. 2004; Hoskins and Hodges 2002; Gulev et al. 2001). The next chapter will discuss the methodology used in this thesis under the light of the previous discussions.

Chapter 4

Methodology

This chapter will describe the dataset and the period selected to study the summer storm tracks. Later, the tracking algorithm will be explained on how it is applied for producing the different climatological variables using the relative vorticity field. Finally, links between the storm track diagnostics (in selected regions) and the large-scale flow will be further investigated.

4.1 The Dataset

In this thesis we use data from the NCEP/NCAR reanalysis provided by the NOAA-CIRES Climate Diagnostics Center (Kalnay et al. 1996; Kistler et al. 2001) for the Northern Hemisphere (NH) summer (June to August). The dataset chosen comprises a period of 54 years, from 1948 to 2002. In order to compare the winter and summer seasons, a winter (December to February) dataset from the NCEP/NCAR reanalysis was also used.

The 850-hPa vorticity field will be applied to the tracking algorithm instead of the mostly used MSLP. The vorticity is here used due to the fact that the MSLP is influenced by large spatial scales (e.g.: the Icelandic Low) and by strong background flows (e.g.: fast moving synoptic scales can be masked by this flow until significant development has occurred) (Barry and Carleton 2001; Hoskins and Hodges 2002). Besides that, the unfiltered MSLP tends to be dominated by large-scale flow and biased towards the slower moving systems. Thus, the vorticity "has been found to be a better field for identifying synoptic systems..." (Hoskins and Hodges 2002) and it is not so influenced by background flow, because it focus on smaller spatial scales.

A climatological study of the summer extra-tropical storm tracks is presented here in order to get a clearer picture of how the summer storm system behaves and to find out new features that can lead to more accurate information which can be used by the GCMs.

4.2 The Tracking Algorithm

During the tracking process, two major techniques are used: the nearest neighbour approach and the optimization of a cost function (Hodges 1999). A drawback of the first technique is that it can be dependent on the data ordering at a certain time step. This approach consists of linking one point of the storm track to the nearest grid point (neighbor). However, this process may be biased since the nearest point could be related to another storm (Figure 4.1). In order to avoid that, the cost function approach is applied and it tries to locate and link the object points more precisely.

Figure 4.1 shows that by using the nearest neighbor technique, during the search for the next neighbour point, a swap between the indexes may occur and this would lead to an error in the tracking approach. However, by employing a cost function optimalization algorithm, no matter which initialization is used, it will track the storms more accurately. The tracking algorithm used by Hodges (1994, 1995, 1996, 1999) makes use of ensemble statistics in order to find the feature points of the storms and to estimate the main variables. This process uses different constraints so as to guarantee trustworthy tracking. One of such constraints is the threshold chosen to remove tracks that last less than 2 days or which travel less than 5° (about 500 km) (Hodges 1999).

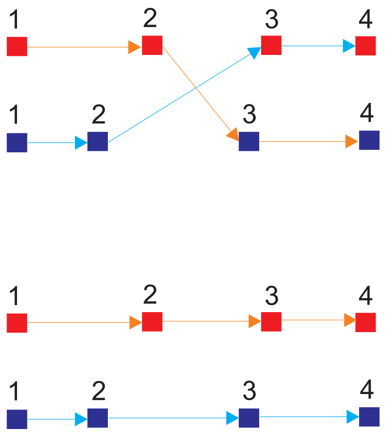

Figure 4.1: *An illustration of the tracking technique by (a) the application of the nearest neighbor approach where point 2 tracked the wrong point 3 and (b) the use of a cost function, where the tracking technique is more accurate.*

The cost function[1] is "...constructed from local track smoothness measures, with the smoothness being measured in terms of changes in direction and speed." Therefore, a number of 3 consecutive frames are required for the ensemble statistics. First, it uses the different frames to locate and index each storm center found. After that, if incomplete tracks are found, they are padded out with "phantom" feature points, so

---

[1] See appendix A for more details on this function.

that "...all tracks have the same number of points and span the length of the time series." Then the "...optimization swaps points on the tracks to give the greatest gain in smoothness" and it goes on both forward and backward in time to guarantee that there is no point ordering dependence in the final result (Hodges 1999).

4.2.1 Using the Dataset to Track Storms

In order to apply the tracking process and the cost function, the dataset needs to undergo a series of identification processes:

(i) **Selection** - The start point is the user's selection of a region of interest and a threshold value;

(ii) **Segmentation** - This process divides the selected region into distinct areas and it gives all points (or pixels) a unique label;

(iii) **Identification** - Points which have intensities larger than the user defined threshold value are characterized as 'object points'. These objects can be the extrema in the vorticity or pressure fields, clouds in a satellite image and so on. The points which have a value that is less than the specified threshold are classified as 'background' points. The next formula shows that 'object points' are identified as number 1, and the 'background' points as number 0 in the matrix (like a binary map):

$$b_{i,j} = \begin{cases} 1, & f_{i,j} \geq T i = N_x, ..., N_x + 2^n - 1 \\ 0, & f_{i,j} < T j = N_y, ..., N_y + 2^m - 1 \end{cases} \tag{4.1}$$

where $b_{i,j}$ is the binary field value, and $f_{i,j}$ is the actual field values, T is the value of the threshold, and N_x and N_y represent a corner node of the region of interest (Hodges 1994);

(iv) **Matrix** - The identification process described before will form a binary map as seen in figure 4.2, which is later converted into a hierarchy of levels called "data hierarchy." They are linked together by the neighbour finding technique;

(v) **Boundary Points** - So far the process does not explain whether the object is leaving or entering the region of interest because the boundary points were not resolved. So, the points outside the region of interest are also identified followed by a filtering process and new labeling. This technique is done so as to understand their relationship with the points which are inside the area of interest;

(vi) **Feature Detection** - The feature detection part of the algorithm identifies suitable points within the binary map for tracking the storms, for example, centroids

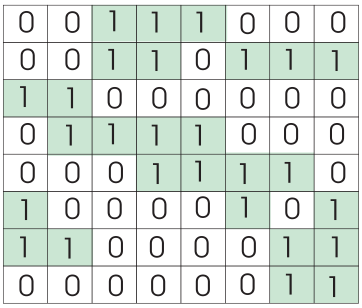

0	0	1	1	1	0	0	0
0	0	1	1	0	1	1	1
1	1	0	0	0	0	0	0
0	1	1	1	1	0	0	0
0	0	0	1	1	1	1	0
1	0	0	0	0	1	0	1
1	1	0	0	0	0	1	1
0	0	0	0	0	0	1	1

Figure 4.2: *An example binary map consisting of object (1) and background (0) points. This matrix is considered the level 0. The other levels (1, 2...) are built by combining quads for level 0. All of the levels form the data hierarchy.*

or local extrema within each object, by comparing each object point with its neighbours. If clusters of object points are found, their centroid is detected and the cluster is represented by a single feature point. The position of the feature point and the point value (local maximum or minimum) are recorded;

(vii) **Correspondence** - After the first frame is analyzed as described above, the next frame (time step) undergoes the same procedures. The problem now is to link the points from the first to the second frame, this is called the 'correspondence' problem. In order to solve the correspondence between the feature points in consecutive frames, the cost function is applied (discussed in Appendix A).

4.2.2 Output from the Tracking Algorithm

The tracking algorithm developed by Hodges (1994, 1995, 1996, 1999) gives different statistical outputs, such as the regions where the storms start, develop and die out. These results may be plotted in different projections and the software used to plot the results was Matlab[2], which is a software package for high-performance numerical computation and visualization, developed by the MathWorks, Inc. It is important to emphasize that semi-stationary storms, less than 10° total displacement, and short-lived storms, with a lifetime less than 2 days, are removed. A description of the different outputs and their units are presented below:

(i) **Genesis Density** - It shows the areas where the largest densities of cyclogenesis are, that is, where the low pressure systems start: the baroclinic generation zones. It is computed from the starting points of the tracks and it does not include any tracks that start at the first time step in the time series of each season. It has

---

[2] The name $Matlab^{TM}$ stands for MATrix LABoratory.

units[3] of $1x10^6 km^2$ per summer;

(ii) **Track Density** - It gives the number of storm tracks through a region per season. It uses a single point from each track that is closest to the estimation point. In this case, a low pressure system is counted just once for each area studied. Hence, it is the amount of low pressure tracks and not the low pressure centers that matters here. It has units of $1x10^6 km^2$ per summer;

(iii) **Feature Density** - Opposed to the track density, the feature density shows the highest density of low pressure *centers*. It uses all points along a track, each center, in each time step, is considered. This will give a density of low centers per season (same unit $1x10^6 km^2$ per summer). For example, if a value of 120 is measured, that means that in an area of 1 million km^2, 120 low pressure centers were counted during one season. This way, slow moving systems will contribute more to the density in a small region due to higher density of points;

(iv) **Lysis Density** - This output is related to the cyclolysis, that is, the areas where a low pressure system dies out. This happens when the pressure in the center of the system is higher than a threshold. It is computed from all end points of the tracks excluding any tracks that end at the last time step. It has the same unit as in the previous densities;

(v) **Intensity** - It shows the intensity of the low pressure systems. The mean intensity is computed from the depth of the feature points and it has units of $10^{-5} s^{-1}$;

(vi) **Mean Speed** - It gives the mean speed of the storm tracks measured in m/s;

(vii) **Mean Longitudinal Velocity Component** - This is related to the **u** component of the cyclone velocity. This parameter is measured in m/s;

(viii) **Mean Latitudinal Velocity Component** - This is the **v** component of the cyclone velocity. The unit is also in m/s;

(ix) **Mean Lifetime** - This output gives the number of days that the mean low pressure system lasted. It is measured in number of days;

(x) **Mean Growth/Decay Rate** - This variable represents the variation of the vorticity field within 6 hours, that is, positive values would indicate that the storm field is filling and that it is intensifying. The unit is day^{-1};

(xi) **Tendency** - The tendency shows how much the vorticity field has changed within an hour. It is measured in $hour^{-1}$.

---

[3] The scaling is related to a number density per month per unit area as in Hoskins and Hodges (2002), where the unit area is considered to be 5° spherical cap, which is around $10^6 km^2$.

4.3 Selected Regions

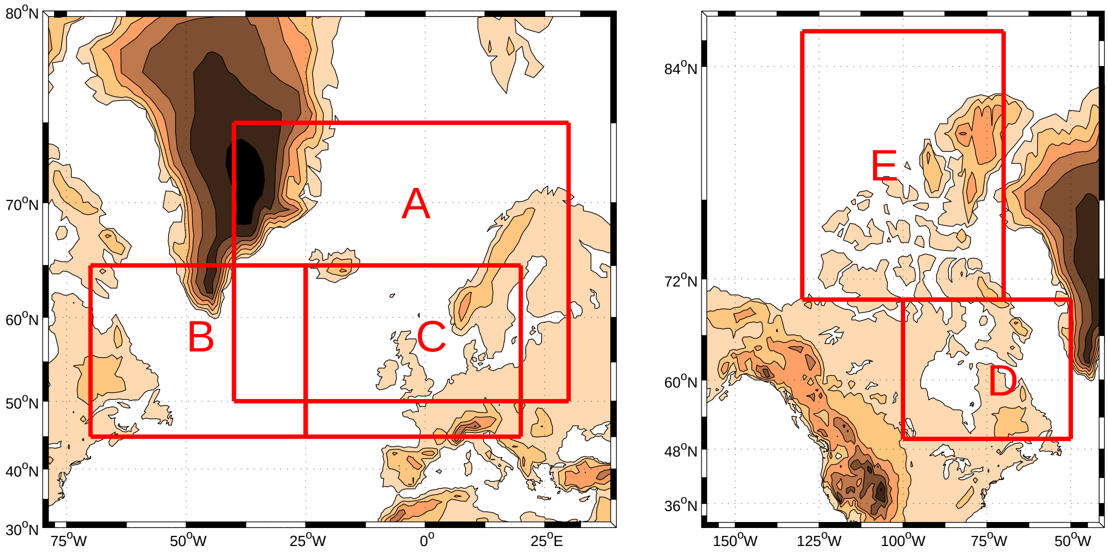

Figure 4.3: The three regions in the North Atlantic and the two in North America studied in this paper: A - lat $50^\circ - 75^\circ N$, lon $40^\circ W - 30^\circ E$; B - lat $45^\circ - 65^\circ N$, lon $70^\circ - 25^\circ W$; C - lat $45^\circ - 65^\circ N$, lon $25^\circ W - 20^\circ W$; D - lat $50^\circ - 70^\circ N$, lon $100^\circ W - 50^\circ W$; E - lat $70^\circ - 85^\circ N$, lon $130^\circ W - 70^\circ W$.

.

Some climatological analysis were made by considering 5 regions in the Northern Hemisphere: 3 in the North Atlantic and 2 in the Arctic (Figure 4.3). These regions were chosen for studying the time variability of the track density and track intensity, and the relation between the summer extra-tropical storm track density and intensity to the large-scale flow. The regions selected are:

(i) **Region A** ($40^\circ W 30^\circ E, 50^\circ N 75^\circ N$) - was selected in order to understand the variability in the summer storms related to Scandinavia, Great Britain and Iceland areas. This region is also important because it covers must of the sub-polar gyre and it is a turning point for the Gulf Stream;

(ii) **Region B** ($70^\circ W 25^\circ W, 45^\circ N 65^\circ N$) - was selected because it encompasses the main features of the maximum localized over the North Atlantic[4];

(iii) **Region C** ($25^\circ W 20^\circ E, 45^\circ N 65^\circ N$) - The same purpose as for region B. Regions B and C were divided into two, in order to understand their differences and to increase the resolution of the averaging for the statistical analysis;

---

[4] See figure 5.1(b).

(iv) **Region D** ($100°W50°W, 50°N70°N$) - this region comprises the area over the Hudson Bay, which seems to be a region of enhanced storm track activity in the summer (when compared to the winter season, as it will be shown);

(v) **Region E** ($130°W70°W, 70°N85°N$) - This area includes part of the Arctic region. It is important to study the changes there, since it has been shown that there is a substantial decrease in the amount of sea-ice over that area (Meier et al. 2005).

4.4 Relation to the Large-Scale Flow

In order to investigate relations between storm track variability in the selected region and the large-scale flow, we have chosen to use the most prominent teleconnection patterns as a representative for the large-scale flow.

One of the procedures used to identify the Northern Hemisphere teleconnection patterns and indices is the Rotated Principal Component Analysis - RPCA as in Barnston and Livezey (1987). The calculation and the data can be obtained at (NOAA , $http://www.cpc.ncep.noaa.gov/data/teledoc/telepatcalc.shtml$) and (NOAA-CIRES 2004, $http://www.cdc.noaa.gov/ClimateIndices/List/index.html$).

A liner regression model[5] was used in order to describe which and how much of the storm track variability is explained by the most influential teleconnection patterns for the summertime. Barnston and Livezey (1987) present a table (See table 4.1) with values of the different teleconnection indexes and the season/months in which they are most influential. The indexes which are important for June, July and August are:

(i) **NAO** - North Atlantic Oscillation - with tabulated values: 3 (June), 3 (July) and 2 (August);

(ii) **EA-JET** - East Atlantic Jet - with tabulated values: 7 (June), 3 (July) and 7 (August);

(iii) **WP** - West Pacific Pattern - tabulated values: 6 (June), 7 (July) and 8 (August);

(iv) **PT** - Pacific Transition Pattern - tabulated values: 4 (June), 4 (July) and 4 (August);

(v) **NP** - North Pacific - tabulated values: 2 (June), 6 (July) and 0 (August);

(vi) **Asian Summer** - tabulated values: 5 (June), 5 (July) and 5 (August).

---

[5] The software used for these models is called R, from The R Development Core Team, which is a powerful statistical program.

Table 4.1: Calendar months when specific teleconnection patterns are important. Adapted from Barnston and Livezey (1987).

Pattern	**Dec**	**Jan**	**Feb**	**Mar**	**Apr**	**May**	**Jun**	**Jul**	**Aug**	**Sep**	**Oct**	**Nov**
NAO	2	2	3	1	1	2	3	2	2	5	1	1
EA	6	6	7	6	10	–	–	–	–	8	7	5
EA-JET	–	–	–	–	6	9	7	3	7	–	–	–
WP	4	3	4	3	4	4	6	7	8	10	4	6
EP	9	10	9	10	8	3	1	1	–	–	6	9
NP	–	–	–	2	2	1	2	6	–	–	–	–
PNA	3	1	2	5	5	10	–	–	6	6	5	2
EATL/WRUS	7	8	10	7	9	7	–	–	–	7	3	4
SCAND	5	9	8	8	3	5	–	–	10	1	2	3
POLAR-EURASIA	1	4	1	–	–	–	–	–	–	–	–	–
TNH	8	7	–	–	–	–	–	–	–	–	–	8
PT	–	–	–	–	–	8	4	4	4	–	–	–
ASIAN SUMMER	–	–	–	–	–	–	5	5	5	–	–	–

(i) Tabulated values indicate the mode number of the pattern for that calendar month (i.e., a 1 indicates that the pattern appears as the leading rotated mode during the month, etc...). No value is plotted when a pattern does not appear as a leading rotated mode in a given calendar month.

(ii) The acronyms used here stand for: NAO - North Atlantic Oscillation; EA - East Atlantic; EA-JET - East Atlantic Jet; WP - West Pacific Pattern; EP - Eastern Pacific; NP - North Pacific; PNA - Pacific North Atlantic; EATL-WRUS - The East Atlantic / West Russia; SCAND - Scandinavia Pattern; POLAR-EURASIA - Polar Eurasia Pattern; TNH - Tropical/Northern Hemisphere pattern; PT - Pacific Transition Pattern; ASIAN SUMMER - Asian Summer Pattern.

(iii) Adapted from the NOAA Climate Prediction Center, retrieved in August 2004 from *http* : *//www.cpc.ncep.noaa.gov/data/teledoc/teletab.gif*.

Hence, some track variables of the summer storms were regressed against the following teleconnection patterns[6]: NAO, EA-JET, WP, EP, NP, PT, the Asian Summer and the AMO[7]. The latter was not included in the table by Barnston and Livezey (1987), it is an index related to the Atlantic SST and not directly related to the atmosphere. However, this index has been used not only for oceanographic purposes but also for atmospheric studies (including summer studies) (Sutton and Hodson 2005), and this is why we decided to include it in this research.

---

[6] See subsection 6.3.1 (Chapter 6) for more information on each of these patterns.

[7] AMO stands for the Atlantic Multidecadal Oscillation.

Chapter 5

Climatology

This chapter presents the main features of the climatology of the extra-tropical summer storms in the Northern Hemisphere. The tracking algorithm by Hodges (1994, 1995, 1996, 1999) has been applied to relative vorticity in 850hPa from 1948 to 2002 (NCEP/NCAR reanalysis).

First, a general overview of different variables will be shown: genesis density, track density, feature density, lysis density, mean intensity, mean speed, mean longitudinal velocity component, mean latitudinal velocity component, mean lifetime, mean growth/decay rate and tendency. Later, the difference between winter and summer storm track climatology will be analyzed.

5.1 Climatology of the Main Variables

For the genesis density variable, it is found that the main regions for cyclogenesis is associated with orographic features. Figure 5.1 (a) shows the genesis density for the summer (JJA), which identifies where the low pressure systems were formed. It is observed that the lee side of the Rocky Mountains[1] sector is the main region where the storms are generated. This baroclinic generation zone comprises a large area which goes from the United States to Canada. Within this region, there are two main zones of maximum values. Another important generation zone is on the lee side of the Appalachian mountains extending to the southern coast of Greenland. The fact that these two regions are the main baroclinic generation areas in the Northern hemisphere is due to the conservation of potential vorticity, where the flow would be cyclonic immediately ‘to the east of the barrier’ (Bluestein 1993; Byrkjedal 2002; Holton 2004).

There are also other important regions, on a smaller scale, which contribute to the generation of storms in the Northern Hemisphere. For example, there is a zone in the northern part of the Baltic Sea. This generation zone may be the result of the influence

---

[1] See the map in figure 3.4.

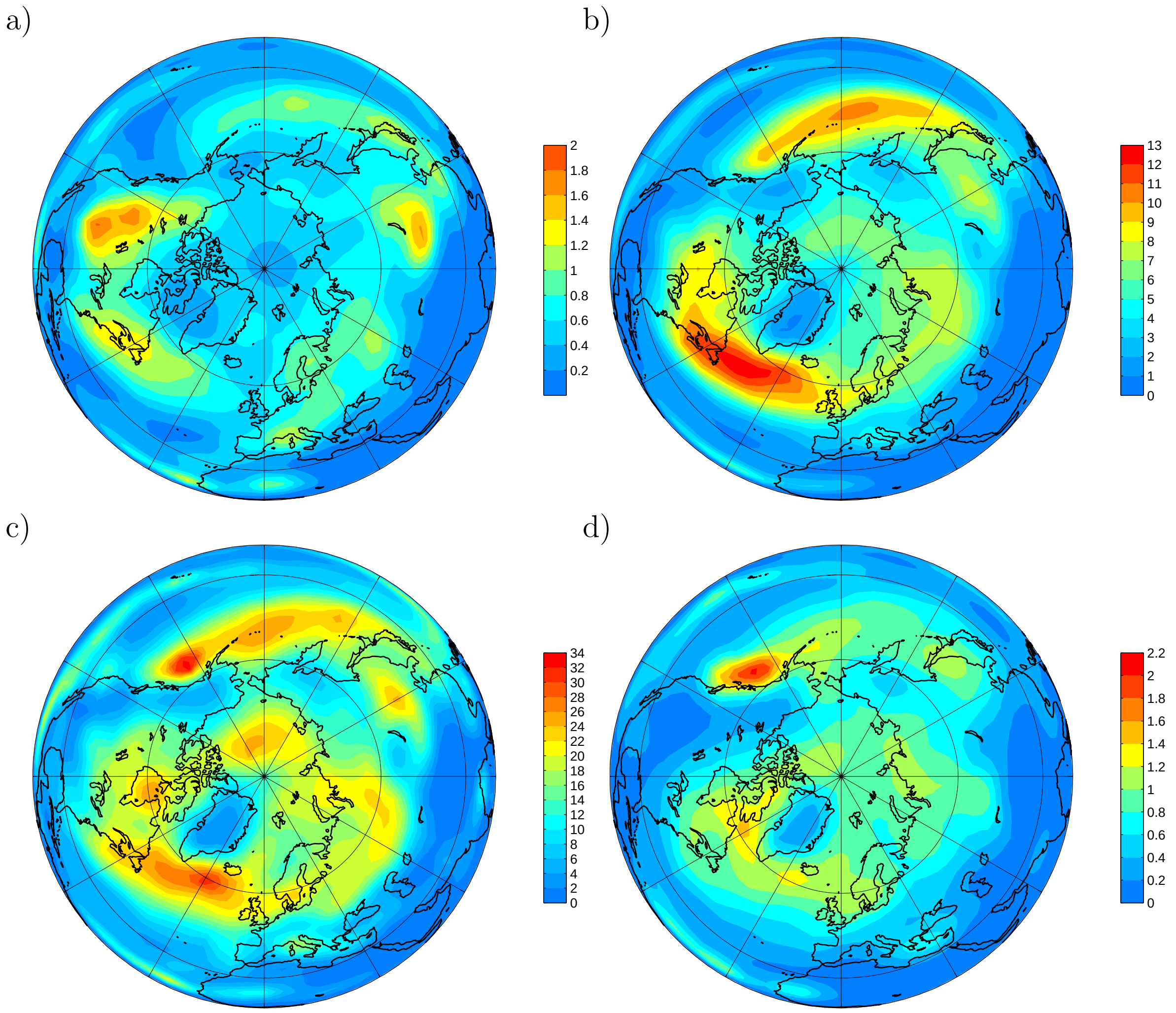

Figure 5.1: *Climatology of summer (JJA) storm tracks in the Northern Hemisphere from 1948 to 2002: (a) The genesis density; (b) The track density; (c) The feature density and (d) The lysis density.*

of the mountains in Norway and because of the warmer temperatures of the Baltic Sea. Even though the genesis density values are not very high over there, it is a region that may influence other parts of Europe, or they may help feed the existing storms that had traveled from North America into Europe.

Another sector where the genesis density is high is over the Mediterranean Sea, close to Italy. The mountains over Spain, Meseta and Pyrenees, may suggest an orographic influence for cyclogenesis in that area. Besides that, the warm waters of the Mediterranean Sea could probably be a new source of diabatic heating for feeding new storms there. In Eastern Europe, east of the Ural Mountains, there is another region of high baroclinicity. Other parts of Asia and the Pacific are also important for the cyclogenesis in the Northern Hemisphere.

Carlson (1991) points out the main baroclinic zones in the Northern Hemisphere:

> In all seasons, the principal sites for cyclone development occur over the western side of the Atlantic Ocean, in the lee of two North American mountain chains (the Rocky Mountains and the Appalachian mountains) and over the Great Plains...south of Greenland over the Atlantic Ocean (40 to 60°N), and over the northern Pacific Ocean south of Alaska (55° N, 140° W).

Thus, the application of the tracking algorithm to 850hPa-vorticity field confirms the same regions as the main sites of genesis density in the Northern Hemisphere in summer. In most of these sites, the flow over mountains favor the generation of waves, due to the conservation of potential vorticity, which consequently will cause convergence in low levels and divergence in higher ones: propitiatory conditions for low pressure vortices.

For the track density variable, the investigation shows that the main areas of location of the summer storms are over the North Pacific and the North Atlantic. Figure 5.1 (b) displays the mean summer (JJA) track density, which is the number of tracks per month per unit area: it represents the spread of the storm tracks, that is, their preferred 'paths'. Three regions of maxima seem to be dominant during the summer season in the Northern Hemisphere:

(i) A region which starts on the eastern part of the United States right after the Rocky Mountains and up towards the Hudson Bay and Appalachian Mountains. Over Quebec, Newfoundland and the Labrador sea, the number of tracks increase to its maximum values. Then, a large band from the east coast of Canada crosses the whole Northern Atlantic. This band goes to the areas between Iceland and England reaching the southern parts of Norway and Sweden;

(ii) A second region is not only a continuation of the maxima over the North Atlantic, but it may also be fed by the high genesis densities which were observed over the Baltic Sea and the Ural Mountains. Thus, these main generation zones may feed the storms that already come from North America in a way that they move on towards the northern parts of Europe and Asia and up to the Arctic. There is almost a circular pattern over the Northern Hemisphere of the storms that begin in North America and go to the Arctic region. The downstream development process contributes to this picture.

(iii) Another important maxima is over the North Pacific. These storms start from Asia crossing the whole North Pacific until the Gulf of Alaska.

The results of the feature density variable are quite similar to the track density plot. The feature density (Figure 5.1 (c)), which is the number of low pressure centers in a region, is an important variable because it represents the contribution of the slow moving systems, that is, when a low pressure is slow, it will enhance the feature density, thus increasing the number of low pressure centers over an area. The tracks would reside in a region over several time steps and they would be counted several times. Maximum values of feature densities can be seen in the region over the Hudson Bay and Victoria and Parry islands. These two areas were also selected as separate regions to be studied and the results will be presented in the next chapter (regions D and E). The fact that the feature density is not so high right east of the lee side of the Rocky Mountains, as it is for the track density plot, is due to the fact that these storms are fast moving and therefore, do not contribute to a high number of feature density.

There is also a maximum through most of the North Atlantic coming from the Appalachian Mountains. The highest values are found close to Iceland. After that, there seems to be a bimodal shape in the feature density plot over the Norwegian Sea. Some of these storms go to the southern part of Scandinavia, while others travel towards Svalbard, a feature not captured by the track density. The southern parts of Norway and Sweden have also high values of low pressure centers. The other main regions are over parts of northern Europe and east of the Ural mountains. These low pressure centers travel northwards from there to the Arctic region. Enhanced values are found in the Arctic region between 75°-85°N, 110°W-100°E.

High values of feature density are also observed through parts of China and Mongolia, and in the Northern Pacific, especially close to the Gulf of Alaska. There are some other areas in the Northern Hemisphere of high values of feature density, but they are not so enhanced as over the main zones pointed out here. One place of enhanced values that is worth mentioning is over Italy, and that may be because of the fact that there is a baroclinic generation zone there, as it was mentioned before.

For the lysis density, the region around the pole seems to be the most preferable place. The lysis density (Figure 5.1 (d)) represents the zones where the storm tracks die out. This is an important feature of the description of the storm track climatology, since it gives an idea of how much the storm tracks traveled. These main regions where the storms 'prefer' to die out during summer are:

(i) A zone close to the Hudson Bay and the north-eastern part of Canada. As it was observed in the feature density description, this is near areas of enhanced feature density values, that is, the storms started to slow down, thus enhancing the feature density and then they died out. Hence, storm tracks over this area did not travel a lot, they probably did not have enough energy to travel much further;

(ii) Along most the North Atlantic, the storms die out in different rates, with a maximum close to Iceland. This region is also connected to the enhanced feature density over there: the storms slowed down and died out. Something interesting is that the bimodal process seen in the feature density is also seen here: most of the storms which venture to Svalbard die out in the middle of the process. The ones which venture towards southern Scandinavia die out there. However, the storms that survive can probably be fed by the high baroclinic generation zone in the Baltic Sea and move on;

(iii) Over parts of Northern Europe: It is seen that the storms east of the Ural mountains die out not much far away from there. Over the Arctic, the storms die out closer to the Northern coast of Greenland, between 80°-180°W;

(iv) Two areas over Asia and the North Pacific: The storms which crossed the North Pacific die out mainly on the coast in the Gulf of Alaska, which is also confirmed by the enhanced values of feature density in that region.

The results for the intensity of the storms show that higher values are found in high latitudes and through the North Pacific. The intensity (Figure 5.2 (a)) is increased from a circle band that runs from between 45°N to 60°N and most of the Arctic. In North America, the highest values are over the Hudson Bay, the Foxe Basin and the Hudson Strait. The higher temperatures in those areas promote cyclogenesis and thus the intensity of the storm tracks[2]. Other areas are also in the north-eastern part of Quebec, the Gulf of Saint Lawrence, Newfoundland and the Labrador Sea. Over most of the eastern part of Canada and in the United States, mainly over the New York State and Maine, the intensity is also enhanced.

In the North Atlantic, the intensity is also elevated from the east coast of Canada to Iceland and the west coast of the British Isles. There is, thus, a small area of maximum intensity close to Iceland between 50° and 60°N. Over Greenland, there is no intense activity, as it would be expected, since the cold temperatures suppress the storm tracks from crossing this region.

In most parts of Europe, the intensity ranges from 3 to around 4 x $10^{-5}s^{-1}$. The highest values are over Southern Norway, and the Russian Federation, going up to the Arctic region through the Barents and Kara Seas. In the Arctic, the storm intensity also varies from 3 to 4 x$10^{-5}s^{-1}$. The intensity is enhanced in almost all of the Arctic area from the Nansen Basin to the Canada Basin and back to North America. The highest values are between 70°-80°N, 150°W-150°E.

In Asia, the intensity is not so enhanced. The most prominent values are over China, Mongolia, Taiwan and Japan. However, the North Pacific has elevated values

---

[2] Serreze (1995) when referring to summer storms pointed out that: "...increased cyclonic activity over Eurasia, as well as Canada, appears to be related to development of a climatological Arctic frontal zone, separate from the Polar front" and he also found out that "...local diabatic heating associated with open water areas within the ice cover can be significant and in some cases might contribute to rejuvenation."

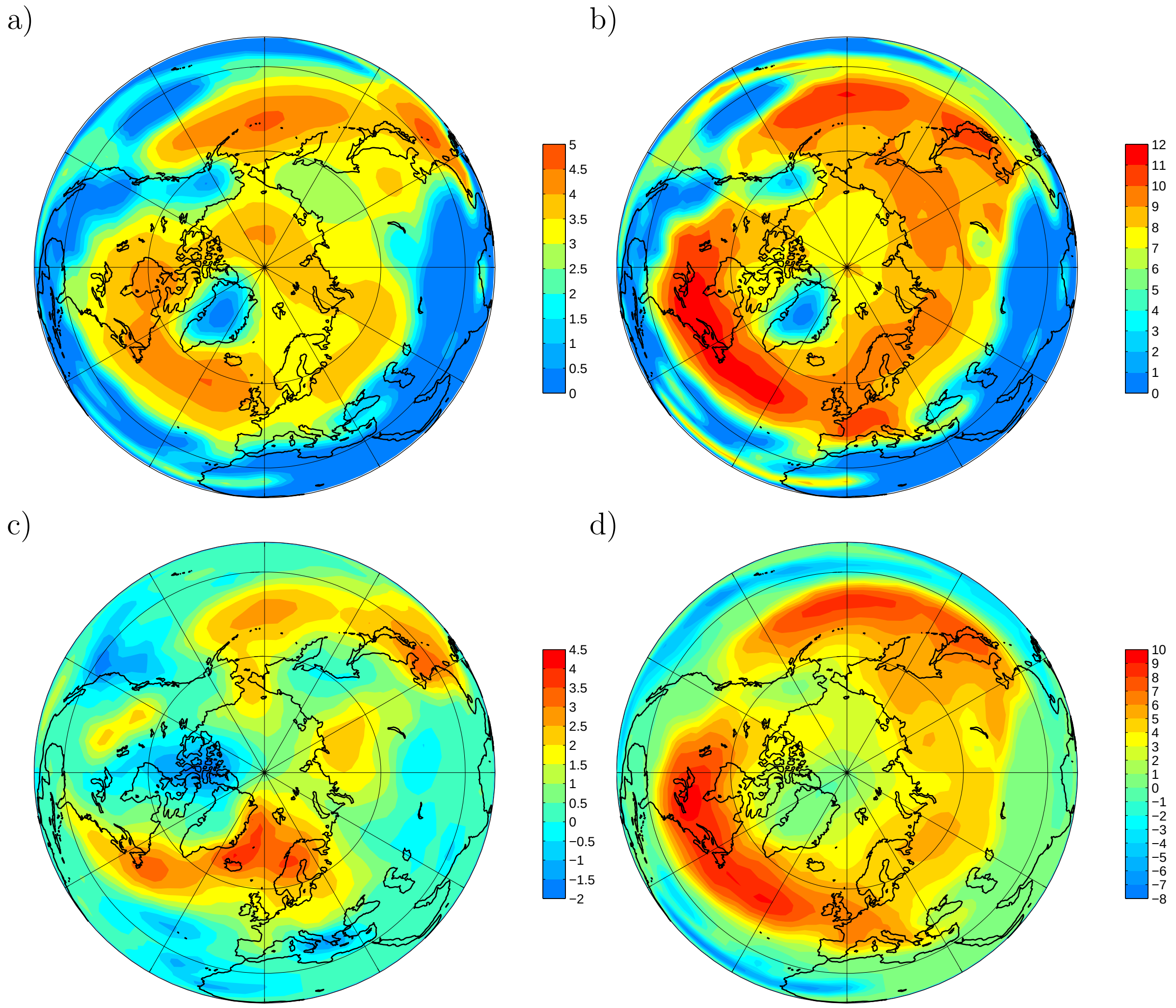

Figure 5.2: *Climatology of summer (JJA) storm tracks for the Northern Hemisphere from 1948 to 2002: (a) The mean intensity; (b) The mean speed; (c) The mean longitudinal velocity component ($\boldsymbol{v}$) and (d) The mean latitudinal velocity component ($\mathbf{u}$).*

compared to the ones in the North Atlantic. There are two enhanced points there: one over Taiwan and the Philipines and the other over the Bearing Sea.

As for the mean speed, the areas of high values are mainly through the Eastern US and Western North Atlantic and over the North Pacific. The mean speed (Figure 5.2 (b)) of the storm tracks follow a similar pattern to that of the intensity. In North America, the speed of most of the storms vary from 7 to 12 ms^{-1}. The regions where the velocity is mostly enhanced is over the Beaufort Sea, the Victoria Islands, Parry Islands, the Northwest Territories in Canada and the Hudson Bay. The highest values are over Alberta, Ontario, Quebec, Lake Michigan, New York, Maine, Newfoundland and the Labrador Sea.

The mean speed reaches its maximum values over most of the North Atlantic, especially between 40°-60°N, 60°-20°W. In Europe, the speed of the storm tracks is not so enhanced as it is in North America and in the North Atlantic. High values, from 10 to 12 ms^{-1} are over France, Belgium, Holland, Germany and Austria. In most other places in Europe, the speed ranges from 7 to 10 ms^{-1}. In most parts of Scandinavia and the northern region of the Russian Federation the speed is from 9 to 10 ms^{-1}. These amounts are also found in parts of Asia, for example, in Mongolia, China, South and North Korea. In most parts of Japan, the velocity of the storms reach values from 10 to 12 ms^{-1}.

In most of the North Pacific, the speed of the storms is also compared to the magnitude of the storms over the North Atlantic, but they seem to be a bit slower. The most enhanced amounts are between 30°-50°N, 150°W-165°E.

For the mean longitudinal velocity component, the results show a characteristic band from the north-east coast of the United States to east coast of Greenland. The mean longitudinal velocity component (Figure 5.2 (c)) has its maximum values close to the Rocky Mountains. Then, on the east coast of the United States and Canada, the velocity varies from 1.5 to 3 ms^{-1}, from Florida to Newfoundland and Labrador. In the North Atlantic, the enhanced values are tilted towards the Denmark Strait, between Greenland and Iceland. Values between 3 to 4.5 ms^{-1} are found in the Greenland Basin, the Norwegian Basin and covering most parts of Scandinavia. Values between 1 to 2.5 ms^{-1} are also found through the Russian Federation between 55°-80°N, 70°E-120°E.

Over the Pacific Ocean, the velocity reaches high values close to the east coast of China, North and South Korea and in most parts of Japan. Besides that, another important sector is between 60°-30°N, 150°E-150°W. The mean longitudinal velocity component is also enhanced over the Bering Strait.

The mean latitudinal velocity component plots follow a similar characteristic as for the mean speed. The mean latitudinal velocity component (Figure 5.2(d)) presents a feature of two main enhanced regions: in the North Atlantic and in the North Pacific with values ranging from 3 up to 10 ms^{-1}. In North America, high values are over most parts of Canada, the Hudson Bay, Lake Michigan, Lake Superior (where the velocity reaches its peak of 10 ms^{-1}), parts of the east coast of the United States and the Newfoundland and Labrador. In the North Atlantic, the mean longitudinal velocity component ranges from 6 to 10 ms^{-1} in a band which goes from 40°-60°N to 60°-10°W.

In Europe, the latitudinal velocity component seems to slow down, its values range from between 3 to 7 ms^{-1}. In the United Kingdom, France, Belgium, Holland and Germany, the values are from 6 to 7 ms^{-1}. Over southern parts of Norway, Sweden and parts of the Russian Federation, the mean latitudinal velocity component is from 5 to 6 ms^{-1}. In most of the east coast of Asia, the latitudinal velocity is also very enhanced, especially in Japan where it ranges from between 8 to 9 ms^{-1}. This is also true in a band which goes over the North Pacific in the same latitude where Japan is situated, with peak values of between 9 to $10ms^{-1}$, between the longitudes of 170°E-170°W.

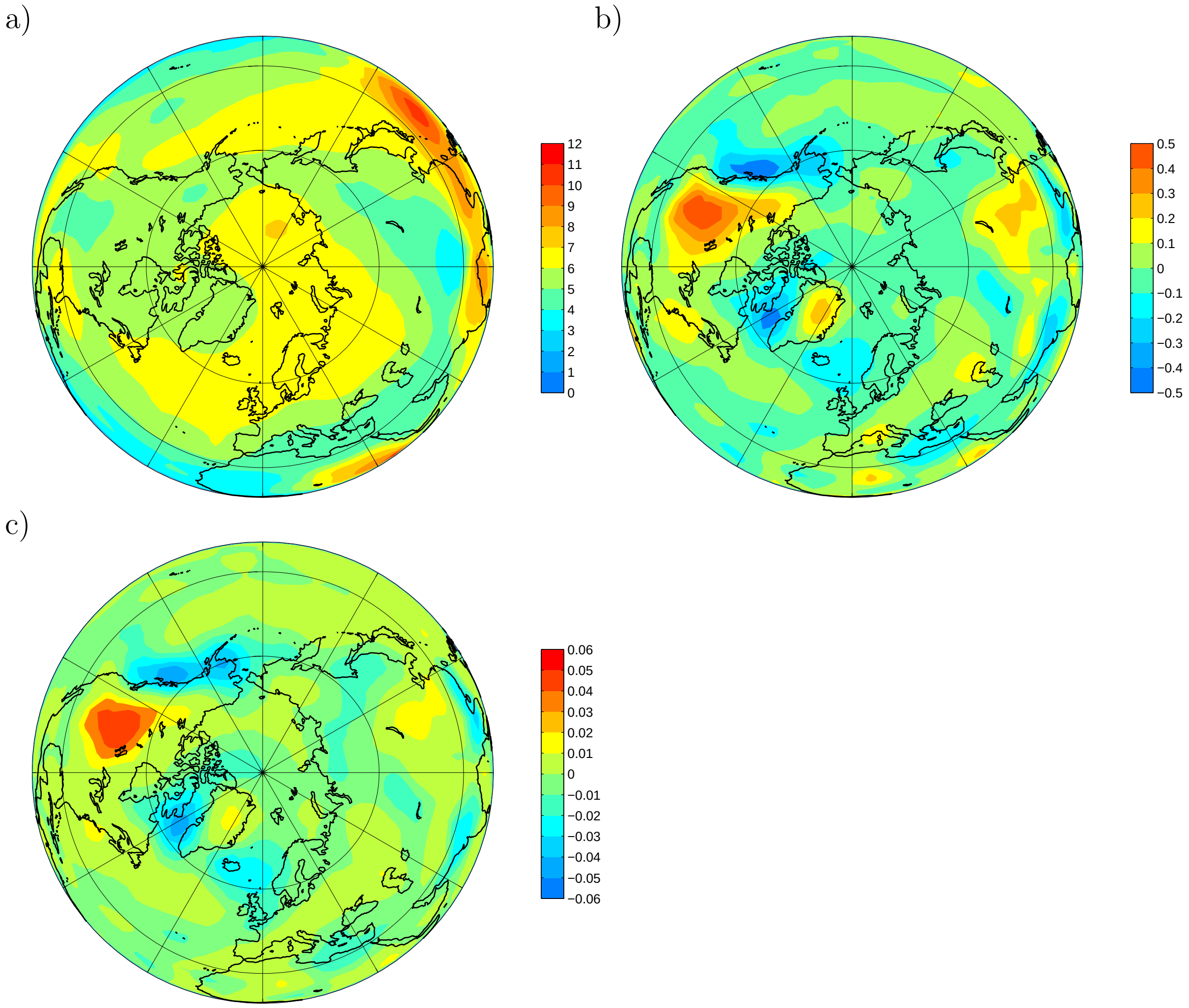

Figure 5.3: *Summer Climatology of the storm tracks in the Northern Hemisphere from 1948 to 2002: (a) The mean lifetime; (b) The mean growth/decay rate and (c) The tendency.*

For the mean lifetime, results show that the values for summer storms is high in most of the Northern Hemisphere and higher than the winter lifetime of the storms. A mean lifetime (Figure 5.3(a)) of 6 or more days is observed in most of the Northern Hemisphere, especially in the North Atlantic, Scandinavia, the Greenland Sea, the Arctic and most of the North Pacific. In North America, the mean lifetime values vary from 3 to 6 days. In California, over the Gulf of Boothia (in Canada), the Newfoundland, the Labrador Sea and the south-eastern coast of the United States, the mean lifetime is from 6 to 7 days. In the North Atlantic, most of the storms last from 6 to 7 days. In the southern part of Europe, they last for 5 to 6 days, while in the northern part, they last from 6 to 7 days. This is is also the case in eastern Europe. In the Arctic, they last from between 6 to 8 days, specially close to the New Siberia Islands. Closer to the tropics, south of Japan, the storms last from 6 up to 12 days. Near Japan and most of the North Pacific, they are from between 6 to 7 days.

Thus, the leading north hemispheric lifetime is 5-7 days (Figure 5.4) for the summer season. Long-living cyclones, with lifetimes longer than seven days, make up a total of 5% of the cyclones in the Northern Hemisphere, 40% of the cyclones exist from 2 to 4 days and 55% of them exist from 5 to 7 days. These results for the summer season are quite different from the results for the winter season obtained by Gulev et al. (2001)[3], where they found that 50% of all cyclones exist from one to four days and 17% of cyclones are long-living, with lifetimes longer than 7 days.

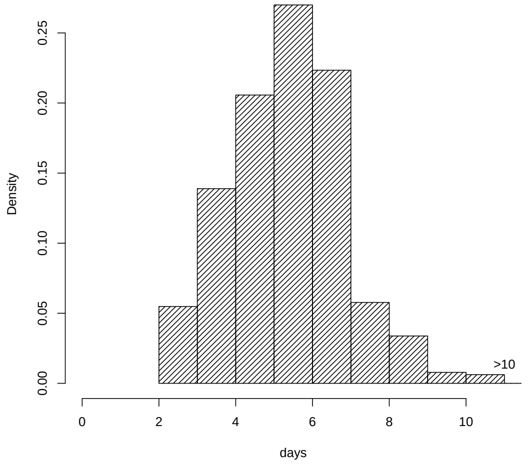

Figure 5.4: Summer climatological occurrence histogram of cyclone lifetime for the Northern Hemisphere. The threshold used by the tracking algorithm is 2 days.

The mean growth rate results show enhanced values mainly in the United States. The highest values of the mean growth rate (Figure 5.3(b)) are indeed over North America right east of the Rocky Mountains. They are also found over the east coast of the United States and Canada. However, the tendency is not so enhanced in the North Atlantic. In Europe, the mean growth rate is high over most parts of southern Europe, especially in France and Italy. In northern Europe and Scandinavia there is a decay rate (since the values are negative). In eastern Europe and Asia, enhanced values are over the Caspian Sea, the Barents Sea, Mongolia, China and over Japan.

---

[3] Gulev et al. (2001) used NCEP/NCAR SLP data for the Northern Hemisphere from 1958 to 1999. He also used a different approach for counting the storms. The example is mentioned here just as a simple comparison.

The growth rate is not enhanced in the North Pacific. There is, though, a region close to Alaska, the west coast of Canada and the United States, of enhanced decay rate. Another enhanced region of decay rate is over the Davis Strait.

The tendency (Figure 5.3(c)) have similar patterns to the growth/decay rates, showing a strong growth over the Rocky Mountain region: this is one of the most important areas for baroclinic generation in the summer. The enhanced values of negative tendency are found, as in the growth/decay rate, over the west coast of the United States and Canada, and over the Davis Strait. The tendency is positive in almost half of the Arctic.

So far, a climatological overview of the main variables to describe storm tracks was discussed. The great importance of the Rocky Mountains and the Appalachian Mountains for cyclogenesis is clearly apparent. Other features that were presented here are related to enhanced activity over places such as the Hudson Bay, the Labrador Sea, the Baltic Sea, the Barents Sea and some others, to the maintenance of the storm tracks. They provide the storm tracks with the necessary energy to their development, since the temperature in these places are elevated during the summer season. The next subsection will compare the same variables[4] to the situation in the wintertime.

5.2 Difference Between Summer and Winter

In this subsection, the climatology of the difference between summer and winter storms will be discussed with respect to the different variables. The results are presented in figures (left-hand side) 5.6, 5.7 and 5.9. The difference between summer and winter was defined as:

$$Track_{difference} = Var_{jja} - Var_{djf} \tag{5.1}$$

where Var_{jja} represents the variable in the summer season and Var_{djf} is the variable in the wintertime. A statistical test (t-test) was also used to analyze areas where this difference was significant at the 95% confidence interval (See the right-hand side of figures 5.6, 5.7 and 5.9).

For the genesis density difference, the results show that the wintertime values are higher through most of the NH region, except in northern parts of the USA, Canada and parts of Asia. Figure 5.6(a) shows the the genesis density difference between the values of the JJA and DJF seasons. The summer season has higher values in some parts of the plot, for example, over the northern part of the Rocky Mountains, the Appalachian Mountains and the Great Lakes in the United States and Canada. In Canada, this is observed over the Hudson Bay and in the north-western part of the country. The high

---

[4] Appendix D brings the NH average and the standard deviation for each of the variables in both summer and winter seasons.

values for the summer found over the Great Lakes and the Hudson Bay may be due to the fact that there is more open waters (a greater amount of freshwater) due to melting of sea-ice, compared to the winter season. Besides that, the lower level temperature is also elevated in this season (JJA). This would promote evaporation and consequently, a strong region for the development of cyclogenesis. In a paper about summer and winter storms in the Arctic, Serreze (1995) pointed out that during the summer "...local diabatic heating associated with open water areas within the ice cover can be significant, and in some cases might contribute to rejuvenation." Serreze (1995) did not, however, found the cyclogenesis region from western Hudson Bay extending into northern Baffin Island. He mentions that these features were observed by Whittaker and Horn (1984), but that this region was "...not observed in the present data," that is, in his dataset[5].

There is also high activity in parts of Asia and the North Pacific. Right east of the Ural Moutains, the genesis density is higher for the summer season. There are also enhanced values over parts of China and in the Bearing Sea.

For the track density, the winter time values are also higher than the summer ones. However, a stronger than winter dipole is found over Canada and Asia. This dipole pattern indicates a northward shift during summer. In Great Britain and Scandinavia, summer storms seem to be associated with more zonally directed tracks than in winter. The track density (Figure 5.6(b)) shows that there is a pronounced downstream development from the baroclinic generation zones (the genesis density). It is seen that a great amount of tracks are found across the North Atlantic, Great Britain and southern Scandinavia, as well. Two other enhanced areas are on the western side of Asia and on the eastern side of Alaska. The south of Greenland, from 40° to 60°N, is a region prominent to extra-tropical cyclone development because of the strong sea-surface temperature gradients (Carlson 1991) (Figure 5.5).

In North America, there is a small region east of the Rocky Mountains where the number of tracks is high: up to 3 tracks more than those during the winter season. Over the Hudson Bay, the Foxe Basin, the Davis Strain, the Hudson Strait, Quebec, the Labrador Sea and the Newfoundland, the number of tracks are on the order of up to 9 tracks more than in the wintertime. This is also similar over most of the North Atlantic from 50° to 60°N, with values up to 7 storms more during the summer season. In the United Kingdom, southern Norway and Sweden, the values are up to 3 storms more than in the wintertime.

In Asia, the most enhanced features in the summertime are over parts of the Russian Federation, most parts of China, the northern part of Japan and over the Sea of Okhotsk (on the eastern coast of the the Russian Federation). The values over these areas are

---

[5] Serreze (1995) developed his own tracking algorithm and used the MSLP as the tracking variable. One reason why he may not have found the Hudson Bay area in his dataset it is because of the use of the MSLP instead of the vorticity field. The vorticity field, as used in this thesis, detects features much earlier than the MSLP field.

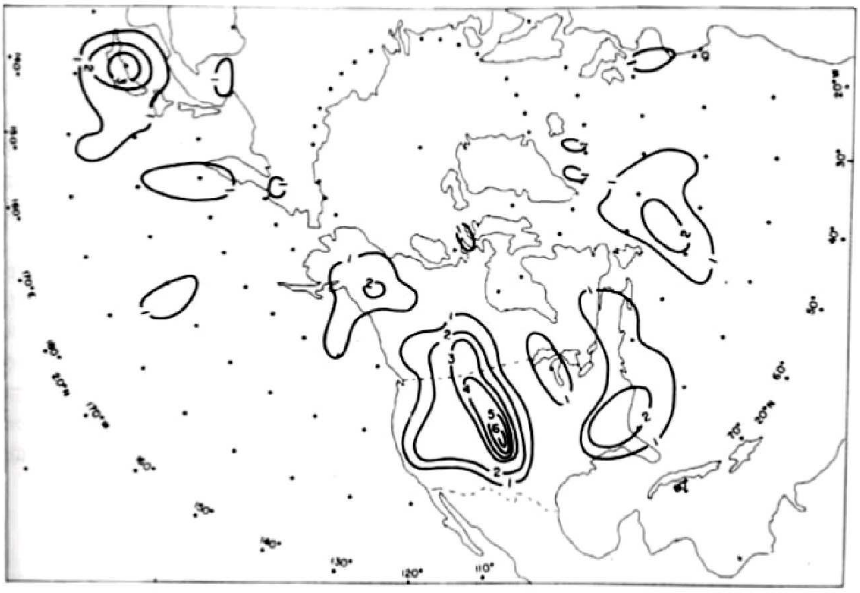

Figure 5.5: *The position of cyclones during the summer from 1976-1982. From Carlson (1991).*

up to even 6 days more than during winter. In the North Pacific, specially over the Bearing Sea, the range of the number of tracks is on the order of 2 to 5 more storms in the summer season.

The feature density plot presents a more homogenous balance between areas where winter dominates summer and vice-versa. Similar regions are also found in the feature density plot (Figure 5.6(c)), but for a broader area. For example, in parts of North America, there are from 6 to 16 more low pressure centers than in the wintertime. There are high values right after the Rocky Mountains, over the Hudson Bay, Quebec and most of the east coast of the United States and Canada. There are also high features through most of the North Atlantic from 35° to 65°N. In Europe, in southern Norway and Sweden, the Baltic Sea and parts of Finland, there are from 6 to 16 more low pressure centers. Some enhanced features are also observed in parts of south and east Europe, in the eastern part of the North Atlantic, most parts of Asia and the North Pacific.

In most parts of Asia, the amount of low pressure centers are higher during summer, there are values of up to 26 more low pressure centers than in the wintertime. This is also the case in the North Pacific, especially close to the Bering Sea and the Gulf of Alaska.

The results for the lysis density show winter values higher than summer over the continents, but higher values during the summer over the oceans. The DJF values are larger for most of the lysis density plot (Figure 5.6(d)). In North America, the only places where the summer values outnumbers the winter ones are over parts of the Baffin

Island (close to the Baffin Bay) and over the Labrador Sea. In the North Atlantic, only areas over the tropical region and on the east coast of Canada between 60°-30°W are seen. In Europe, the most enhanced places are in the southern parts of Norway and Sweden, the northern part of the United Kingdom and parts of the Norwegian and the North Seas. This reinforces the fact that extra-tropical summer storms over the North Atlantic have a preferred path over the North Atlantic and that they die out in Southern Scandinavia, while the winter storms go up between Greenland and Iceland. In Asia, enhanced values are over parts of China, the Russian Federation and Japan. In the North Pacific, high values are only found in the tropical regions and on the west coast of Canada.

The mean intensity is more enhanced during winter, except in some parts of the USA, Canada, Asia and tropical regions. The winter season values are also dominant when it concerns the intensity of the storms (Figure 5.7(a)), as it would be expected. However, this is not the case in some areas close to the Rocky Mountains, over the Hudson Bay, the Foxe Basin, the Hudson Strait and parts of Quebec. Therefore, this makes the Hudson Bay an important region related to the summer storms. In most of the North Atlantic, the winter intensity is higher, but it is only on the order of 1.5 to 2x $10^{-5}s^{-1}$ higher.

However, over Europe, this order is much less with a mean strength value of around 0.5 x$10^{-5}s^{-1}$ higher in winter than in the summer season. Even though the winter storm intensity is higher, this intensity is not much different than in the summer season. In Asia, the storm intensity in the summer is higher in most of the eastern part, for example, in China, Mongolia and parts of the Russian Federation. In the North Pacific, the winter storm values outnumbers the summer ones in an order of around 0.5 to 3 x$10^{-5}s^{-1}$.

More enhanced areas are found in small regions and over tropical areas for the mean speed variable. Figure 5.7(b), the mean speed of the storms, shows that even though winter storms are faster than the summer ones, the difference is not so high in some places. For example, in most parts of the United States, the North Atlantic and Europe, the winter storm speed is of the order of 2 to 4 m/s faster. It is thus much higher than the summer over the southeast part of the United States and over the Atlantic and Pacific Oceans, where the order of the difference may be from 6 up to 10 ms^{-1} higher. The summer season mean speed is more enhanced in a small region close to the Rocky Mountains, over China, Mongolia, parts of the Russian Federation and in most of the tropical Pacific.

There are, however, differences concerning the components of the wind velocity. Figures 5.7(c) and 5.7(d) show the mean longitudinal and latitudinal velocity components, respectively. A dipole pattern over the pole, of values higher in summer than winter, is observed for the mean longitudinal velocity component. In North America, the mean longitudinal velocity component is higher, during the JJA season, over the Queen Elizabeth and Parry Islands, parts of Quebec, over the Newfoundland, the Labrador Sea and the Hudson Bay. In the North Atlantic, the wintertime values are much higher than the summer ones, with the velocity component reaching amounts of around 4 to 6 ms^{-1} orders higher than in the summertime. The difference over Europe is not so enhanced, with an order of around 2 ms^{-1} higher in the wintertime. However, across most regions in the eastern part of Asia, the summer time values of the mean longitudinal velocity are much larger, up to around 4 ms^{-1} higher. This is also the case in the North Pacific, especially close to the Sea of Okhotsk and the Bearing Sea.

For the mean latitudinal component, a “Y” shape is found where values are higher during summer. The mean latitudinal velocity component presents an interesting pattern, that is, it looks as if the Northern Hemisphere was divided into three different regions by the positive values. There is a band coming from the south-east part of USA and up to the North pole. There is also a huge band that captures the whole eastern side of Europe, Scandinavia and it finally crosses parts of Asia. The fact that the winter season latitudinal velocity dominates in the North Atlantic sector confirms that the “preferred paths” for the winter storms curve up between Greenland and Iceland, that is, the velocity is higher making that possible. As discussed before, the summer storms seem to be flatter while crossing the North Atlantic towards southern Scandinavia.

For the mean lifetime, this study shows that summer storms live longer than winter ones, and this is seen in most of the Northern Hemisphere. Figure 5.9(a) shows that the mean lifetime of summer storms is higher than the winter ones in almost the whole Northern Hemisphere, except in parts of the South Atlantic. Some of these storms last 2 or more days more compared to the winter season, for example, the storms over England and parts of Scandinavia. There are also intense gradients in the eastern Pacific as well. It is interesting to note that Guterl (2005) reports that storms in a warmer world last longer, according to model experiments.

In North America, the storms last up to 1.5 days more than in the wintertime. This is also similar in the North Atlantic. In Europe, the highest values are over the United Kingdom and Scandinavia. The difference is not so enhanced through most parts of Asia and the Russian Federation, with values up to around 1.25 days. In the North Pacific, the summer storms last up to 2.25 days more, for instance, over the Gulf of Alaska and on the west coast of Canada. They last up to 2 days in the Arctic region.

The mean growth rate is dominated by winter values being higher than summer, except in some continental areas. The mean growth rate plot (Figure 5.9(b)) emphasizes the role played by the mountainous regions (the Great Mountains and the Appalachian Mountains) in the United States, the seasonal shift in jet position over the Great Lakes and the Hudson Bay, and surface baroclinicity: the mean growth is much larger during the summer for these places. In Europe, the growth rate is higher over Portugal, Spain and most parts of Europe, with the highest values in Germany. In most parts of the Russian Federation and Asia, the values of the growth rate are also higher than during the wintertime. In the North Pacific, the growth rate is also enhanced over the Bering Sea and the Sea of Okhotsk.

For the tendency variable, it is found that this parameter is more enhanced in winter than summer. The most evident exceptions are found in continental areas. The tendency (Figure 5.9(c)) plot shows that the summer values are higher over the whole west coast of the United States and Canada, parts of the Arctic Ocean, Victoria Island, Baffin Island, Hudson Bay, the Davis Strait, the Labrador Sea, Newfoundland, Quebec and the regions around the lakes Superior, Michigan and Huron. In most of the North Atlantic, the tendency is higher in the wintertime. In most parts of Europe, the tendency is higher during the summer, except in the areas around Italy. The values are also larger over the northern part of Asia, and the eastern side of the Russian Federation. The summer values are also enhanced in most of the North Atlantic, especially the regions close to the Bering Sea.

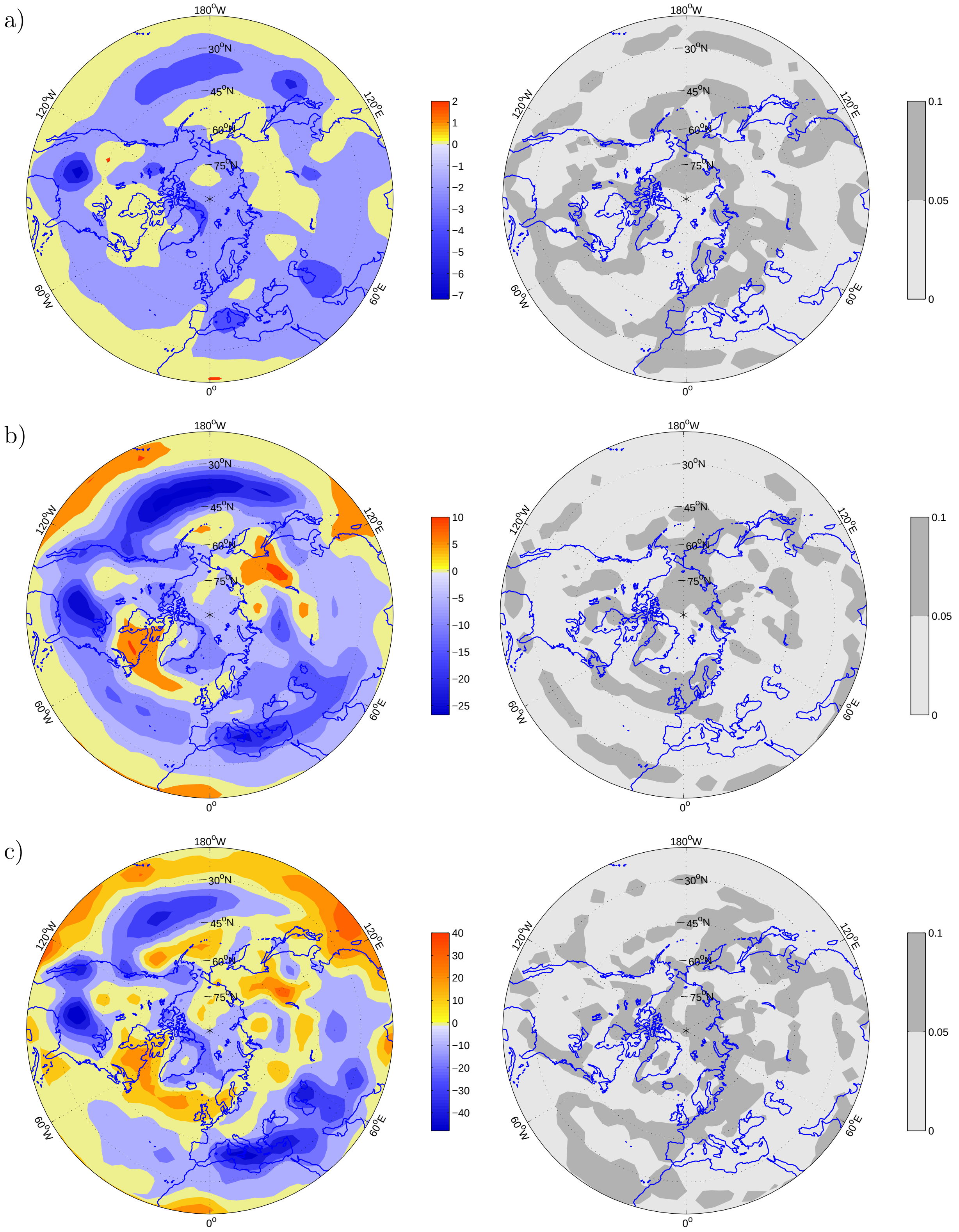

Figure 5.6: *The difference between the JJA and DJF seasons for the Northern Hemisphere from 1949 to 2002: (a) The genesis density; (b) The track density; and (c) The feature density. The right-hand side is a t-test of the difference between summer and winter showing areas where this difference is statistically significant at the 95% confidence interval.*

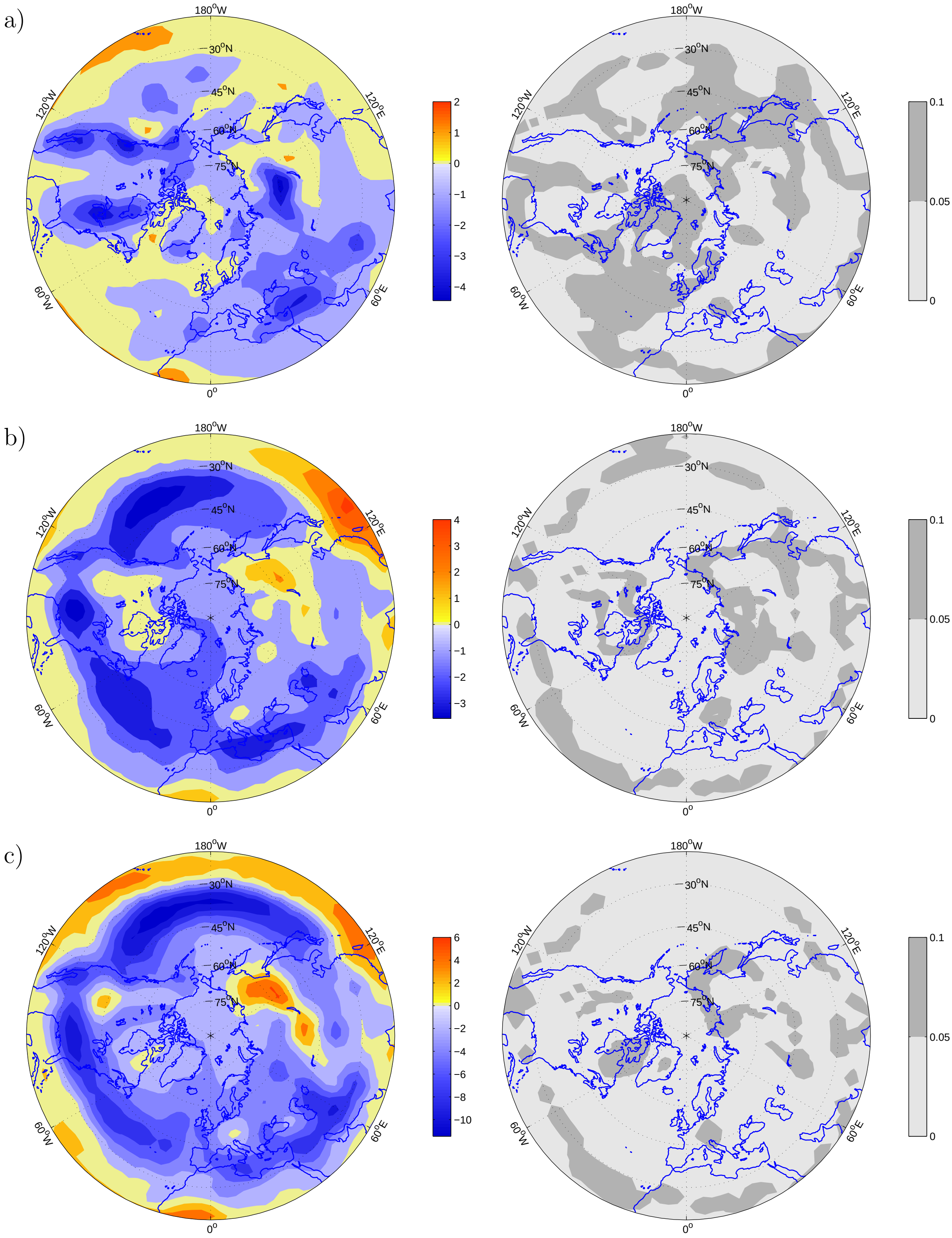

Figure 5.7: *The difference between the JJA and DJF seasons for the Northern Hemisphere from 1949 to 2002: (a) The lysis density; (b) The mean intensity; and (c) The mean speed. The right-hand side is a t-test of the difference between summer and winter showing areas where this difference is statistically significant at the 95% confidence interval.*

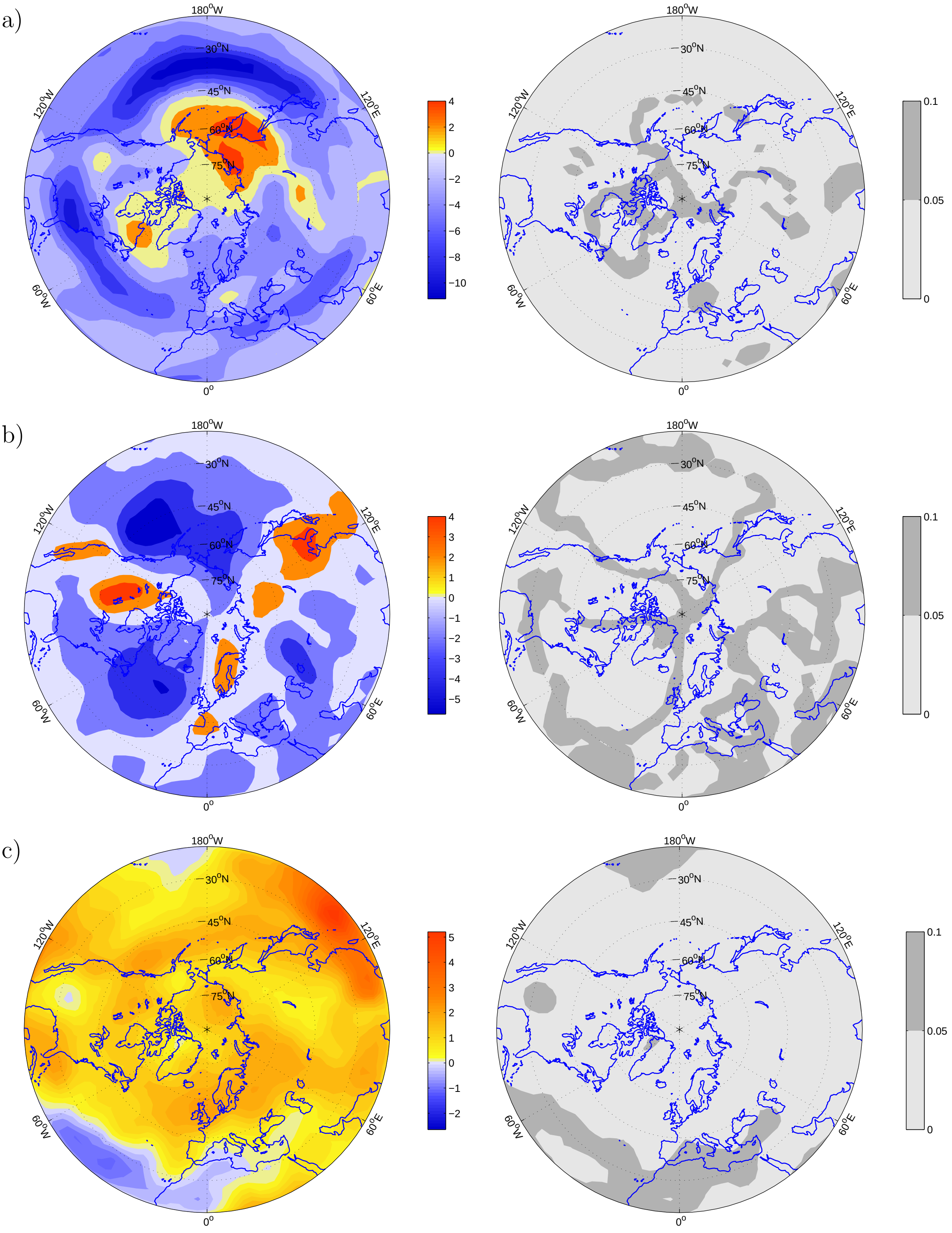

Figure 5.8: *The difference between the JJA and DJF seasons for the Northern Hemisphere from 1949 to 2002: (a) The mean longitudinal velocity component (**v**); (b) The mean latitudinal velocity component (**u**); and (c) The mean lifetime. The right-hand side is a t-test of the difference between summer and winter showing areas where this difference is statistically significant at the 95% confidence interval.*

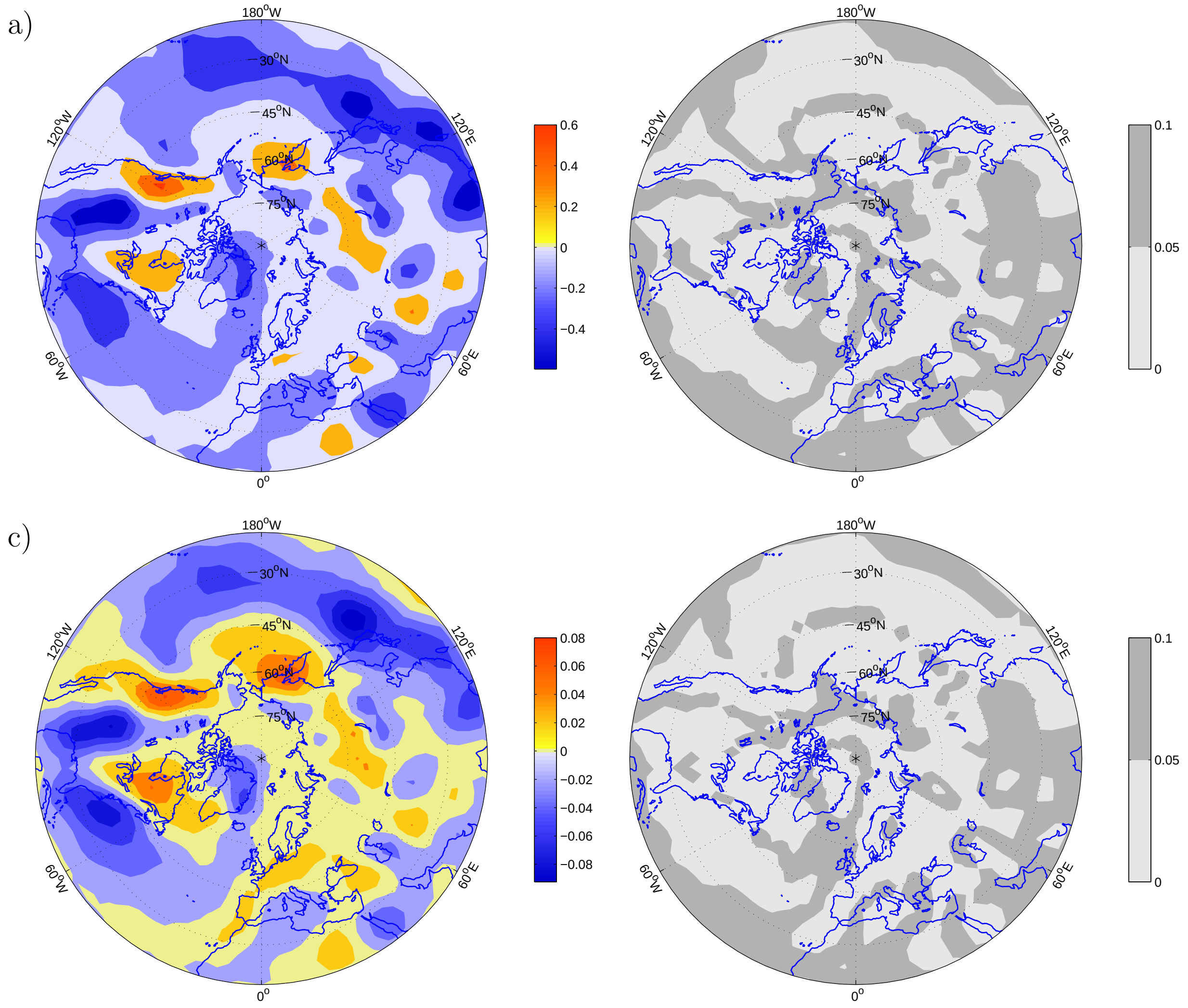

Figure 5.9: *The difference between the JJA and DJF seasons for the Northern Hemisphere from 1949 to 2002: (a) The mean growth/decay rate; and (b) The tendency. The right-hand side is a t-test of the difference between summer and winter showing areas where this difference is statistically significant at the 95% confidence interval.*

Chapter 6

Variability

The previous chapter dealt with general assertions related to the climatology of the different track variables for the Northern Hemisphere as a whole. The focus now is on more regional aspects of the variability of the track statistics both in the North Atlantic and the Arctic. The first part of this chapter will consider trends and cycles, in the number of storms and their intensity, for the five different regions studied. Later, it will also analyze the relation between summer extra-tropical storms and the large-scale flow.

Appendixes C, E and F will be used throughout this chapter. Appendix C discusses the differences between the parameters used for choosing the 'best' regression model: AIC and R^2. Appendix E, however, displays plots of the contribution of each teleconnection pattern used in the regression equations. Finally, Appendix F shows all of the fitted models (candidate models) which fulfilled the criteria discussed in section 6.3.

6.1 Is the Number of Storms Changing?

In order to answer the question above, it is necessary to analyze cycles and trends in the track density variable. Cycles were checked by computing the autocorrelation function[1], ACF, of the timeseries; the trend line was obtained by regressing the track density (the dependent variable) on the year (the explanatory one), that is, making up a linear trend.

Figure 6.1 shows the timeseries of the track density for regions: A, B, C, D and E; and their respective autocorrelation functions.

---

[1] The autocorrelation function (ACF) represents how a particular instantaneous amplitude value depends on previous occurrences of the amplitude values. It is defined as $\psi(\tau) = \lim_{T\to\infty} \frac{1}{T} \int_0^T f(t) \cdot f(t+\tau) dt$, where $\psi(\tau)$ is the autocorrelation function, f(t) is the magnitude of a characteristic property at an arbitrary instant (t), and $f(t+\tau)$ represents the magnitude of the same property at a time (τ) later (Broch 1981; Chatfield 2004; Maindonald and Braun 2005).

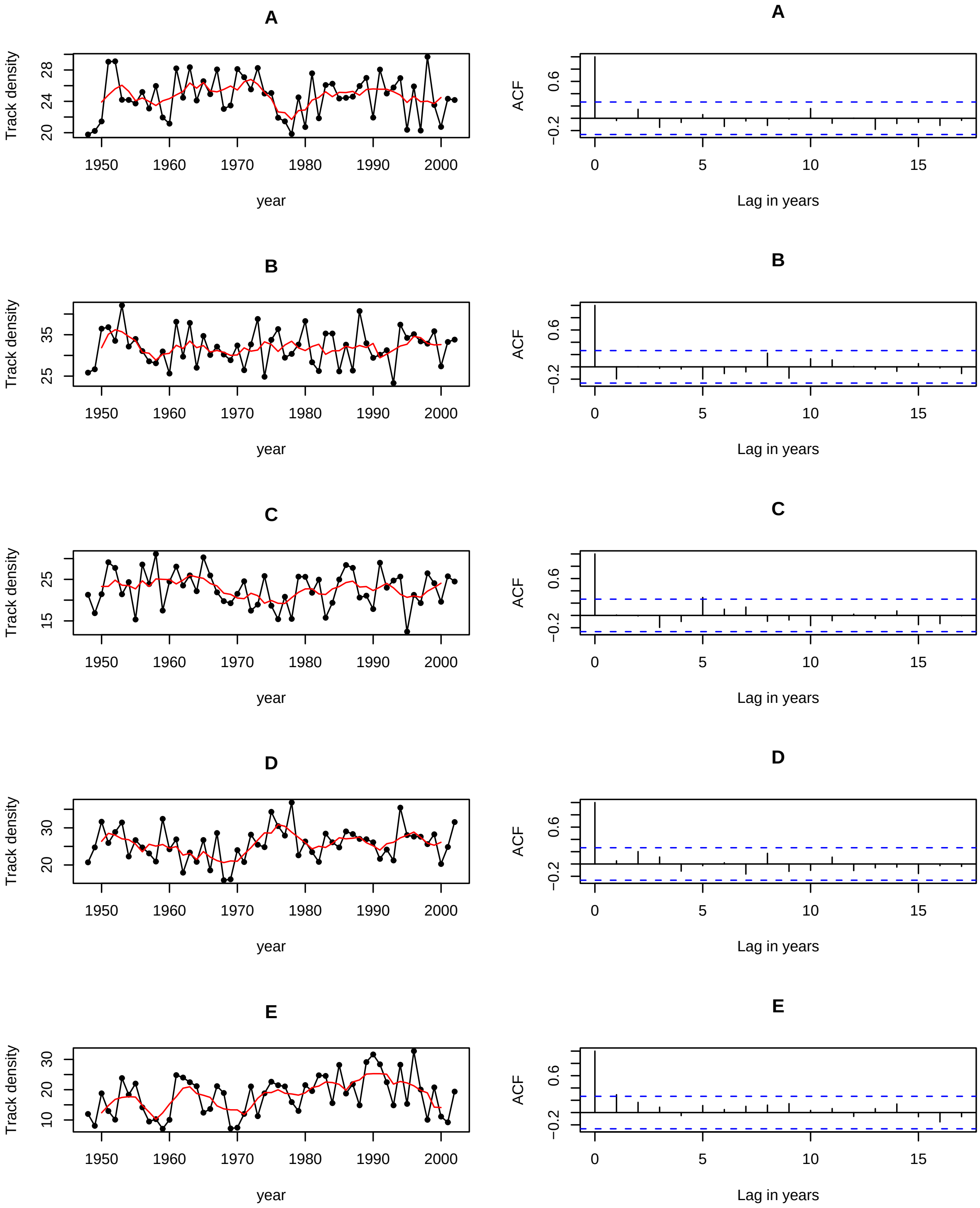

Figure 6.1: Left hand side: the track density for regions A, B, C, D and E. A 5-year-running mean is plotted in red. Right hand side: the autocorrelation function of the residuals, the lines above and below the ACF depict upper and lower 95% confidence limits.

The five-year running mean line in the plots seem not to represent an overall large increase or decrease in the number of storms through the decades for most of the regions. Apparently, there seems to be no trend in the number of storms either:

(i) **Region A**: there is a small increase from 1960 to 1970, followed by an abrupt drop during the 1970s. A sharp increase after 1980 is also seen and then, a more constant phase in the number of storms;

(ii) **Region B**: the number of storms in this region is more constant through the decades, except during the 1950s where there was a considerable drop;

(iii) **Region C**: this region experienced a decrease from mid-1960s to mid-1970s followed by an increase in the track density;

(iv) **Region D**: there is a decrease from around 1950 to 1970, an increase in the 1970s and a more constant number of storms from the 1980s on;

(v) **Region E**: this region is a bit different from the others, there is an increase in the number of storms, especially from 1980 to the 1990s and there seems to be an overall positive trend.

Cycles in the timeseries were identified through the autocorrelation function plots in figure 6.1 (right-hand side). The spikes in the plot which cross the confidence interval line are statistically significant. Therefore, there seems to be a 5-year and a 1-year cycle (at the 95% confidence interval) in regions C and E, respectively.

The track density was then regressed on time for each of the regions in order to search for a trend. A regression line was obtained and the autocorrelation of the residuals of the least square fit of the regression line were also plotted. The ACF plot of the residuals is important because the lack of correlation between them indicate the goodness of fit of the linear regression (Chatfield 2004; Maindonald and Braun 2005), that is, if no spikes cross the 95% confidence intervals in the ACF plot, then there is no correlation between the residuals.

Figure 6.2 (left-hand side) shows the track density timeseries with the regression line. The number in red represents the p-values of a t-test statistic to check whether the regression line is statistically significant or not. P-values under 0.05 are considered significant at the 95% confidence interval. There is no statistically significant trend at this interval, except in region E, where the trend (slope) is statistically significant $p - value = 0.017$, confirmed by the lack of correlation in the residuals (Figure 6.2 right-hand side) with a trend of 1.33 storms per decade (an increase of 38.88% of the average in 54 years).

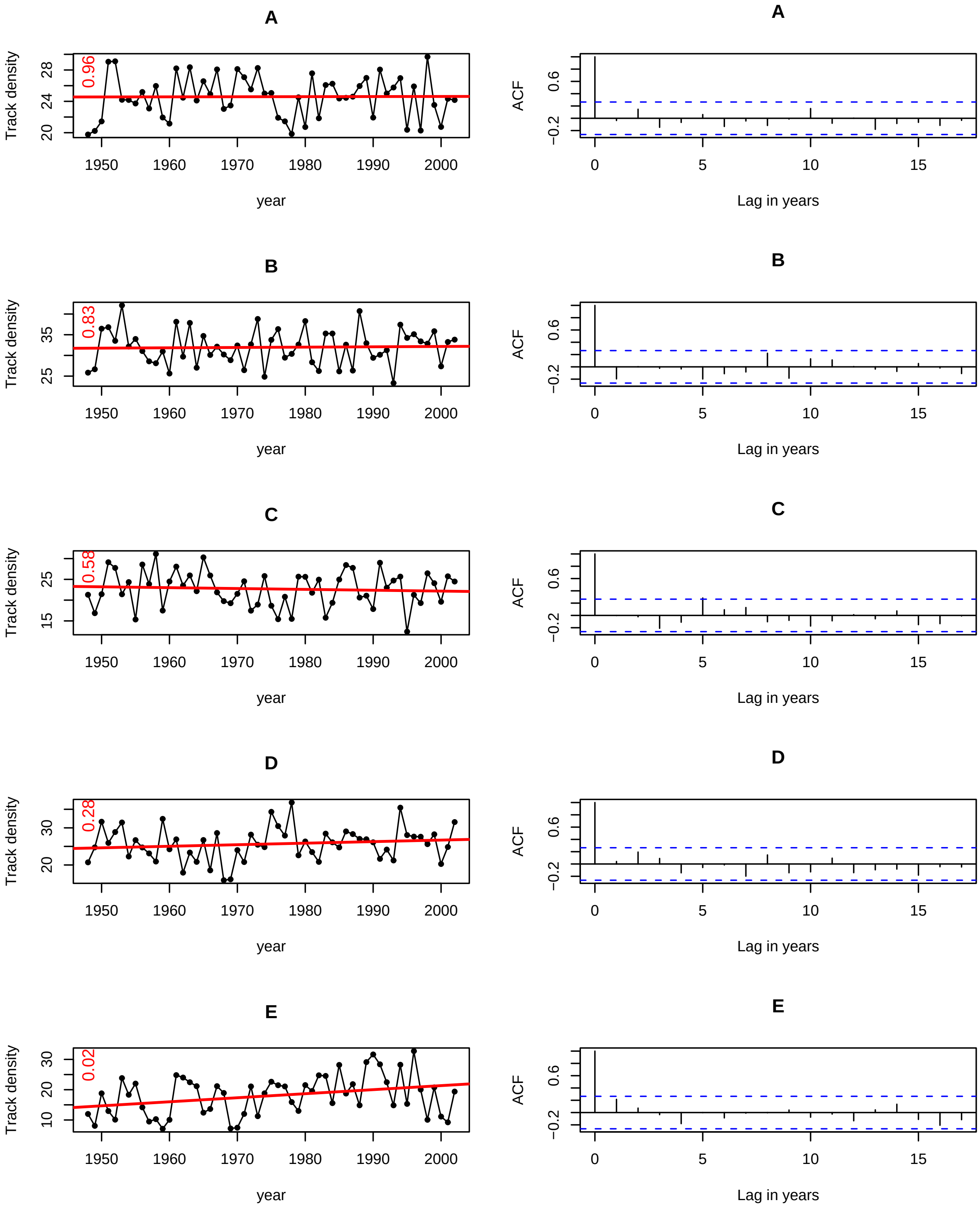

Figure 6.2: Left hand side: The timeseries of the track density for regions A to E; the red line shows a linear least squares fit for the data, that is, a trend line; The number in red is the p-value of the linear least squares fit, values under 0.05 are statistically significant at the the 5% significance level. Right hand side: The autocorrelation function of the residuals of the least squares fit, the lines above and below the ACF depict upper and lower 95% confidence limits.

6.2 Are the Storms Intensifying?

The variable analyzed here is the track intensity of the summer storms. A linear regression line was fit to each of the regions in order to find out if there was a trend. Figure 6.3 shows the timeseries of the intensity of the storm tracks for regions A, B, C, D and E (left-hand side).

The autocorrelation plots in figure 6.3 (right-hand side) help determine any cycles in the timeseries. There is no statistically significant cycle in regions A, C and E. However, region B presents a 4-year cycle, and region D a yearly and a two-year cycles, which are statistically significant at the 95% confidence interval.

Figure 6.4 (left-hand side) displays the linear regression line of the different timeseries. On the right-hand side, there is a plot of the autocorrelation function of the fit residuals: a lack of correlation between them means that the fit was effective. A liner trend was not found in region A: it is not statistically significant (p-value= 0.49). Region B shows a trend of $0.06x10^{-5}s^{-1}$ per decade, where the trend (slope) is statistically significant ($p - value < 0.001$) at the 5% significance level, confirmed by the lack of correlation in the residuals (Figure 6.4 right-hand side).

Region C has a statistically significant trend ($p - value = 0.05$) at the 95% confidence interval, with a negative trend of $-0.05x10^{-5}s^{-1}$ per decade. This is also confirmed by the lack of correlation between the residuals (Figure 6.4 right-hand side). There is a positive trend in region D: $0.06x10^{-5}s^{-1}$ per decade. This trend is also statistically significant at the 95% confidence interval ($p - value < 0.001$). There is a statistically significant trend ($p - value = 0.02$, 5% level) in region E. The trend is on the order of $0.09x10^{-5}s^{-1}$ per decade.

Table 6.1 summarizes the results:

Table 6.1: Summary of the Intensity Variable Within the Different Regions.

Region	**Cycle (year)**	**Trend ($x10^{-5}s^{-}1$ per decade)**
A	-	-
B	4	0.06
C	-	-0.05
D	1 and 2	0.06
E	-	0.09

(i) The trend results are statistically significant at the 95% confidence interval;

(ii) Cycle: The ACF function (Figure 6.3) was applied to the track intensity timeseries in order to look for cycles;

(iii) Trend: The ACF function (Figure 6.4, right-hand side) was applied to the residuals of the least square linear fit. The lack of correlation between the residuals of the trend line indicate the goodness of fit of the linear regression (Chatfield 2004; Maindonald and Braun 2005).

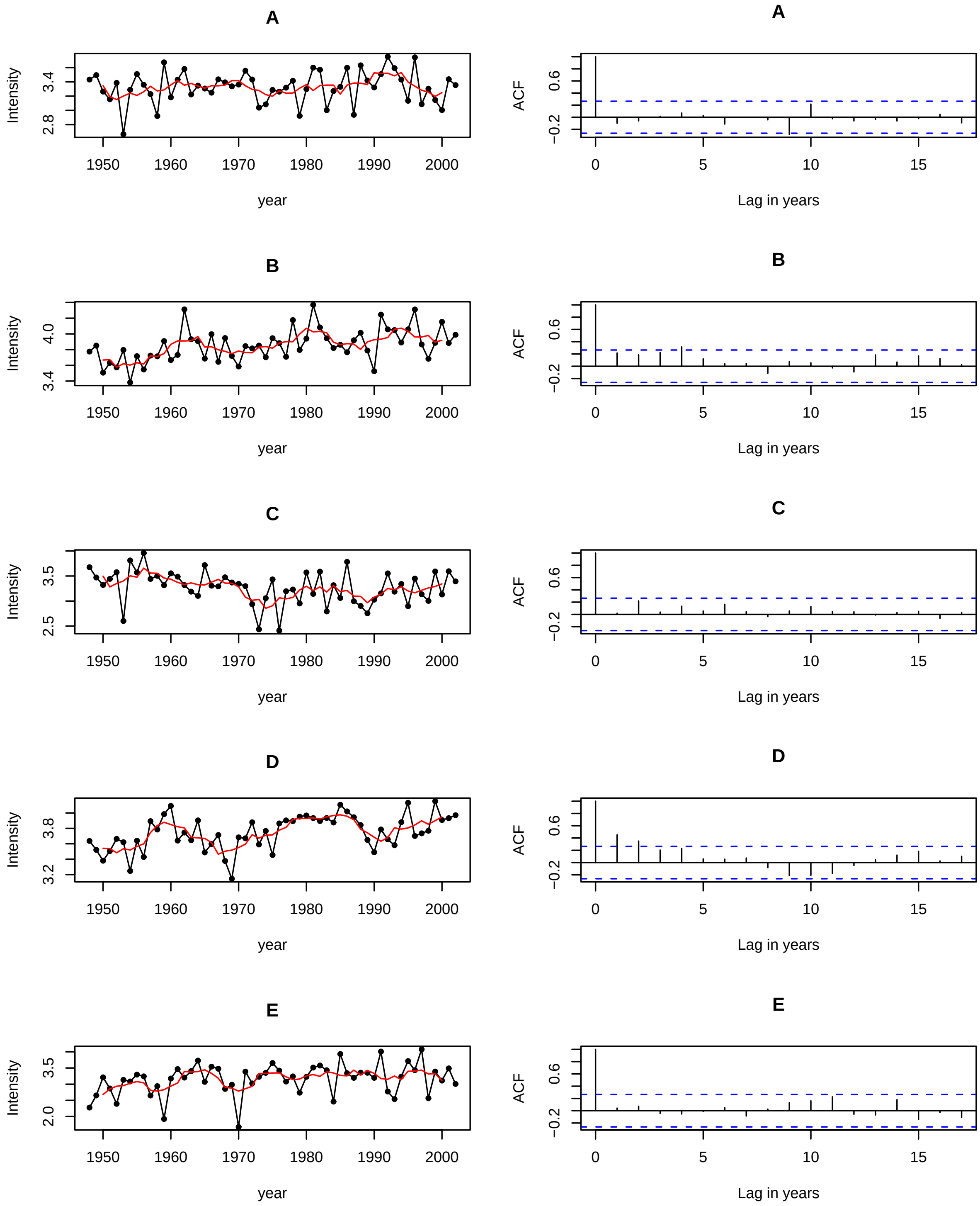

Figure 6.3: Left hand-side: The track intensity timeseries for regions A, B, C, D and E. A 5-year-running mean is plotted in red; Right hand side: The autocorrelation function of the track intensity, the lines above and below the ACF depict upper and lower 95% confidence limits.

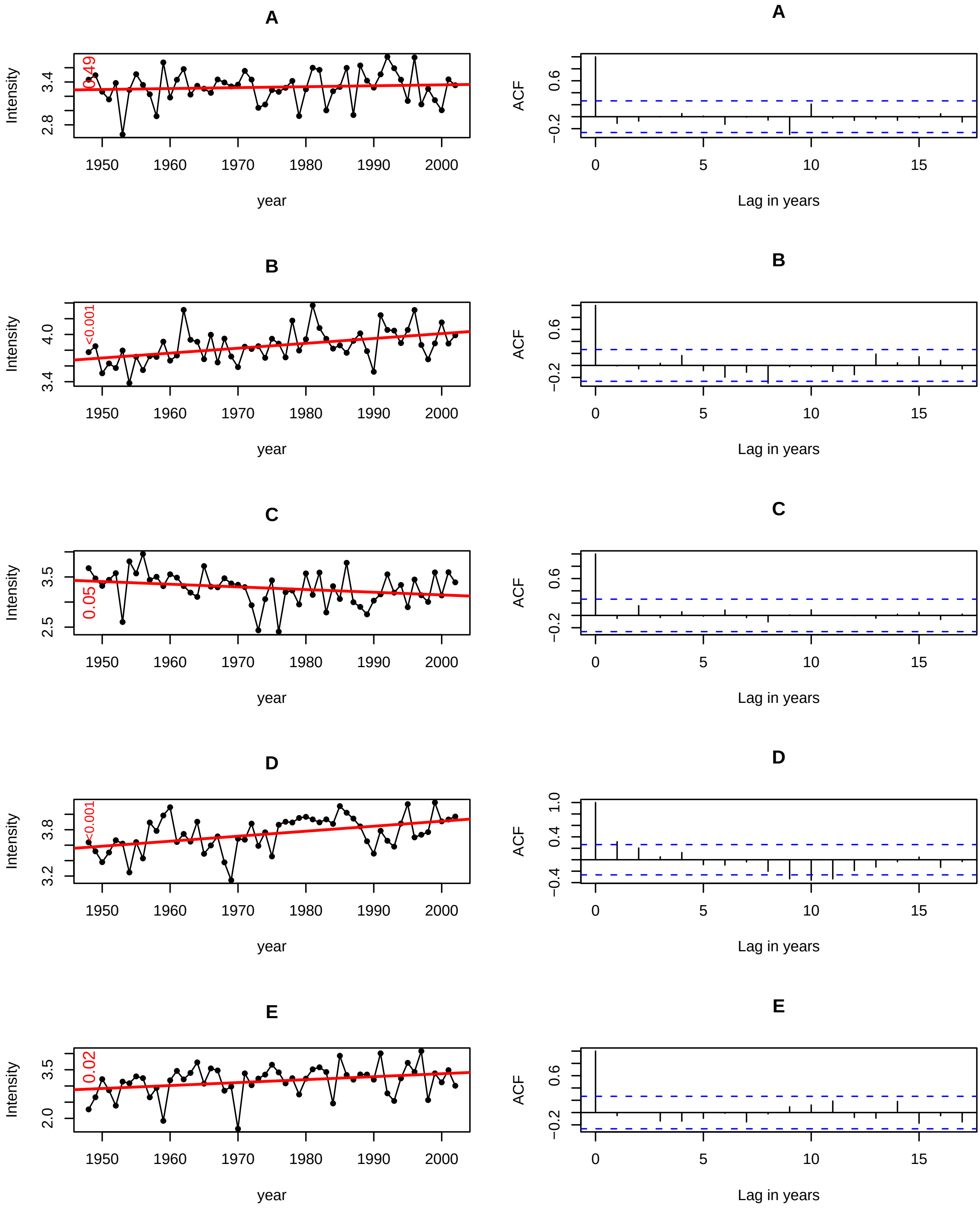

Figure 6.4: Left hand-side: The timeseries of the track intensity for regions A, B, C, D and E. The red line shows a linear least squares fit for the data, that is, a trend line: the p-values of the fit are written in red. Left hand-side: the autocorrelation function of the residuals of the least squares fit for the different regions, the lines above and below the ACF depict upper and lower 95% confidence limits.

6.3 Statistical Modeling of Selected Variables

A simple regression model[2] of the track density anomaly and track intensity has been applied to the different large-scale flow modes (which are relevant for the summer season in the NH, see subsection 6.3.1). The models for the five regions try to explain which and how much of these large-scale patterns and the AMO index (The Atlantic Multidecadal Oscillation) (Sutton and Hodson 2005) influence the variability of track density anomaly and intensity of summer storms. These indices were used as explanatory variables and different combinations of them were tried in order to find the most appropriate model that would be statistically significant at the 95% confidence interval. The different models whose combination between the different variables (indices) showed some skill[3] in explaining storm track variability of the equation and where the p-values were statistically significant are shown in Appendix F. The ones which are presented here were selected based on the lowest AIC[4] number.

The selection of the different combinations between the teleconnection patterns (and the AMO index) in explaining density anomalies was based following these steps:

(i) Different combinations were made to try to find the ones which were statistically significant at the 95% confidence interval (p-values less than 0.05). The combinations were, for example: model = Intercept + NAO, model = Intercept + PT, model = Intercept + AMO and so on. Since there are 7 indexes and a trend to be tried out, there were 8 possible combinations/equations to be tested for significance in this case;

(ii) Trials with more than one index were also tested, for instance: model = Intercept + NAO + PT, model = Intercept + NAO + AMO and so on. There were 28 possibilities[5] for this kind of combination;

(iii) After that, in order to reduce the number of trials for tests with three or four elements, which would generate 56 and 70 combinations[6], respectively, a scatterplot[7] (not shown) of all the explanatory variables, including the dependent variable, was used. This type of technique (Maindonald and Braun 2005) plots

---

[2] The regression models applied here are Multiple Linear Regression and it was assumed that the data were normally distributed. A test for normality was done and it is discussed in Appendix B.

[3] The AIC was thus used in this study as a parameter indicating improvement of the model skill. Even though the R^2 is commonly used for assessing a model qualitatively, it gives only a "rough sense of the adequacy of the model" and the information measure statistics (AIC) is a preferable measure for comparing different models (Maindonald and Braun 2005). See Appendix C for more information.

[4] Akaike's Information Criterion. See Appendix C for more information.

[5] $\binom{8}{2} = \frac{8!}{2!(8-2)!} = 28$.

[6] $\binom{8}{3} = \frac{8!}{3!(8-3)!} = 56$ and $\binom{8}{4} = \frac{8!}{4!(8-4)!} = 70$.

[7] See Maindonald and Braun (2005), pages 145-152, for more information on strategies for fitting multiple regression models.

each variable against one another and against the dependent variable. This was done to look for the different relationships between them to select which of the teleconnection patterns were most correlated to the explanatory variable. This method helped lowering the number of trials (combinations). Besides that, when the addition of more elements would not improve the skill or the statistical significance of the equations, the inclusion of more elements would not be used;

(iv) Then, all of the equations which were statistically significant were tested without an intercept element as well, in order to find out whether removing the intercept would improve the skill of the regression model or not;

(v) Finally, the combinations which were statistically significant were grouped together[8] and the 'best' model was selected according to its lowest AIC number.

6.3.1 Pattern Characteristics

Here, a simple description of the patterns which are relevant to the analysis in the next section are described. The descriptions shown below are only used as a guidance. They are not intended to provide a thorough explanation of each of the patterns, but to give a general idea of their behavior and importance for the summer season.

NAO - North Atlantic Oscillation

The NAO index can be defined as the difference between the normalized MSLP anomaly for Ponta Delgada (Azores) and for Akureyri (Iceland) (Barry and Carleton 2001). The NAO is strongest in winter and weakest in autumn, but it is "evident each month of the year" (Barry and Carleton 2001). The NAO index may influence not only the North Atlantic, but also parts of North America: according to Barnston and Livezey (1987), the NAO is characterized by a center west of Greenland, and a center of opposite sign over the Atlantic, Europe or the USA. During summer, "the Greenland center is near $70° - 75°N$ with zero line $50° - 60°N$, the Atlantic center is as far north as $40° - 50°N$, and a southern zero line near $30° - 35°N$." Figures 6.5 and 6.6 show the summer NAO mode and timeseries, respectively.

Both phases of the NAO are associated with changes in the intensity and location of the North Atlantic jet stream and storm track, and in large-scale modulations of the normal patterns of zonal and meridional heat and moisture transport (Hurrell 1995).

EA-JET - East Atlantic Jet

The East Atlantic Jet is characterized by a north-south dipole of pressure anomalies positioned in the eastern North Atlantic and Scandinavia, and another center located

---

[8] See Appendix F.

in Northern Africa and the Mediterranean Sea. This pattern appears between April and August (Rogers 1990).

According to Rogers (1990), a positive phase of the EA-JET represents an intensification of westerlies over central latitudes of the eastern North Atlantic and over Europe. A negative phase, however, is related to long-living blocking systems in Greenland and Great Britain.

Besides that, Washington et al. (2000) comments on the contribution of the EA-JET pattern to the summer season: "Summer melt is associated with the East Atlantic Jet Pattern in the Boreal spring" related to the Svalbard glaciers. Figures 6.5 and 6.6 show the summer EA-JET mode and timeseries, respectively.

WP - West Pacific Pattern

The WP pattern is characterized by a north-south dipole of pressure anomalies centered over the Kamchatka peninsula and southeastern Asia (in summer and fall a third centre is added over the Beaufort sea).

This pattern can be defined[9] as the difference in the normalized 500 mb height anomalies between two points (60°N, 155°E and 30°N, 155°E) (Wallace and Gutzler 1981). A positive phase of this index represents an increase in precipitation in all seasons over high latitudes of the North Pacific. It also affects the position of storms: a northward shift. During summer and fall, the WP pattern becomes more wave-like, and a third center appear over Alaska and the Beaufort Sea. Another anomaly center is also located over the eastern North Pacific and southern US in all seasons. A negative phase is associated with a zonal Pacific jet. Figures 6.5 and 6.6 show the summer EA-JET mode and timeseries, respectively.

PT - Pacific Transition Pattern

The Pacific Transition is characterized as a wave-like pattern of anomalies which extends from the Gulf of Alaska to the Labrador Sea and is aligned along 40° N. It is also associated with above-average surface temperatures in the western subtropical North Pacific, the subtropical North Atlantic, and western North America, and with below-average temperatures over the eastern half of the United States. This pattern is also the leading mode during August and September (Hansen and Svenoe 2005).

The PT has a broad east-west band in the subtropical Pacific. Barnston and Livezey (1987) emphasize that a "center is found in the eastern Soviet Union... with a... center of opposite sign in southwest Canada which may also include the west of central United States and northern Canada or the Arctic." Thus, this is an index related to the Pacific, but it has consequences in the North Atlantic and the Arctic areas.

---

[9] Another definition is based on the Rotated PCA for the 700 hPa height field.

The positive phase of the PT pattern is characterized by above-average heights west of Hawaii and across western North America, and below-average heights in the Gulf of Alaska and over the southeastern United States. A negative phase, however, is linked to a reduced ridge over North America.

ASU - Asian Summer

The Asian Summer pattern is an important mode from June to August. The ASU has an east-west center in central Asia, besides that, "...loadings of opposite sign tend to reside to the north, including Novaya Zemlya and sometimes the pole" (Barnston and Livezey 1987). A positive phase of the pattern is indicated by above-normal heights throughout southern Asia and northeastern Africa. The Asian Summer pattern exhibits considerable interannual and interdecadal variability.

Gong and Ho (2003) found a relationship between the Arctic Oscillation and the the East Asian summer circulation features. A positive phase of the AO pattern[10] in late spring "is found to lead a northward shift in the summertime upper troposphere jet stream over East Asia." (Gong and Ho 2003) Thus, the AO pattern influences both the monsoon rainfall and the associated summer circulation features in Asia. Consequently, this will have a great impact over the ASU pattern.

---

[10] The AO pattern stands for the Arctic Oscillation. A positive phase of this pattern is characterized by below normal pressure over the pole and above normal pressure over the mid-latitudes, enhanced polar vortex and stronger westerlies (Thompson and Wallace 1998; Xie et al. 2005).

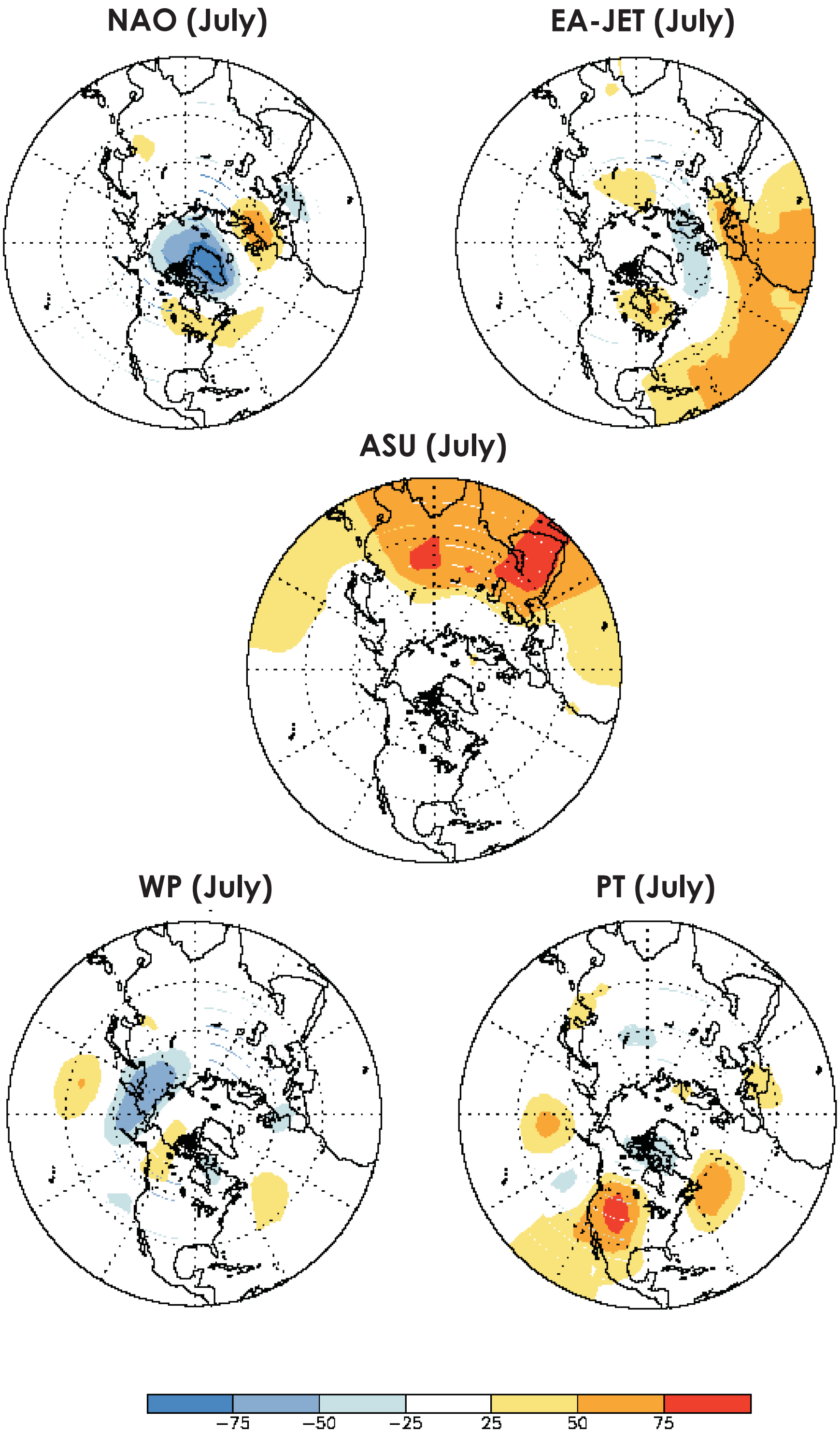

Figure 6.5: Positive phase of the patterns in the summer. The plotted values represent the temporal correlation between the standardized height anomaly and the teleconnection index. Reproduced from NOAA - Climate Prediction Center: *http : //www.cpc.ncep.noaa.gov/data/teledoc/teleintro.shtml*.

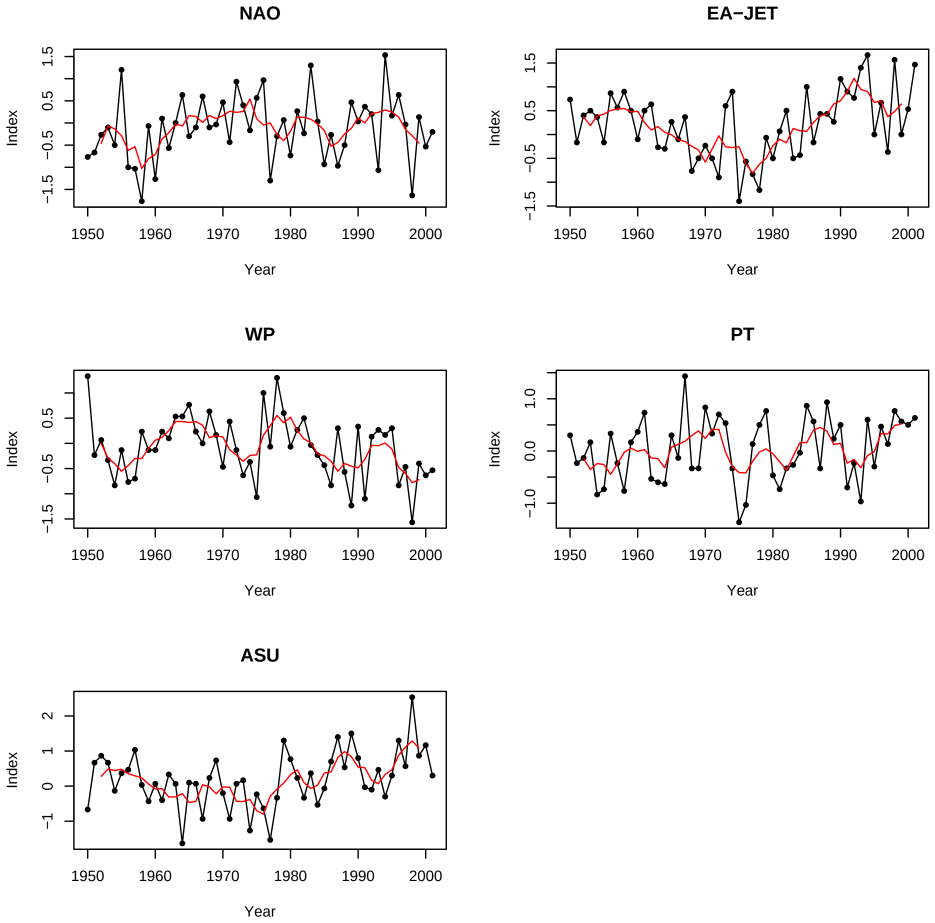

Figure 6.6: The timeseries of the summer (JJA) teleconnection patterns used in the statistical modeling. In red: a 5-year running mean average.

AMO - Atlantic Multidecadal Oscillation

The AMO index is a parameter related to the Sea Surface Temperature over the Atlantic ocean. It is thought to be driven by the ocean's Thermohaline Circulation (Sutton and Hodson 2005), and it shows the importance of convection during the summer season. It has been used for summer studies and it has proven to be a good predictor for rain in Europe and North America (Sutton and Hodson 2005):

> ...the AMO has indeed been responsible for marked changes in the regional atmospheric circulation, and for associated anomalies in precipitation and surface temperature over the US, southern Mexico and, probably, western Europe.

Sutton and Hodson (2005) also found that the Atlantic Ocean was the dominant influence for summer climate in the regions they studied. The changes in phase of the AMO affect the climate in Europe and the United States: “A change in phase of the AMO in the 1960s may have caused a cooling of U.S. and European Summer climate; a further change in the AMO may have contributed to recent warming in these regions” (Sutton and Hodson 2005). Figure 6.7 shows a smoothed timeseries of the AMO index and the spatial pattern of Sea Surface Temperature variations associated with the AMO index.

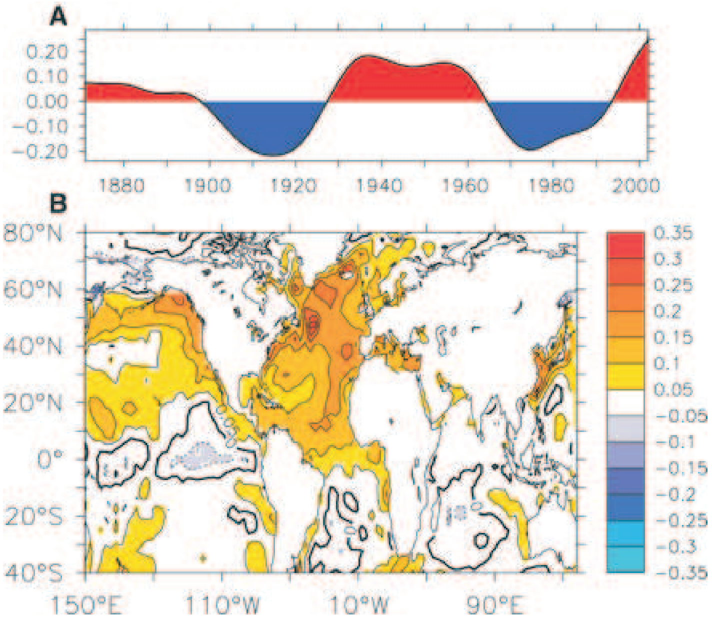

Figure 6.7: (A) The AMO index from 1871 to 2003, calculated by averaging annual mean SST observations over the region 0N to 60N, 75W to 7.5W. The units on the vertical axis are $^\circ C$. (B) The spatial pattern of SST variations associated with the AMO index. Reproduced from Sutton and Hodson (2005).

6.3.2 Selected Models

Here we present the results of the fitted models chosen to explain the relationship between the track density anomaly and intensity, with the large-scale flow for the regions studied. Appendix F brings all of the statistically significant candidate regression models used in this selection.

Track Density Anomaly - Region A

For region A, the variables which gave the best regression models with a high degree of skill were: EA-JET, NAO, WP and a linear trend (represented by the year variable). The best model was selected according to its AIC number[11]. The lower the AIC, the

---

[11] Appendix C discusses the main differences between the R^2 and the AIC (Akaike's Information Criterion). The AIC is used in the thesis because it is a better parameter for making comparison

better skill the model has. Table F.1 (Appendix F) shows the combinations that are statistically significant at the 95% confidence interval (p-values less than 0.05).

Thus, the fitted model chosen is the fifth in table F.1: a regression model of track density on NAO, $EA - JET$, WP and a linear trend, fitted by ordinary least squares:

$$\widehat{TD}_i = \beta_0 + \beta_1 p_{eajet_i} + \beta_2 p_{wp_i} + \beta_3 p_{nao_i} + \beta_4 year_i \tag{6.1}$$

where $\widehat{TD}_i$ is the track density fitted model. The parameter estimates are $\beta_0 = 102.36 \pm 45.69$, $\beta_1 = 1.16 \pm 0.51$, $\beta_2 = -1.39 \pm 0.56$, $\beta_3 = 1.05 \pm 0.48$ and $\beta_4 = -0.05 \pm 0.02$. The slope is significantly different from zero ($p - value = 0.007$) and the coefficient of determination, R^2, is 25.6%. Even though this coefficient explains only one fourth of the track density variance in region A, this regression equation was the most appropriate fit from the different large-scale factors which are important in summer.

Region A is located within the region of action of all of the patterns used in the fitted model 6.1. The correlation coefficient between the track density in region A and the NAO is 0.15, the EA-JET is 0.26 and the WP is -0.30. The correlation coefficients are not so high. However, it is their combination in the multiple linear regression equation which increases the skill and the significance of the fitted model. The patterns in equation 6.1 which contribute most to the fitted model are the NAO and the EA-JET, according to the plots presented in Appendix E.

The 5-year running mean average may be used as an aid to find similarities between the timeseries and the teleconnection patterns. By comparing the track density anomaly timeseries (Figure 6.8) with the timeseries of each of the patterns used in the fitted model (Figure 6.6), one can observe some common characteristics between them. For example, the 5-year running mean for the track density anomaly is quite similar to the NAO series, even though the correlation between their unfiltered series is not high. The WP pattern captures the features in the track density from around 1960 to 1980; and from 1980 to 2002, a more negative correlation between them is observed. As for the EA-JET, it seems to capture the features of the track density 5-year running mean from 1970 to around 1990.

The fitted model 6.1 seems to explain quite well the variability of the track density anomaly from around 1970 to 2002 (Figure 6.8 lower). The reason why the correspondence is not so accurate for the beginning of the series may be related to the fact that the coefficient of determination of the regression equation explains only 25.6% of the variability[12]. It is important to emphasize that what figure 6.8 (lower) displays is only an estimation. There are confidence intervals (95%) in which the values could vary (shown as dotted black lines).

---

between models and selecting the best one (Chatfield 2004; Maindonald and Braun 2005). The model with the smallest AIC value has the best skill.

[12] See Appendix E: the contribution of each variable used in the regression equations.

The same applies to the regressed series (Figures 6.9, 6.10, 6.11, 6.12, 6.13, 6.14, 6.15, 6.16 and 6.17) of the other regions for the track density anomaly and intensity. Even though the values of the regression series seem not to be exactly the same as the original timeseries, it is important to analyze the confidence intervals in which these values could vary in the 95 % confidence interval. Therefore, the regression plots display, as dotted black lines[13], the confidence interval limits for the track density anomaly and the track intensity, respectively.

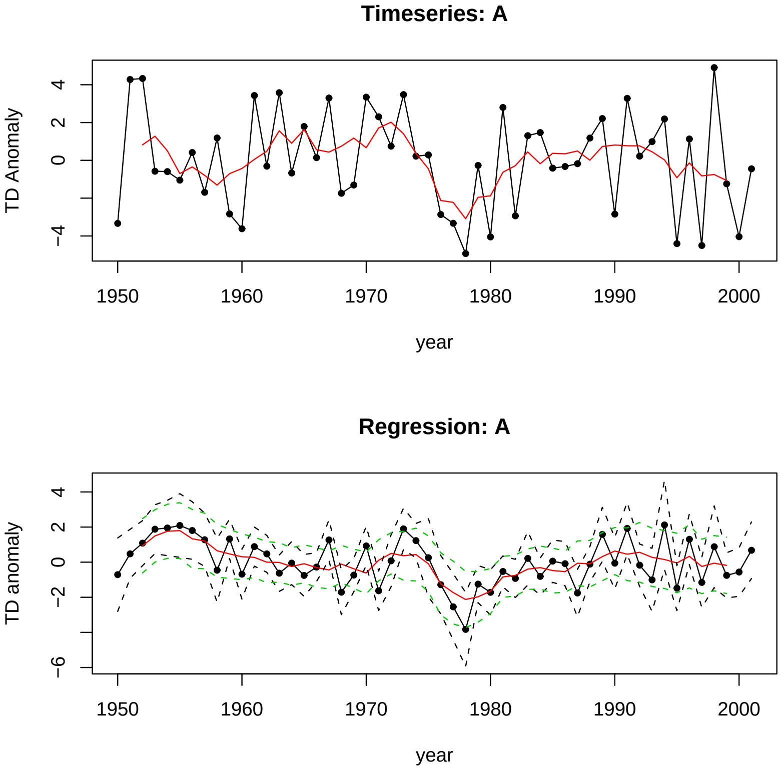

Figure 6.8: Upper: The original timeseries of the track density anomaly for region A. Lower: The regression timeseries of the track density anomaly using the fitted model 6.1. A 5-year-running mean is plotted in red. The dotted black lines are 95% pointwise confidence intervals for the fitted curves. The green lines are 95% pointwise confidence intervals for the 5-year-running mean.

Track Density Anomaly - Region B

The variables which gave the best results in the regression of the track density anomaly for region B were: NAO, AMO, ASU, WP and a linear trend (year). Table F.2 (Appendix F) shows the results for the combinations which are statistically significant at the 95% confidence interval (p-values less than 0.05).

---

[13] Green dotted lines are plotted for the 5-year running mean.

For the regression model of the track density for this region, the best fit chosen was based on the smallest AIC number. The model selected is the fourth equation in table F.2. This equation is made up of a combination between the NAO, the AMO and a linear trend. It is important to observe that this model does not contain an intercept:

$$\widehat{TD}_i = \beta_1 p_{amo_i} + \beta_2 p_{nao_i} + \beta_3 year_i \tag{6.2}$$

where $\widehat{TD}_i$ is the track density fitted model. The parameter estimates are: $\beta_1 = 6.58 \pm 2.23$, $\beta_2 = 2.86 \pm 0.77$ and $\beta_3 = -0.07 \pm 0.02$. The slope is significantly different from zero ($p - value = 0.002$) and the coefficient of determination is 26.3%. Again, this equation explains only around one fourth of the track density variance in region B. Figure 6.9 shows the timeseries of the track density anomaly for region B and the regression timeseries using equation 6.2.

The correlation coefficient between the track density anomaly in region B and the NAO is 0.36 and the AMO is 0.23. It seems that the NAO has a larger influence in the fitted model, as confirmed by the plots in Appendix E. Both the NAO and the AMO have centers of action within region B (compare Figures 4.3, 6.5 and 6.7). By comparing the 5-year running mean of the track density timeseries for region B (Figure 6.9) and the 5-year running mean of the patterns used in the equation (Figure 6.6), one sees that the NAO seems to be similar to the track density series from around 1950 to 1964 and from 1990 to 2002. The AMO has a similar negative drop in the 5-year running mean from 1950 to around 1970 and an increase afterwards.

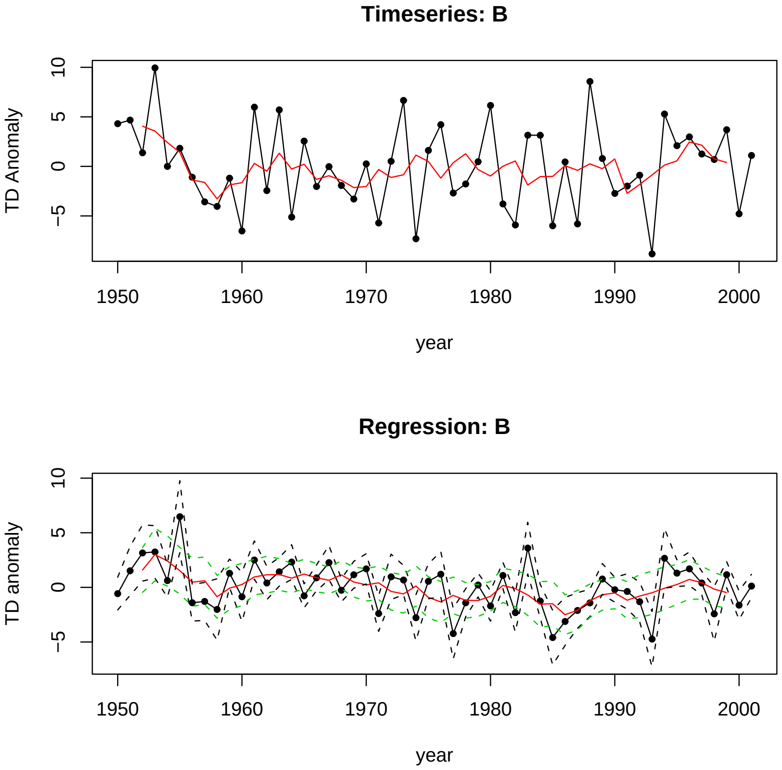

Figure 6.9: Upper: The original timeseries of the track density anomaly for region B. Lower: The regression timeseries of the track density anomaly using the fitted model 6.2. A 5-year-running mean is plotted in red. The dotted black lines are 95% pointwise confidence intervals for the fitted curves. The green lines are 95% pointwise confidence intervals for the 5-year-running mean.

Track Density Anomaly - Region C

From the different combinations with the relevant indices for summer, 8 equations were mostly significant, as shown in Table F.3 (Appendix F).

For region C, the best fit obtained was a combination between the NAO, the EA-JET and a linear trend. This model has the lowest AIC value ($AIC = 135.72$) among the others. The simple regression model obtained was:

$$\widehat{TD}_i = \beta_0 + \beta_1 p_{nao_i} + \beta_2 p_{eajet_i} + \beta_3 year_i \qquad (6.3)$$

where $\widehat{TD}_i$ is the track density fitted model. The parameter estimates are $\beta_0 = 102.71 \pm 67.71$, $\beta_1 = -2.19 \pm 0.73$, $\beta_2 = 2.36 \pm 0.76$ and $\beta_3 = -0.05 \pm 0.03$. The regression equation is statistically significant ($p - value < 0.001$). This model explains 36.7% of the track density variance in region C.

The correlation coefficient between the track density anomaly in this region and the NAO is -0.48 and the EA-JET is 0.43. These are high values of correlation. Both indexes seem to have an important influence in the fitted model (See Appendix E). Region C is also located within regions of action of both the NAO and the EA-JET.

Similar features between the 5-year running mean of the track density anomaly (Figure 6.10) and the patterns (Figure 6.6) were: for the NAO, there seems to be a similar drop from the 1950s to mid-1950s, then a more curved shape from mid-1950s to 1970, and a short drop from 1970 to 1980; The EA-JET pattern has a two-sided pattern, that is, a decay from 1950 to mid-1970s and an increase afterwards. This is a similar feature to the 5-year running mean of the track density as well.

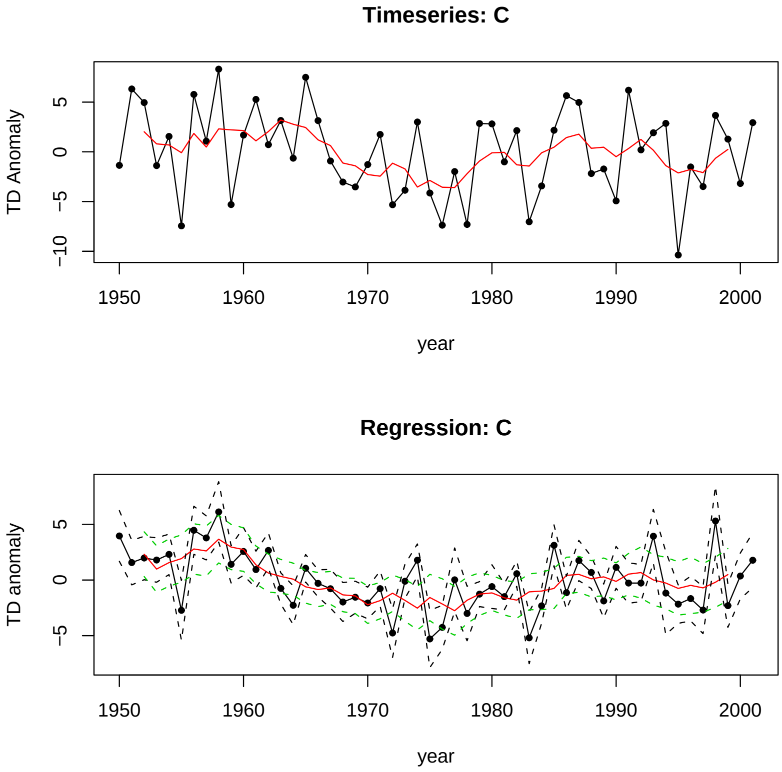

Figure 6.10: Upper: The original timeseries of the track density anomaly for region C. Lower: The regression timeseries of the track density anomaly using the fitted model 6.3. A 5-year-running mean is plotted in red. The dotted black lines are 95% pointwise confidence intervals for the fitted curves. The green lines are 95% pointwise confidence intervals for the 5-year-running mean.

Track Density Anomaly - Region D

For region D, 4 equations (Table F.4, Appendix F) were significant. Most of them used the NAO or the PT indices. The fitted model chosen was number 4:

$$\widehat{TD}_i = \beta_1 p_{nao_i} + \beta_2 p_{pt_i} \tag{6.4}$$

The parameter estimates are: $\beta_1 = 1.73 \pm 0.81$ and $\beta_2 = 1.76 \pm 0.97$. The regression equation is statistically significant ($p - value = 0.03$). This model explains 13.3% of the track density variance in region D.

The correlation coefficient between the track density anomaly in this region and the NAO is 0.28 and the PT is 0.23. Both the NAO and the PT patterns have a strong influence in this area (See Appendix E). This region is also within the center of action of the NAO and the PT patterns. The 5-year running mean of the track density timeseries (Figure 6.11) and the NAO (Figure 6.6) present similar features such as a drop from 1950 to 1960 and an increase after 1970, a curved shape from 1980 to 1990, and from 1990 to 2002. The PT index also presents some similarities: a drop until around 1960, another drop from mid-1970s to 1980 and a curved shape in the 1980s.

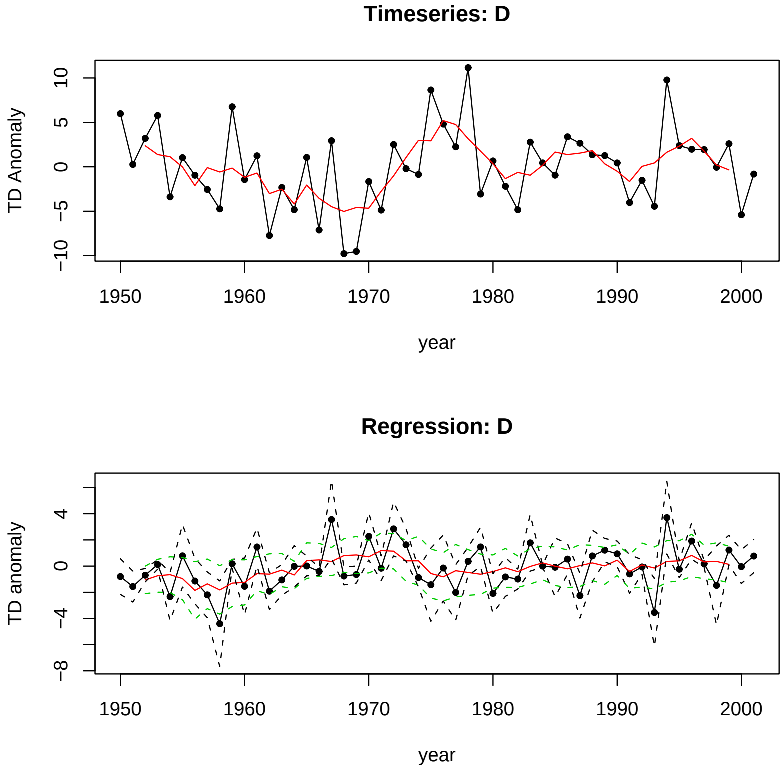

Figure 6.11: Upper: The original timeseries of the track density anomaly for region D. Lower: The regression timeseries of the track density anomaly using the fitted model 6.4. A 5-year-running mean is plotted in red. The dotted black lines are 95% pointwise confidence intervals for the fitted curves. The green lines are 95% pointwise confidence intervals for the 5-year-running mean.

Track Density Anomaly - Region E

As for region E, 7 equations were obtained (Table F.5,Appendix F). Again, the NAO was widely used among them. Besides that, the AMO gave a good result in equations 6 and 7. Equation 6 gave the highest R-squared.

However, model 3 was the one selected: its AIC was the lowest one, 188.05:

$$\widehat{TD}_i = \beta_1 p_{nao_i} \tag{6.5}$$

The parameter estimate is: $\beta_1 = 3.74 \pm 1.16$. The regression equation is statistically significant ($p-value = 0.002$). This model explains 16.9% of the track density variance in region E.

The correlation coefficient between the track density anomaly in this region and the NAO is 0.42. Region E is also within the center of action of the NAO pattern. Its influence over this area is really important. It contributed to a trend in the number of storms there: 1.33 storms per decade. The NAO (Figure 6.6) and the track density timeseries for region E (Figure 6.12) present many similarities: a drop until around 1958, an increase from 1958 to around 1963, then an increase from 1970 to around 1983 and finally, a drop from 1990 to 2002.

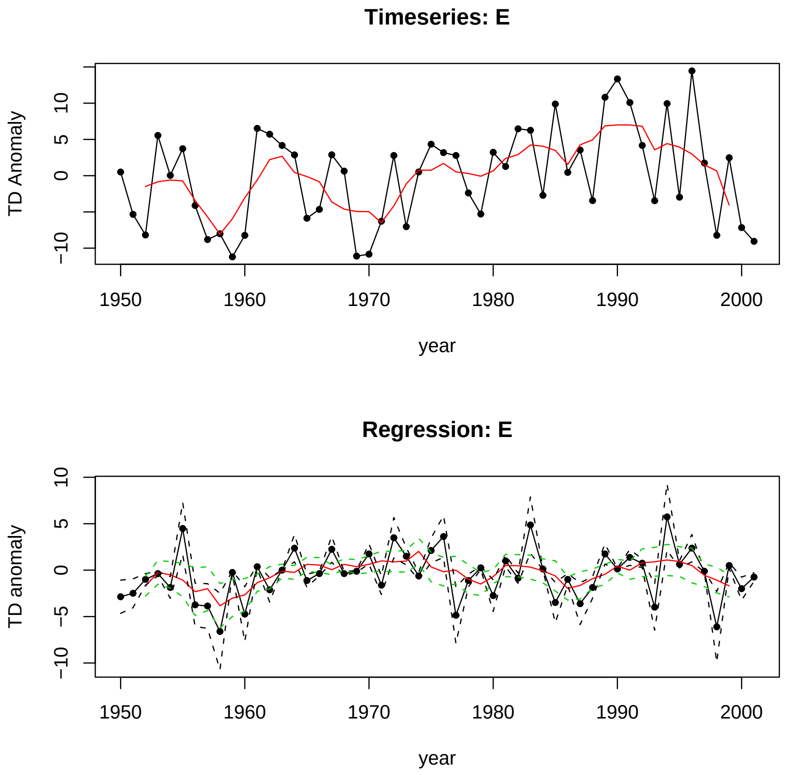

Figure 6.12: Upper: The original timeseries of the track density anomaly for region E. Lower: The regression timeseries of the track density anomaly using the fitted model 6.5. A 5-year-running mean is plotted in red. The dotted black lines are 95% pointwise confidence intervals for the fitted curves. The green lines are 95% pointwise confidence intervals for the 5-year-running mean.

Track Intensity - Region A

For the track intensity in region A, the best combinations used the AMO index. The fitted model chosen was number 3 (Table F.6, Appendix F): no intercept and the inclusion of a linear trend:

$$\widehat{TI}_i = \beta_1 p_{amo_i} + \beta_2 year_i \tag{6.6}$$

where $\widehat{TI}_i$ is the track intensity fitted model. The parameter estimates are $\beta_1 = -0.22 \pm 0.12$ and $\beta_2 = 0.004 \pm 0.001$. This model explains 99.6% ($p - value < 0.001$) of the track intensity variance in region A.

The correlation coefficient between the track intensity in this region and the AMO is -0.27. The AMO captures some of the track intensity features: a drop from around 1970 to 1975 and an overall increase afterwards. Region A is within the North Atlantic and it is thus influenced by the AMO index. This may indicate that the intensity of the storms for this area might be connected to the Sea Surface Temperature variation and to the diabatic heating.

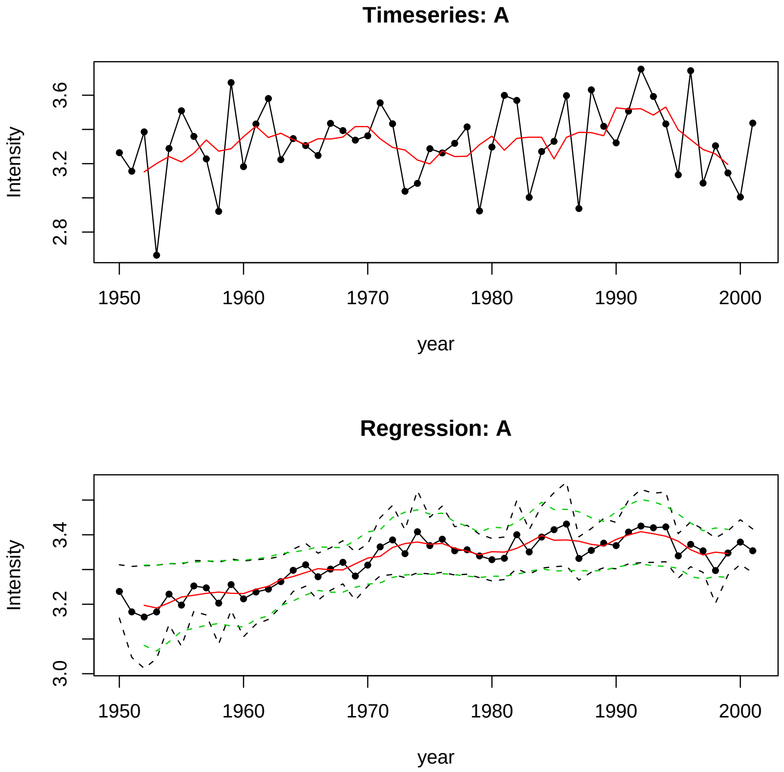

Figure 6.13: Upper: The original timeseries of the track intensity for region A. Lower: The regression timeseries of the track density anomaly using the fitted model 6.6. A 5-year-running mean is plotted in red. The dotted black lines are 95% pointwise confidence intervals for the fitted curves. The green lines are 95% pointwise confidence intervals for the 5-year-running mean.

Track Intensity - Region B

In region B, four possible candidate models used the WP and PT indices. The fitted model chosen was number 3 (Table F.7, Appendix F):

$$\widehat{TI}_i = \beta_0 + \beta_1 p_{pt_i} + \beta_2 year_i \tag{6.7}$$

where $\widehat{TI}_i$ is the track intensity fitted model. The parameter estimates are $\beta_0 = -11.59 \pm 3.30$, $\beta_1 = 0.008 \pm 0.002$, $\beta_2 = -0.12 \pm 0.04$. This model explains 34.35% of the track intensity variance in region B ($p - value < 0.001$).

The correlation coefficient between the track intensity for this region and the PT pattern is -0.22. The PT also influences this area where region B is located. The track intensity 5-year running mean timeseries (Figure 6.14) is similar to the PT pattern

(Figure 6.6) until around 1963, then there is another similar increase from 1975 to 1980, and a decrease from 1980 to around 1987.

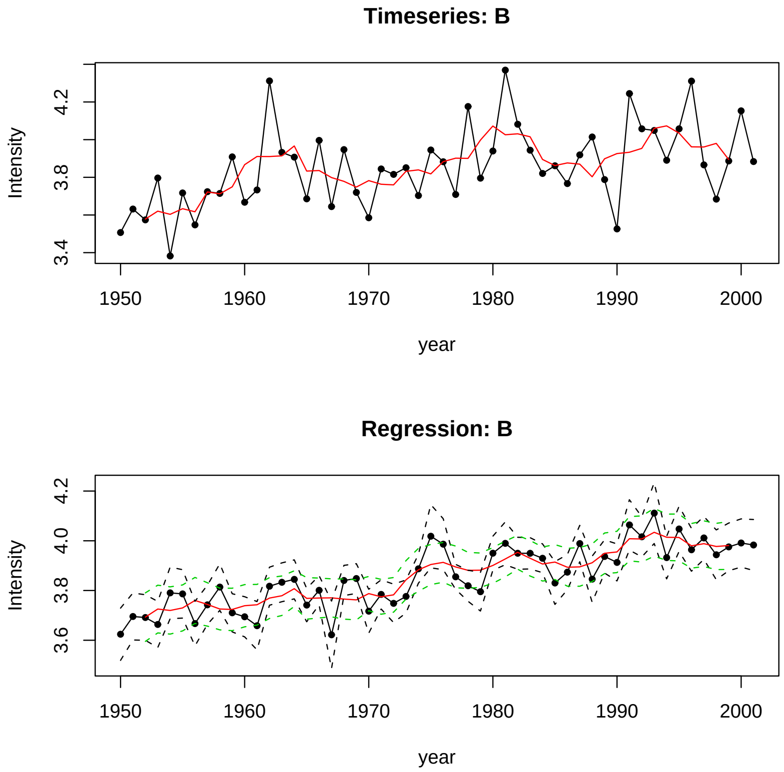

Figure 6.14: Upper: The original timeseries of the track intensity for region B. Lower: The regression timeseries of the track density anomaly using the fitted model 6.7. A 5-year-running mean is plotted in red. The dotted black lines are 95% pointwise confidence intervals for the fitted curves. The green lines are 95% pointwise confidence intervals for the 5-year-running mean.

Track Intensity - Region C

For region C, there are no models to be compared, only one seemed to fulfill the criteria (Table F.8, Appendix F):

$$\widehat{TI}_i = \beta_1 p_{nao_i} + \beta_2 year_i \tag{6.8}$$

where $\widehat{TI}_i$ is the track intensity fitted model. This model does not contain an intercept. The parameter estimates are $\beta_1 = -0.128 \pm 0.06$ and $\beta_2 = 0.0016 \pm 2.33x10^{-5}$. This model explains 99.04% ($p-value < 0.001$) of the track intensity variance in region C.

The correlation coefficient between the track intensity in this region and the NAO is -0.27. The track intensity over this area has decreased around -9.89% in 54 years. This area is located within the region of action of the NAO. The NAO pattern (Figure 6.6) and the track intensity (Figure 6.15) have some similar characteristics: an increase until around 1958, a decrease until 1963, a curved path from the end of the 1970s to the beginning of the 1990s, an increase from 1990 to around 1995 and a decrease afterwards.

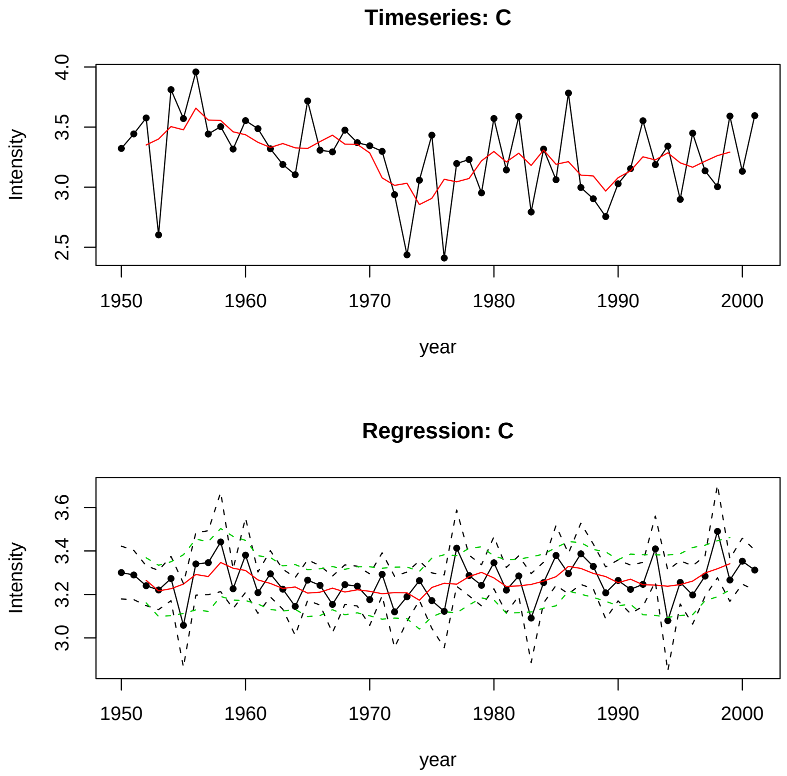

Figure 6.15: Upper: The original timeseries of the track intensity for region C. Lower: The regression timeseries of the track density anomaly using the fitted model 6.8. A 5-year-running mean is plotted in red. The dotted black lines are 95% pointwise confidence intervals for the fitted curves. The green lines are 95% pointwise confidence intervals for the 5-year-running mean.

Track Intensity - Region D

As for the intensity in region D, the tree best models used the indexes: AMO, EA-JET and the PT (Table F.9, Appendix F). Model 3 was the one selected:

$$\widehat{TI}_i = \beta_1 p_{pt_i} + \beta_2 year_i \tag{6.9}$$

where $\widehat{TI}_i$ is the track intensity fitted model. The parameter estimates are $\beta_1 = 0.07 \pm 0.05$ and $\beta_2 = 0.002 \pm 1.48x10^{-5}$. This model explains 99.7% of the track intensity variance in region D.

The correlation coefficient between the track intensity in this region and the PT pattern is 0.22. This index has a center of action over region D. The intensity in that area increased 8.64% in 54 years. The PT index (Figure 6.6) and the track intensity for region D (Figure 6.16) have some similarities: a decrease from 1960 to 1970; and an increase from around 1950 to 1960, another increase from 1970 to around 1980, and from 1990 to 2002.

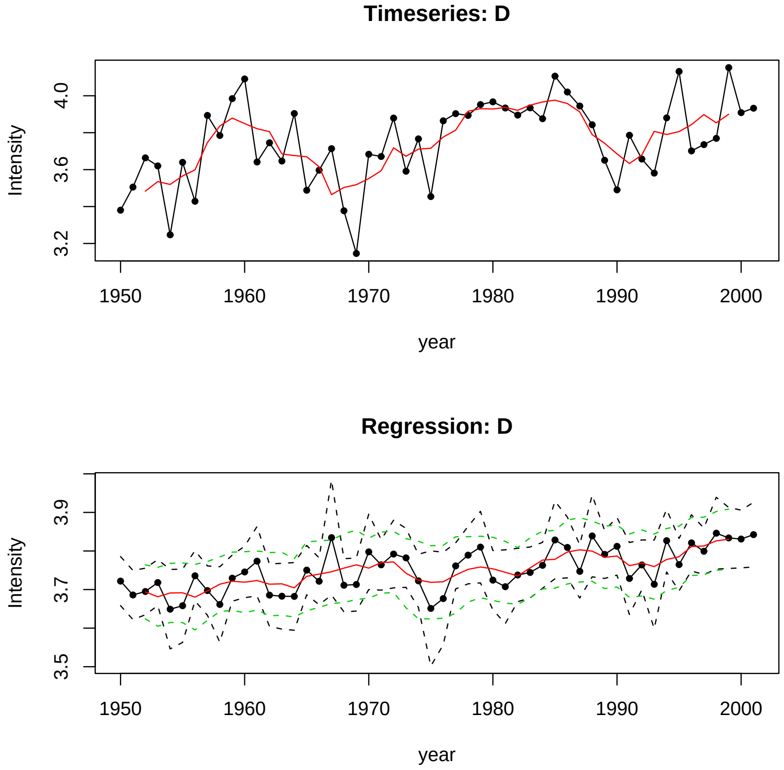

Figure 6.16: Upper: The original timeseries of the track intensity for region D. Lower: The regression timeseries of the track density anomaly using the fitted model 6.9. A 5-year-running mean is plotted in red. The dotted black lines are 95% pointwise confidence intervals for the fitted curves. The green lines are 95% pointwise confidence intervals for the 5-year-running mean.

Track Intensity - Region E

Finally, four fitted regression models were obtained for region E. These models used the AMO, EA-JET, ASU and the AMO. The model chosen was number 3 (Table F.10, Appendix F):

$$\widehat{TI}_i = \beta_0 + \beta_1 p_{asu_i} + \beta_2 year_i \tag{6.10}$$

where $\widehat{TI}_i$ is the track intensity fitted model. The parameter estimates are $\beta_0 = -17.39 \pm 8.37$, $\beta_1 = -0.16 \pm 0.08$ and $\beta_2 = 0.01 \pm 0.004$. This model explains 13.3% of the track intensity variance in region E.

The correlation coefficient between the track intensity in this region and the ASU is -0.16. The correlation is not high and region E is not located in the region of action of the ASU index. However, as it was shown before, the ASU pattern influences the pole as well (Barnston and Livezey 1987). Besides that, the AO[14] pattern in late spring may influence the ASU pattern mode in summer (Gong and Ho 2003). That is why the ASU gave good skill features to the fitted model for region E, which is located in the Arctic area and, as a consequence, it is influenced by the Arctic Oscillation. The ASU pattern (Figure 6.6) and the track intensity for region E (Figure 6.17) have some similarities: a decay in the 1950s, a semi-circle shape in the 1960s and another semi-circle shape in the 1990s.

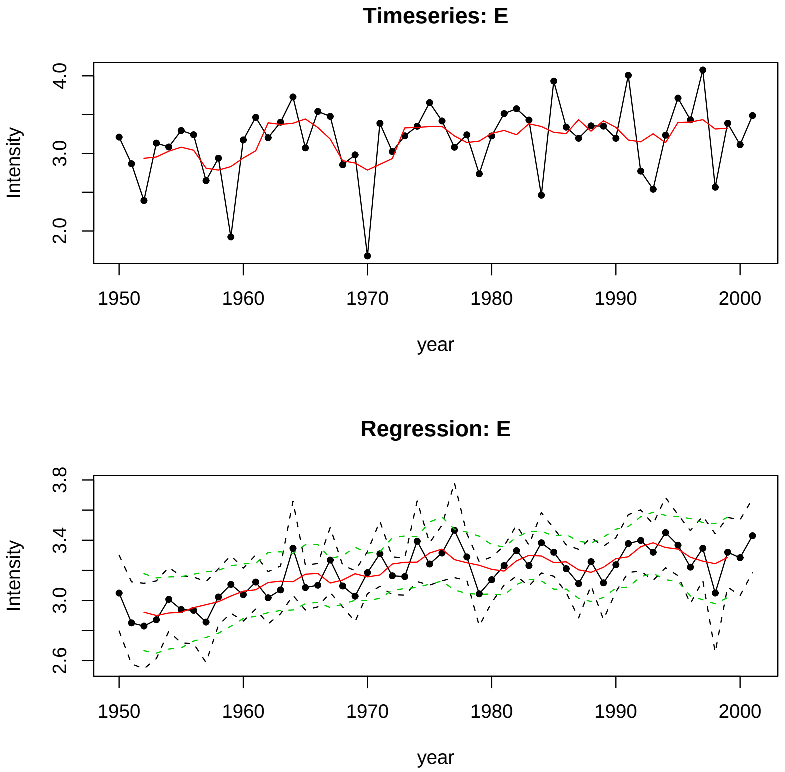

Figure 6.17: Upper: The original timeseries of the track intensity for region E. Lower: The regression timeseries of the track density anomaly using the fitted model 6.10. A 5-year-running mean is plotted in red. The dotted black lines are 95% pointwise confidence intervals for the fitted curves. The green lines are 95% pointwise confidence intervals for the 5-year-running mean.

---

[14] AO stands for the Arctic Oscillation.

Chapter 7

Discussion and Concluding Remarks

The discussion presented here will focus on the climatology results, the difference between summer and winter storm tracks, the variability and the relation to the large-scale flow. In summary, summer storms are weaker, more long-lived and shifted northwards compared to winter storms. The track density anomaly and the track intensity show a connection to the large-scale flow (teleconnection patterns related to the summer season) and to the sea-level temperature (given by the AMO index).

7.1 Climatology

The climatology results showed a similar structure to the winter storm tracks, that is, the maxima over the North Atlantic and the North Pacific. Most summer storms are generated downstream main orographic features. The Rocky Mountains and the Appalachian Mountains play the most important role in the generation of the storm tracks over the North Atlantic.

The path followed by summer storms in the North Atlantic are differently located compared to that during winter. The winter 'paths' are very widespread and may be found from latitude 40° upwards. We have also found that the storms are concentrated between Iceland and Greenland (Murray and Simmonds 1991; Jones and Simmonds 1993; Serreze et al. 1993; Barry and Carleton 2001; Serreze 1995). The summer storm paths, on the other hand, are found in a much narrower region. The tracks go from the east coast of the United States, cross the North Atlantic (generally between $50°-60°$N), and travel up on the eastern side of Iceland. This particular feature is interesting: there seems to be a preferred path for the winter storms, that is, between Iceland and the western part of Greenland, while the summer storms tend not to go there, they travel to the eastern side of Iceland and thus reaching Scandinavia and western Europe.

The mean lifetime of summer storms are mainly composed of storms which last from 5 to 7 days. Figure 7.1 shows the distribution of the mean lifetime of summer storms based on the climatology for the Northern Hemisphere. This amount of time is quite different from, for example, the mean lifetime of winter storms over the North Atlantic: from 4 to 5 days (Hoskins and Hodges 2002).

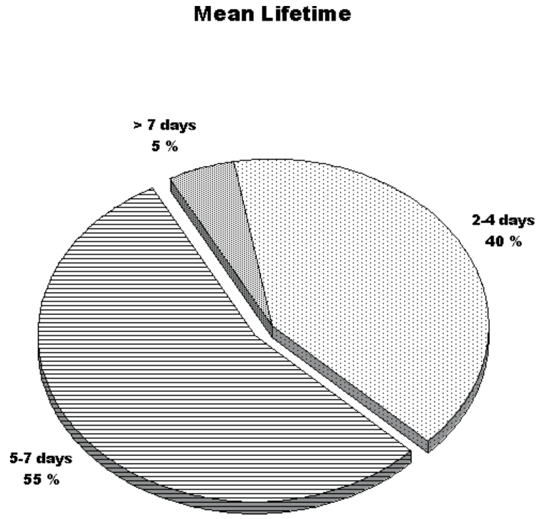

Figure 7.1: The distribution of the mean lifetime of the storm tracks in the Northern Hemisphere during summer. The modal mean lifetime is from 5-7 days.

The difference between summer and winter has shown that summer storms last longer, are weaker than winter ones. These storms are also shifted northwards as seen in the summer/winter difference in the track density and feature density variables, figures 5.6 a and b, respectively. The area between Greenland and Iceland seems to be preferred by winter storms. Figure 7.2 shows, as an example, the path of summer storms in 1954 for summer (a) and winter (b). Summer storms are not much found in the area between Greenland and Iceland, whereas winter storms are.

7.2 Variability

There is a positive trend in the number of summer storms in region E, in the Arctic. No statistically significant trends were observed in the North Atlantic regions studied. There seems to be a 5-year cycle in the number of storms in sector C (North Atlantic) and a 1-year cycle in sector E (Arctic).

In the North Atlantic, the summer storm intensity has increased about $0.06x10^{-5}s^{-1}$ per decade in region B. In region C, the intensity of the storms have decreased -0.05 $x10^{-5}s^{-1}$ per decade. In the Arctic, a positive trend of about $0.06x10^{-5}s^{-1}$ for sector

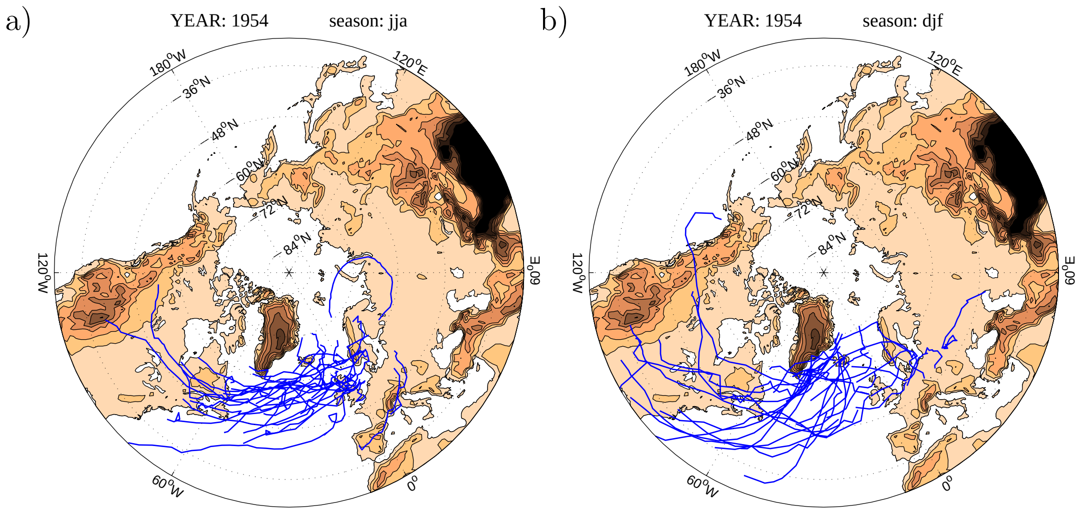

Figure 7.2: *The trajectories of the storms which ended within region A in 1954 for (a) Summer and (b) Winter.*

D in the track intensity and $0.09x10^{-5}s^{-1}$, in sector E . Table 7.1 summarizes the main trend findings.

Hence, summer storms in sector E in the Arctic are not only increasing their number but also intensifying. This is thus a very important region to be further investigated. Perhaps, the reason why this region is so important it is because of the decrease in sea-ice in that area (Overpeck et al. 2005), which may provide enough convective energy to the development and growth of the storms there, or by the large-scale flow, especially the summer NAO which helped explain the number of storm tracks in that sector and the Asian Summer (ASU) which was selected as a good explanatory variable for storm intensity in sector E. So, when the summer NAO index increases and the ASU index decreases, sector E may expect increase in the amount and intensity of summer storms.

Table 7.1: Summary of the Track Density and Intensity Trends Within the Different Regions.

Area	**Track Density Trend** (storms per decade)	**% of increase/decr.** of the average in 54 years	**Intensity Trend** ($x10^{-5}s^{-1}$ / decade)	**% of increase/decr.** of the average in 54 years
A	-	-	-	-
B	-	-	0.06	8.40%
C	-	-	-0.05	-9.89%
D	-	-	0.06	8.64%
E	1.33	38.88%	0.09	15.43%

7.3 Relation to the Large-Scale Flow

The summer storm tracks are related to the large-scale flow and to the Sea Surface Temperature. Table 7.2 summarizes the use of the different indices in the regression equations for the track density anomaly and the track intensity for the 5 sectors studied.

Table 7.2: Summary of the Teleconnection Patterns Used in the Regression Models.

	North Atlantic			**Arctic**	
	A	**B**	**C**	**D**	**E**
Track Density Anomaly	NAO (+∗) EA-JET (+∗) WP (−)	NAO (+∗) AMO (+)	NAO (−∗) EA-JET (+∗)	NAO (+∗) PT (+∗)	NAO (+∗)
Track Intensity	AMO (−∗)	PT (−∗)	NAO (−∗)	PT (+∗)	ASU (−∗)

(i) + : This sign represents that the explanatory variable is ascending: it contributes to increase the value of the regression equation;

(ii) − : The explanatory variable is decreasing: it contributes to a decrease in the value of the regression equation;

(iii) ∗ : This symbols is used to represent which explanatory variable makes a large contribution to the model.

NB: The symbols used here were based in the plots found in appendix E; The “year” variable (linear trend) was not included in this table, since the objective is to understand which *teleconnection patterns* were important in this study.

The summer NAO index is present in all of the regression equations for the track density anomaly case, not just for the North Atlantic sector but also for the Arctic too. The PT index used helps explain the variability in three of the regression models: The track density anomaly in region D and the track intensity in regions B and D. Region D is the most influenced by this parameter. For the track intensity in region E, the Asian Summer pattern (ASU) was the best index to help explain the variability in that sector. Even though it is a parameter for Asia, this index may affect the pole as well (Barnston and Livezey 1987).

Region A (Figure 4.3) was an important sector to be studied. It includes Iceland, Scandinavia, Great Britain and so on. No trends in the track density anomaly nor in the track intensity were found. However, the number of storms seem to have increased in that area (Figure 6.8) during the 1960s and 1980s. It has presented a decrease in the 1950s, 1970s and 1990s as well. Three teleconnection summer patterns were used for fitting the model in region A: NAO, EA-JET and WP. The NAO and the EA-JET seem to be the most influential patterns in the number of storms there: they contribute to their increase. Since this region is over Iceland, it is somehow obvious that the NAO would have some kind of influence in the number of storms. As for the winter NAO, it influences the location of the storm tracks (Hurrell 1995). It also seems that the summer NAO influences the summer storm tracks.

According to Washington et al. (2000), the EA-JET is associated with summer melting in Svalbard. Therefore, the fact that the EA-JET was used in the regression equation for region A, may reflect the role played by the diabatic heating to the development of the summer storms in that area: the extra fresh water from the sea-ice melting. The WP was also used in the regression equation for region A. This pattern affects North America and it also shows some influence over Europe (Great Britain, France and Belgium, for example) (Figure 6.5) which are areas located within region A.

The track intensity of the summer storm tracks in region A do not present a trend (Table 7.1). The Atlantic Multidecadal Oscillation was used in the track intensity regression model for that sector. Therefore, the AMO index plays an important role in the summer storm tracks over the Atlantic. It was also identified over region B together with the summer NAO for the track density anomaly and it was used alone to model the track intensity variability in region A. Since the AMO reflects an interaction between ocean-atmosphere, convection and diabatic heating seem to play an important role in summer storms in the North Atlantic (sectors A and B).

One of the regions which is also worth mentioning here is region E. The difference between summer and winter storm track variables (explained in section 5.2, Chapter 5), showed a huge variation within sector E. The value of the summer season variables there seem to be higher than winter. It was also found that the trend in the track density anomaly was 1.33 storms per decade, which represents an increase of the average of 38.88% in 54 years[1].

The intensity has also increased in region E: 15.43% of the average in 54 years. Besides that, the ASU pattern was used in the fitted model. It is a pattern for Asia, but it is observed to affect the pole (Barnston and Livezey 1987) and it is also affected by the AO pattern[2] in late Spring. Since the AO affects the Arctic, and region E is located there, it seems to influence not only the ASU index, but it also contributes to the variability of the intensity of the summer storm tracks. According to Thompson and Wallace (1998), the AO pattern is similar to the NAO, they also proposed that “the zonally asymmetric surface air temperature and mid-troposphere circulation anomalies observed in association with the AO may be secondary baroclinic features induced by the land-sea contrasts.” Hence, the AO together with the ASU pattern are affecting sector E in a high proportion.

We speculate that the variability of the storm tracks over region E could be the result of a climate change[3]. That is, extra melting of sea-ice could influence the AO pattern in late Spring (Thompson and Wallace 1998; Gong and Ho 2003). The AO would, consequently, influence the ASU pattern in summer, which would give a signal

---

[1] See table 7.1.

[2] The AO in late spring has been found to shift the summertime upper tropospheric jet stream over east Asia.

[3] There may be other explanations, however, they would require extra added efforts which would go beyond the scope of this thesis.

to the summer storm tracks in region E. We have also hypothesized that the extra melting of sea-ice would provide extra energy input to the storm tracks due to the diabatic heating. If the storm tracks are self-maintained[4] (Hoskins and Valdes 1990), the diabatic heating would then contribute to an increase in their number, intensity and lifetime for that region as well. This is one effect that would explain the increased amount of storms and their intensity in 54 years.

7.4 Final Remarks

This thesis has provided a historic overview of the cyclogenesis theory, the Bergen School and the storm tracks. It has also shown the climatology of the extra-tropical summer storm in the Northern Hemisphere, in order to give a clearer picture of such kind of systems. After that, it focused on a more regional view of the storm tracks by considering three regions in the North Atlantic, and two in the Arctic. Finally, it presented the relation of the extra-tropical summer storm tracks to the large-scale flow and to the ocean-atmosphere interaction through the Sea Surface Temperature (AMO index).

This is a pioneer work in this area due to the void in the literature related to summer storm tracks. There are many other questions to be answered that may be considered for future work, for example: why storm tracks last longer during summer than winter; the energetics of extra-tropical summer storms; explore the idea that baroclinic instability may exist without a temperature gradient at the surface (as mentioned in subsection 2.2.1); the regeneration/rejuvenation of weak storms (Grønås et al. 1994; Bergeron 1950; Serreze 1995) and so on. It is hoped that this research may be a contribution to future research, for the improvement of GCMs and to the Atmospheric/Climatology science theory in general.

---

[4] See subsection 3.2.2.

Appendix A

The cost Function

The cost function is given by:

$$\Xi = \sum_{i=1}^{m} \sum_{k=2}^{n-1} D(\mathbf{P}_i^{k-1}, \mathbf{P}_i^{k}, \mathbf{P}_i^{k+1}) \tag{A.1}$$

where $D(\mathbf{P}_i^{k-1}, \mathbf{P}_i^{k}, \mathbf{P}_i^{k+1})$ is the local deviation at time step k, m the number of tracks and n the number of frames (time steps). The $\mathbf{P}_i^{k}$ represents the position of the vector in a Cartesian space. For the local deviation, the following assumptions are made:

$$D(\mathbf{P}_i^{k-1}, \mathbf{P}_i^{k}, \mathbf{P}_i^{k+1}) = \begin{cases} 0 & \text{(i)} \\ \psi(\mathbf{P}_i^{k-1}, \mathbf{P}_i^{k}, \mathbf{P}_i^{k+1}) & \text{(ii)} \\ \Psi & \text{(iii)} \end{cases} \tag{A.2}$$

where

(i) if $\mathbf{P}_i^{k-1}$ is a phantom feature point, and $\mathbf{P}_i^{k}$ and $\mathbf{P}_i^{k+1}$ are real or phantom;

(ii) if $\psi(\mathbf{P}_i^{k-1}, \mathbf{P}_i^{k}, \mathbf{P}_i^{k+1})$ are real feature points;

(iii) otherwise.

The term $\psi(\mathbf{P}_i^{k-1}, \mathbf{P}_i^{k}, \mathbf{P}_i^{k+1})$ is a measure of the change of speed and direction over three time steps and Ψ is a global upper bound on ψ, according to Hodges (1999).

Appendix B

The Normal Probability Plots

B.1 Checks for Normality

The regression models in this thesis assumed that the variables were normally distributed. The variables considered in the study were the track density anomaly and the track intensity. Even though the track density variable informs the number of tracks (as count data), it is, in this case, a measure of density: the number of storms over a region per season or month. Therefore, the values for the track density are given as continuous and not discrete values. In the model analysis, the anomaly of the track density was used instead as a means of transforming the data. Transformation of data is a normal practice in science, even for count data, as mentioned by Stephenson (2005):

> While a linear response is justifiable in many situations, there are also occasions when the response is not expected to be linear... Either you non-linearly transform the response variable... and then do a linear regression using the transformed response, or you non-linearly transform the fitted values, which are a linear combination of the explanatory variables... the square root transformation is useful for transforming positive and zero count data (e.g. number of storms) prior to linear regression.

This assumption is also confirmed by Chatfield (2004) who mentions that plotting the data "...may suggest that it is sensible to consider transforming them, for example, by taking logarithms or square roots."

A test for normality was also considered in order to confirm that the dataset used was normally distributed or not. One way to investigate this is to use a histogram to observe how skewed the dataset is or not. There is, though, a "better tool for assessing normality": the normal probability plot (Maindonald and Braun 2005). This method consists of:

(i) Sorting the data values;

(ii) Plotting the sorted data against the ordered values that might be expected if the data really were from a normal distribution;

(iii) If the data are from a normal distribution, the plot should approximate a straight line;

(iv) Finally, the plotted data can be compared to several probability plots of normal random data in order to check how much the original dataset has departed from these plots.

The results of such plots for the track density anomaly data, for the different regions investigated, are shown in the Appendix figures: B.1 (regions A,B and C) and B.2 (regions D and E). The upper right panel of the figures represent the normal probability plot for the track density anomaly data, whereas the remaining of the plots are for random samples from a normal distribution. This way the analyst may compare how much the original data has departed from a straight line and how much it has departed from other random samples that are normally distributed.

There is no obvious feature that distinguishes the plots in the upper right panel from the seven reference plots. Therefore, the linear regression model was chosen to study the track density anomaly and the intensity of the summer extra-tropical storm tracks.

The normal probability plots of the track intensity are shown in the Appendix figures: B.3 (regions A, B and C) and B.4 (regions D and E).

B.2 The Normal Probability Plots

Below are the normal probability plots used for testing if the datasets are normally distributed. The plots shown are for the track density anomaly and the track intensity.

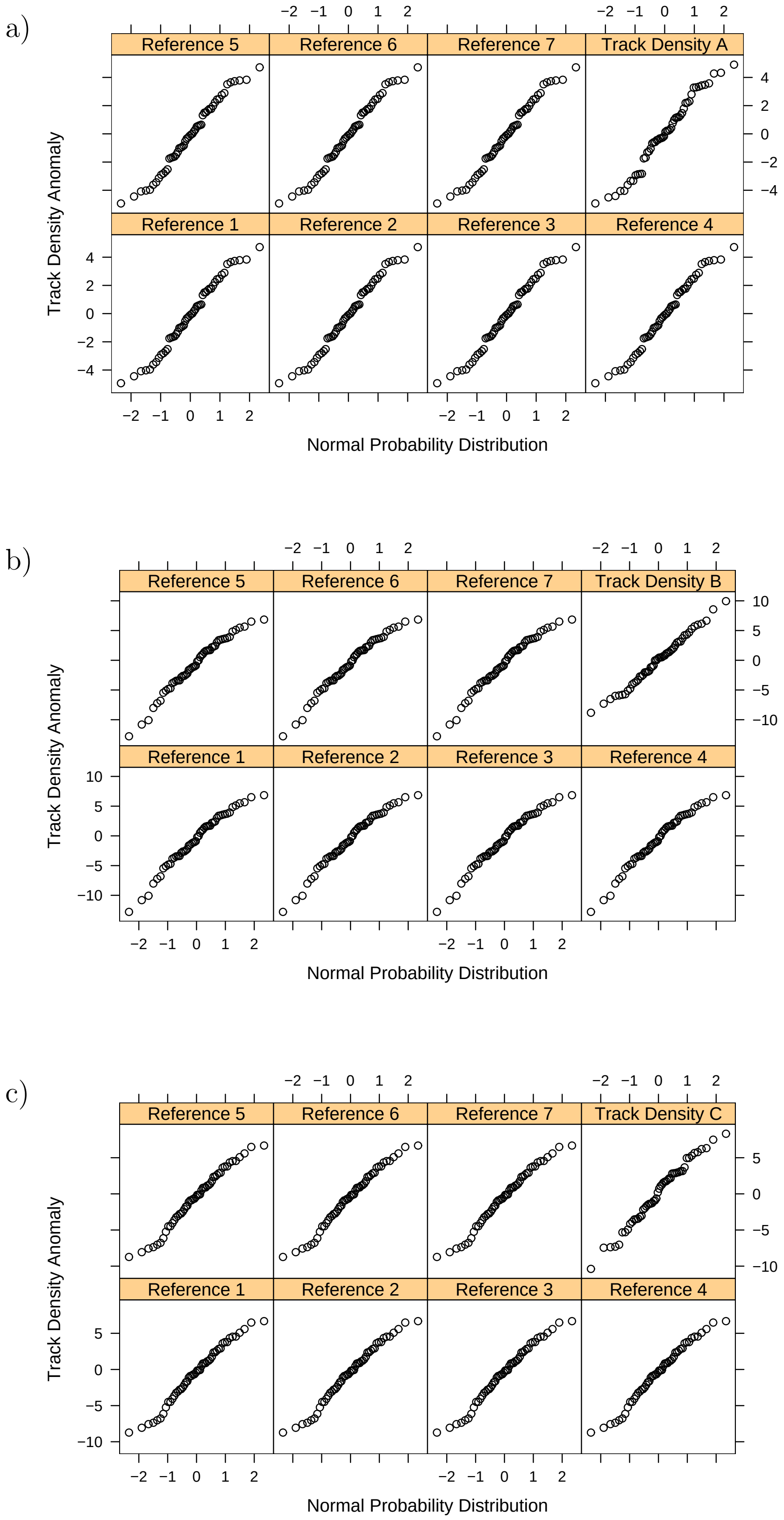

Figure B.1: *The upper right panel in each of the plots (a, b and c) is the normal probability plot for the track density anomaly in regions (a) A, (b) B and (c) C. Remaining panels show plots for samples from a normal distribution.*

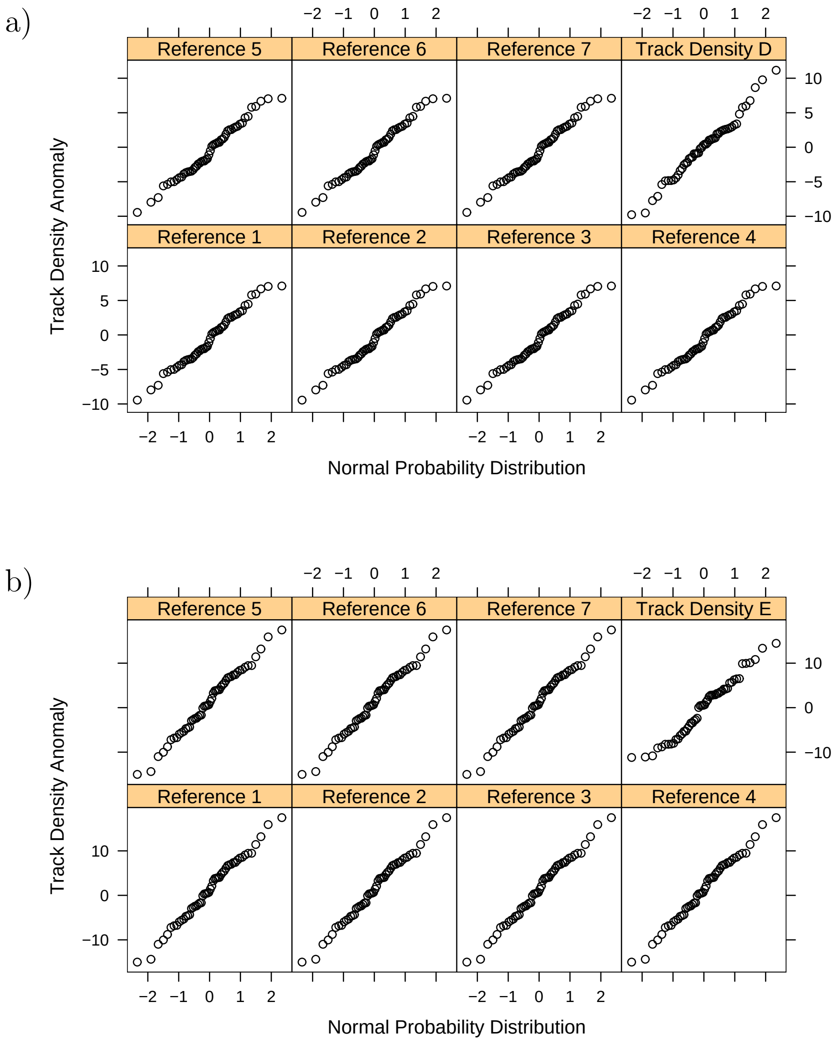

Figure B.2: *The upper right panel in each of the plots (a and b) is the normal probability plot for the track density anomaly in regions (a) D and (b) E. Remaining panels show plots for samples from a normal distribution.*

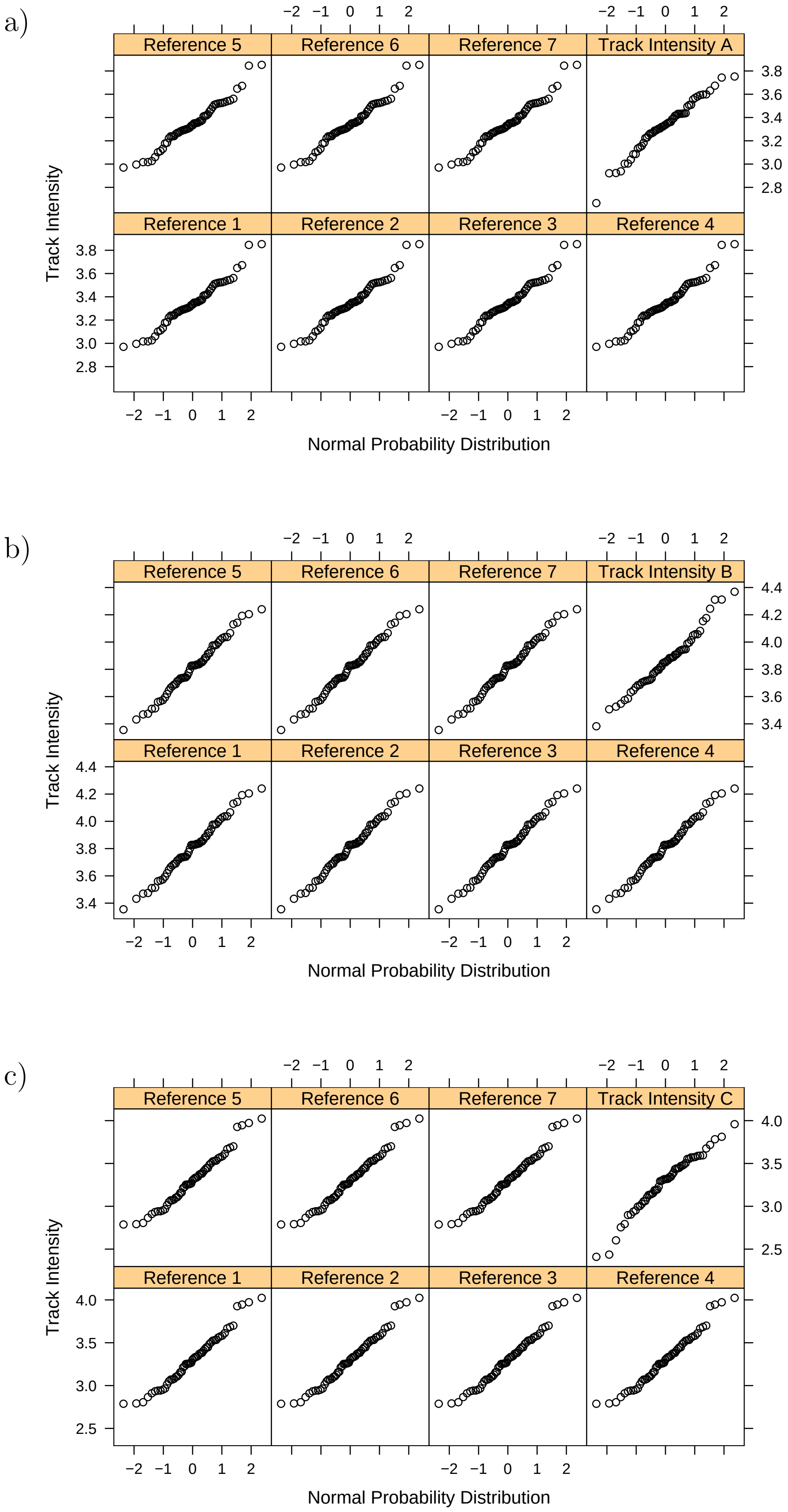

Figure B.3: *The upper right panel in each of the plots (a, b and c) is the normal probability plot for the track intensity in regions (a) A, (b) B and (c) C. Remaining panels show plots for samples from a normal distribution.*

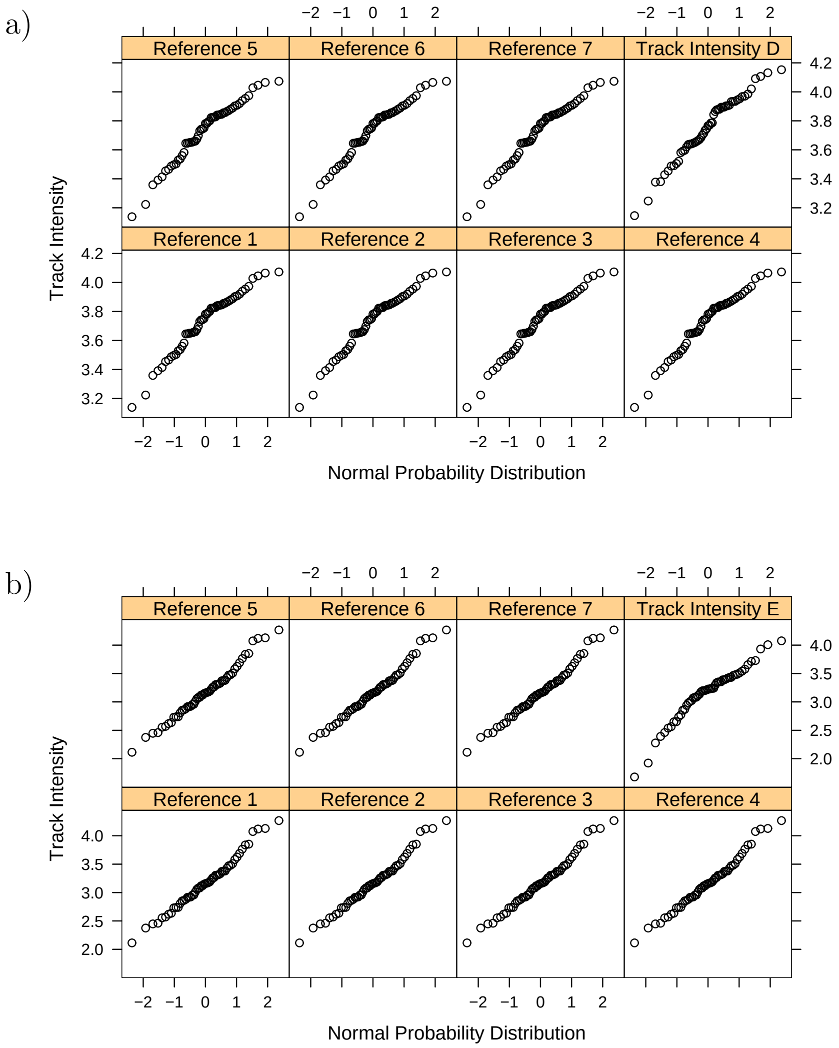

Figure B.4: *The upper right panel in each of the plots (a and b) is the normal probability plot for the track intensity in regions (a) D and (b) E. Remaining panels show plots for samples from a normal distribution.*

Appendix C

Criteria for Comparing the Regression Models: R^2 and the AIC

In order to choose the ‘best’ model, under a regression model analysis, some statistical parameters may be used. Among the several parameters available, two well-known are the R^2 and the AIC (Maindonald and Braun 2005; Chatfield 2004).

The R^2 statistic or ‘coefficient of determination’ is defined as the square of the correlation coefficient. It represents the sum of squares about the mean that is explained by the model, divided by the total sum of squares:

$$R^2 = \frac{Sum \quad of \quad Squares}{Total \quad Sum \quad of \quad Squares} \tag{C.1}$$

The value obtained may be multiplied by 100 to give the percent of the model power, that is, how much the model explains the variability in the case study. This parameter gives only a ‘crude’ estimation of the adequacy of the model. If the range of the explanatory variables are different, R^2 should be avoided for making comparisons between different models (Maindonald and Braun 2005).

A better parameter for making comparisons between models and selecting the best one is the Akaike’s Information Criterion (AIC). This is a more sophisticated criterion which is generally preferred (Chatfield 2004).

The AIC in the R statistical package is calculated as (Maindonald and Braun 2005):

(i) if the variance is known:

$$AIC = \frac{RSS}{\sigma^2} + 2p \tag{C.2}$$

(ii) if the variance is unknown:

$$AIC = \quad n \quad log(\frac{RSS}{n}) + 2p \tag{C.3}$$

where p is the number of parameters that have been fitted; RSS represents the residual sum of squares and n is the number of observations.

The AIC is designed to decrease as the estimated skill increases (Maindonald and Braun 2005), thus the selection is made by choosing the model which contains the smallest value of AIC, as Chatfield (2004) points out:

> A model-selection criterion gives a numerical-valued ranking of all models, so that the analyst can see whether there is a clear winner or, alternatively, several competing models.

Therefore, the AIC should not be used alone, but as a measure of comparison between the different AIC values of the different models. This criterion was applied to choose the 'best' regression models in this thesis, whereas the R^2 was used only to provide a rough estimation of the predictive power of the equations.

Appendix D

Average and Standard Deviation of the Main Variables

A summary of the variables presented in chapter 4 is shown here. The values are for the composite means and standard deviations only. The units of each variable are discussed in section 4.2.2.

Table D.1: Averages and standard deviations of the different variables in the different regions: JJA(1948-2002) and DJF(1949-2002).

		Reg. A		**Reg. B**		**Reg. C**		**Reg. E**		**Reg. E**	
		JJA	DJF	JJA	DJF	JJA	DJF	JJA	DJF	JJA	DJF
v1	$\overline{x}$	3.33	4.37	3.86	5.16	3.28	4.12	3.75	3.70	3.15	3.86
	σ	0.22	0.31	0.21	0.35	0.33	0.36	0.22	0.36	0.47	0.39
v2	$\overline{x}$	8.64	11.44	19.19	12.49	8.71	11.59	9.21	10.02	7.38	8.71
	σ	0.69	1.11	0.79	1.28	1.07	1.13	0.78	1.17	1.38	0.99
v3	$\overline{x}$	55.14	50.50	62.66	50.96	50.59	40.66	57.27	43.27	51.86	57.88
	σ	4.74	4.59	6.06	4.76	7.56	7.90	8.47	6.07	13.75	12.32
v4	$\overline{x}$	2.11	3.00	2.73	2.68	1.99	2.73	2.12	1.24	1.39	2.09
	σ	0.38	0.51	0.52	0.57	0.44	0.63	0.51	0.43	0.72	0.76
v5	$\overline{x}$	2.77	3.01	3.08	3.02	2.53	2.46	3.03	3.53	3.00	3.03
	σ	0.37	0.45	0.54	0.51	0.59	0.57	0.54	0.57	1.11	0.98
v6	$\overline{x}$	24.59	26.87	31.96	29.08	22.69	23.12	25.66	20.49	18.01	20.84
	σ	2.68	3.52	4.30	4.44	4.30	4.40	4.47	3.54	6.64	4.82
v7	$\overline{x}$	5.07	6.98	7.29	7.12	5.50	7.53	5.78	4.76	2.32	0.97
	σ	0.64	1.49	0.80	1.96	0.86	1.68	0.93	1.82	1.44	1.41
v8	$\overline{x}$	2.28	2.43	2.13	4.99	1.54	1.24	0.33	0.89	-1.19	-2.43
	σ	0.51	1.13	0.59	1.19	0.61	1.59	0.87	1.25	1.19	1.48
v9	$\overline{x}$	6.35	4.53	6.12	4.72	6.28	4.45	5.74	4.44	6.04	5.15
	σ	0.79	0.43	0.74	0.46	0.85	0.52	0.74	0.63	1.24	0.53
v10	$\overline{x}$	-0.05	-0.06	-0.02	-0.09	-0.03	-0.08	-0.05	-0.19	-0.07	-0.05
	σ	0.05	0.06	0.05	0.05	0.05	0.05	0.04	0.05	0.07	0.06
v11	$\overline{x}$	-0.007	-0.013	-0.002	-0.017	-0.006	-0.015	-0.007	-0.031	-0.010	-0.008
	σ	0.006	0.009	0.007	0.010	0.006	0.009	0.006	0.009	0.009	0.009

NB: The variable names are: v1 - Mean Intensity; v2 - Mean Speed; v3 - Feature Density; v4 - Genesis Density; v5 - Lysis Density; v6 - Track Density; v7 - Mean Longitudinal Velocity Component; v8 - Mean Latitudinal Velocity Component; v9 - Mean Lifetime; v10 - Mean growth/decay rate; v11 - Tendency. (See section 4.2.2 for reference on the variable descriptions and units).

Appendix E

Contributions of the Explanatory Variables to the Regression Models

Figures E.1, E.2 and E.3 show the contribution of individual terms of the regression fit for the track density anomaly equations (E.1 and E.2) and the track intensity ones (E.3). The $y-scale$ on these plots represent the scale of the linear predictor. The more inclined the curve is, the more its contribution to the regression fit. Ascending curves mean that the variable is making a large contribution, with probability of increasing the value of the regression equation as the variable goes from low to high values, and vice-versa for the descending curves (Maindonald and Braun 2005).

The partial residuals of the different elements which compose the equations were added to the plots, they are plotted as dots. The importance of these plots are to identify which elements in the multiple regression equations play an important role when compared to one another. They also inform, for the purpose of this thesis, how the large-scale flow is related to the storm track density anomaly and intensity.

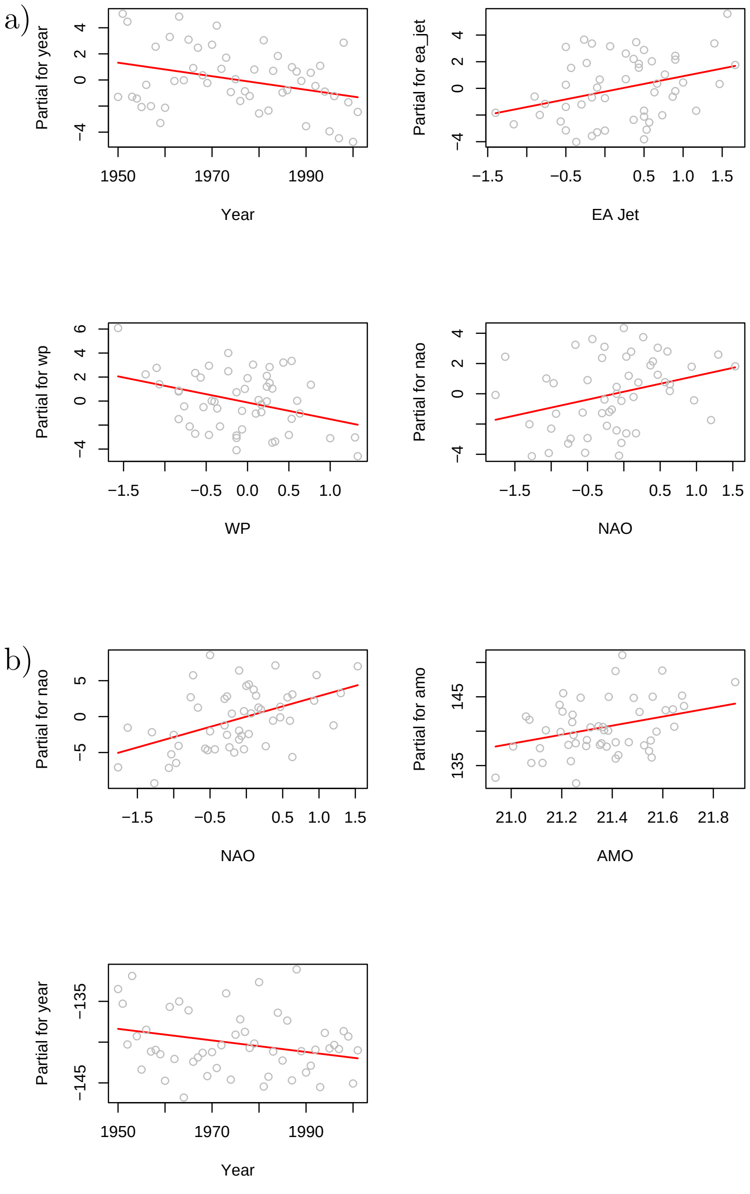

Figure E.1: *Plots showing the contributions of the individual terms (explanatory variables) to the track density anomaly regression fit of the equations for regions: (a) A and (b) B. The dots represent the partial residuals of the fitted values.*

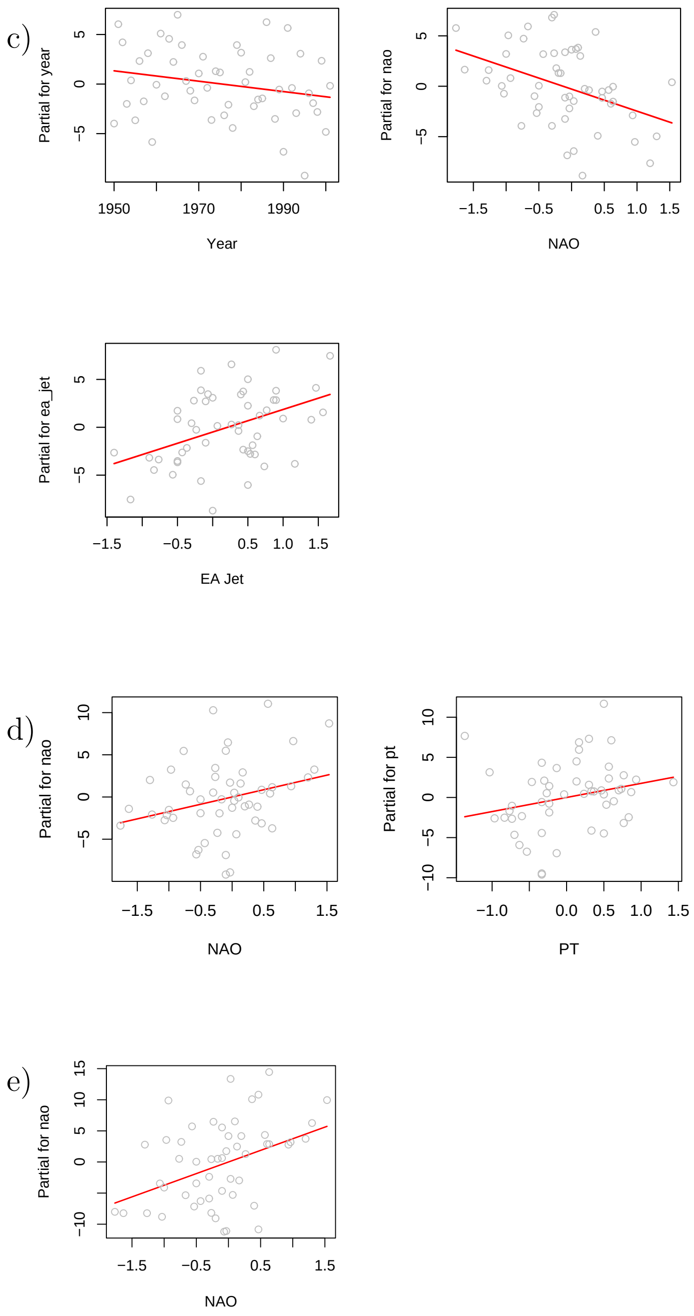

Figure E.2: *Plots showing the contributions of the individual terms (explanatory variables) to the track density anomaly regression fit of the equations for regions: (c) C; (d) D and (e) E. The dots represent the partial residuals of the fitted values.*

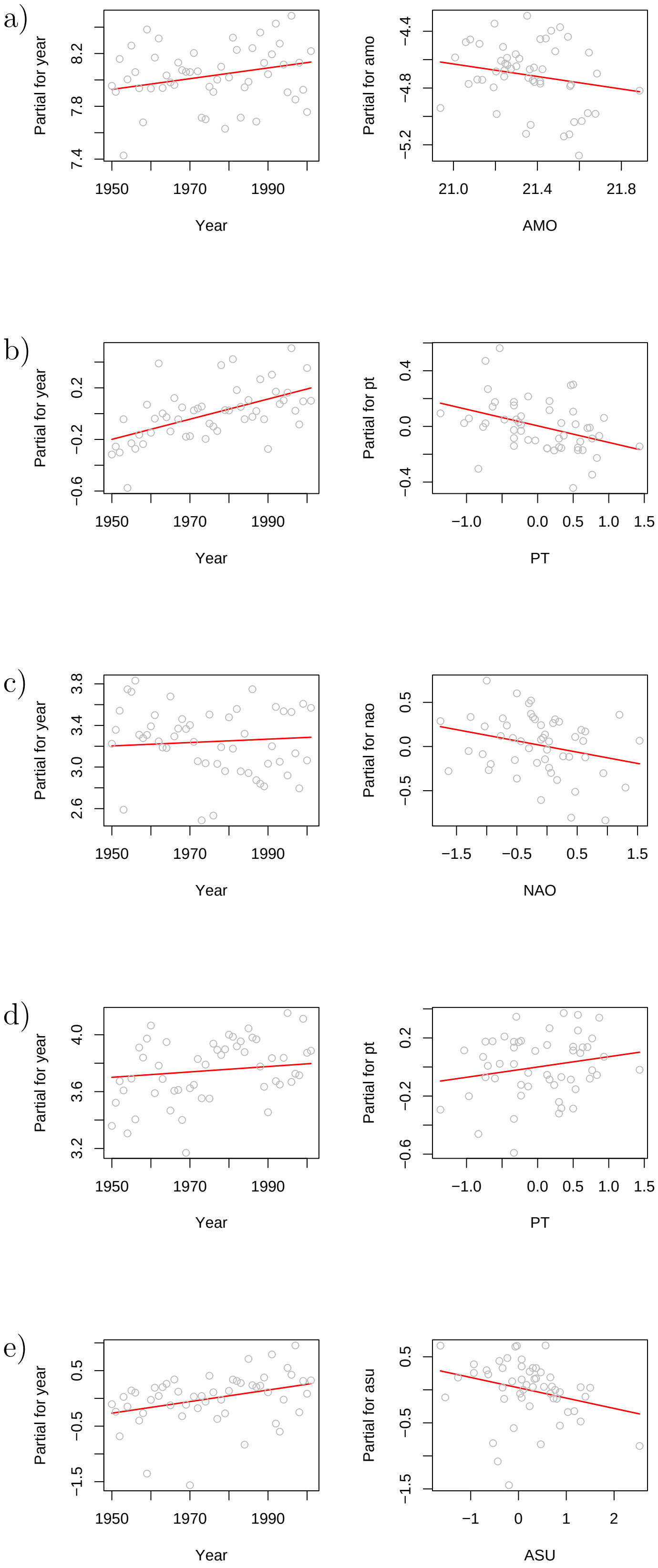

Figure E.3: *Plots showing the contributions of the individual terms (explanatory variables) to the track intensity regression fit of the equations for regions: (a) A; (b) B; (c) C; (d) D and (e) E. The dots represent the partial residuals of the fitted values.*

Appendix F

Statistically Significant Regression Models

The list of regression models which were statistically significant at the 95% confidence interval are presented here. They are related to the explanations given in chapter 6, section 6.3. First, the track density anomaly models for each region are shown. Then the models related to the track intensity will be presented. The selection of the 'best' model for each region, explained in chapter 6, was based on the lowest AIC number. See Appendix C for more information on the difference between the AIC and the R^2.

F.1 Track Density Anomaly

The fitted models for the track density anomaly are presented below, where β represents the coefficient estimates; $\widehat{TD}$ is the expected track density regression model; p denotes the amplitude of the actual mode and i is the year index.

Region A

Table F.1: The track density anomaly models for region A.

Model no.	Regression Equation	p-value	AIC	R^2
1	$\widehat{TD}_i = \beta_0 + \beta_1 p_{wp_i}$	0.03	97.15	9.2%
2	$\widehat{TD}_i = \beta_0 + \beta_1 p_{eajet_i} + \beta_2 p_{wp_i}$	0.03	97.05	12.8%
3	$\widehat{TD}_i = \beta_0 + \beta_1 p_{eajet_i} + \beta_2 p_{wp_i} + \beta_3 p_{nao_i}$	0.02	96.07	17.7%
4	$\widehat{TD}_i = (nointercept) + \beta_1 p_{eajet_i} + \beta_2 p_{wp_i} + \beta_3 p_{nao_i}$	0.04	95.55	12.0%
5	$\widehat{TD}_i = \beta_0 + \beta_1 p_{eajet_i} + \beta_2 p_{wp_i} + \beta_3 p_{nao_i} + \beta_4 year_i$	0.007	92.78	25.6%

Region B

Table F.2: The track density anomaly models for region B.

Model no.	Regression Equation	p-value	AIC	R^2
1	$\widehat{TD}_i = \beta_0 + \beta_1 p_{nao_i}$	0.008	146.48	13.2%
2	$\widehat{TD}_i = \beta_0 + \beta_1 p_{amo_i} + \beta_2 p_{nao_i}$	0.001	141.24	24.5%
3	$\widehat{TD}_i = (nointercept) + \beta_1 p_{amo_i} + \beta_2 p_{nao_i}$	0.03	146.46	13.3%
4	$\widehat{TD}_i = (nointercept) + \beta_1 p_{amo_i} + \beta_2 p_{nao_i} + \beta_3 year_i$	0.002	139.97	26.3%

Region C

Table F.3: The track density anomaly models for region C.

Model no.	Regression Equation	p-value	AIC	R^2
1	$\widehat{TD}_i = \beta_0 + \beta_1 p_{eajet_i}$	0.001	144.79	18.5%
2	$\widehat{TD}_i = \beta_0 + \beta_1 p_{nao_i}$	< 0.001	141.76	23.2%
3	$\widehat{TD}_i = \beta_0 + \beta_1 p_{nao_i} + \beta_2 p_{eajet_i}$	< 0.001	136.19	33.6%
4	$\widehat{TD}_i = (nointercept) + \beta_1 p_{nao_i} + \beta_2 p_{eajet_i}$	< 0.001	136.3	30.8%
5	$\widehat{TD}_i = \beta_0 + \beta_1 p_{nao_i} + \beta_2 year_i$	0.001	143.23	23.9%
6	$\widehat{TD}_i = \beta_0 + \beta_1 p_{nao_i} + \beta_2 p_{eajet_i} + \beta_3 year_i$	< 0.001	135.72	36.7%
7	$\widehat{TD}_i = (nointercept) + \beta_1 p_{nao_i} + \beta_2 p_{eajet_i} + \beta_3 year_i$	< 0.001	136.15	33.6%
8	$\widehat{TD}_i = \beta_0 + \beta_1 p_{nao_i} + \beta_2 p_{wp_i}$	0.001	143.00	24.3%

Region D

Table F.4: The track density anomaly models for region D.

Model no.	Regression Equation	p-value	AIC	R^2
1	$\widehat{TD}_i = \beta_0 + \beta_1 p_{nao_i}$	0.04	154.51	7.8%
2	$\widehat{TD}_i = (nointercept) + \beta_1 p_{nao_i}$	0.05	152.66	7.6%
3	$\widehat{TD}_i = \beta_0 + \beta_1 p_{nao_i} + \beta_2 p_{pt_i}$	0.03	153.26	13.4%
4	$\widehat{TD}_i = (nointercept) + \beta_1 p_{nao_i} + \beta_2 p_{pt_i}$	0.03	151.35	13.3%

Region E

Table F.5: The track density anomaly models for region E.

Model no.	Regression Equation	p-value	AIC	R^2
1	$\widehat{TD}_i = \beta_0 + \beta_1 year_i$	0.05	195.77	7.3%
2	$\widehat{TD}_i = \beta_0 + \beta_1 p_{nao_i}$	0.002	189.73	17.5%
3	$\widehat{TD}_i = (nointercept) + \beta_1 p_{nao_i}$	0.002	188.05	16.9%
4	$\widehat{TD}_i = \beta_0 + \beta_1 p_{nao_i} + \beta_2 year_i$	0.002	188.81	22.0%
5	$\widehat{TD}_i = (nointercept) + \beta_1 p_{nao_i} + \beta_2 year_i$	0.008	189.72	17.5%
6	$\widehat{TD}_i = \beta_0 + \beta_1 p_{nao_i} + \beta_2 p_{amo_i} + \beta_3 year_i$	0.005	189.72	23.6%
7	$\widehat{TD}_i = (nointercept) + \beta_1 p_{nao_i} + \beta_2 p_{amo_i} + \beta_3 year_i$	0.005	188.33	22.7%

F.2 Track Intensity

The fitted models for the track intensity are presented below, where β represents the coefficient estimates; $\widehat{TI}$ is the expected track intensity regression model; p denotes the amplitude of the actual mode and i is the year index.

Region A

Table F.6: Track intensity models for region A.

Model no.	Regression Equation	p-value	AIC	R^2
1	$\widehat{TI}_i = \beta_0 + \beta_1 p_{amo_i}$	0.05	-155.65	7.2%
2	$\widehat{TI}_i = (nointercept) + \beta_1 p_{amo_i}$	< 0.001	-149.23	99.5%
3	$\widehat{TI}_i = (nointercept) + \beta_1 p_{amo_i} + \beta_2 year_i$	< 0.001	-155.96	99.6%

Region B

Table F.7: Track intensity models for region B.

Model no.	Regression Equation	p-value	AIC	R^2
1	$\widehat{TI}_i = \beta_0 + \beta_1 year_i$	< 0.001	-171.26	23.4%
2	$\widehat{TI}_i = \beta_0 + \beta_1 p_{wp_i} + \beta_2 year_i$	< 0.001	-172.15	27.6%
3	$\widehat{TI}_i = \beta_0 + \beta_1 p_{pt_i} + \beta_2 year_i$	< 0.001	-177.27	34.4%
4	$\widehat{TI}_i = (nointercept) + \beta_1 p_{pt_i} + \beta_2 year_i$	< 0.001	-167.60	99.8%

Region C

Table F.8: Track intensity model for region C.

Model no.	Regression Equation	p-value	AIC	R^2
1	$\widehat{TI}_i = \beta_1 p_{nao_i} + \beta_2 year_i$	< 0.001	-114.36	99.04%

Region D

Table F.9: Track intensity models for region D.

Model no.	Regression Equation	p-value	AIC	R^2
1	$\widehat{TI}_i = (nointercept) + \beta_1 p_{amo_i}$	< 0.001	-154.37	99.7%
2	$\widehat{TI}_i = (nointercept) + \beta_1 p_{eajet_i}$	0.03	135.09	8.4%
3	$\widehat{TI}_i = (nointercept) + \beta_1 p_{pt_i} + \beta_2 year_i$	< 0.001	-159.79	99.7%

Region E

Table F.10: Track intensity models for region E.

Model no.	Regression Equation	p-value	AIC	R^2
1	$\widehat{TI}_i = (nointercept) + \beta_1 p_{amo_i}$	< 0.001	-79.23	98.0%
2	$\widehat{TI}_i = (nointercept) + \beta_1 p_{eajet_i}$	0.04	119.14	7.8%
3	$\widehat{TI}_i = \beta_0 + \beta_1 p_{asu_i} + \beta_2 year_i$	0.03	-83.32	13.3%
4	$\widehat{TI}_i = (nointercept) + \beta_1 p_{amo_i} + \beta_2 year_i$	< 0.001	-81.39	98.1%

References

Akyildiz, V. (1984). Systematic errors in the behaviour of cyclones in the ecmwf operational models. *Tellus 37A*, 297–308.

Anderson, D., K. I. Hodges, and B. J. Hoskins (2003, March). Sensitivity of feature-based analysis methods of storm tracks to the form of background field removal. *American Meteorological Society 131*, 565–573.

Barnston, A. G. and R. E. Livezey (1987). Classification, seasonality and persistence of low frequency atmospheric circulation patterns. *Mon. Wea. Rev.* (115), 1083–1126.

Barry, R. and A. Carleton (2001). *Synoptic and Dynamic Climatology.* New York: Routledge.

Bergeron, T. (1950). *De Tropiska Orkanernas Problem.* Stockolm: Kungl. Boktr. P. A. Norstedt & Söner.

Bluestein, H. B. (1993). *Synoptic-Dynamic Meteorology in Midlatitudes*, Volume II. New York: Oxford University Press.

Branscome, L., W. Gutowski, and D. Stewart (1989). Effects of surface fluxes on the nonlinear development of baroclinic waves. *J. Atmos. Sci. 46*, 460–475.

Broch, J. T. (1981). *Principles of Analog and Digital Frequency Analysis.* Tapir.

Byrkjedal, O. (2002, June). Stormbaner ved ulikt isdekke i labradorhavet. Master's thesis, Universitetet i Bergen, Bergen.

Cai, M. and H. van der Dool (1991). Low-frequency waves and traveling storm tracks. i. barotropic component. *J. Atmos. 48*, 1420–36.

Carlson, T. (1991). *Mid-Latitude Weather Systems.* London: Routledge.

Chang, E. (2004). Are the northern hemisphere winter storm tracks significantly correlated. *American Meteorological Society 17*, 4230–4244.

Chang, E. and I. Orlanski (1992). On the dynamics of a storm track. *Journal of the Atmospheric Sciences* (50), 999–1015.

Chang, E. K. and Y. Fu (2002). Interdecadal variations in northern hemisphere winter storm track intensity. *American Meteorological Society 15*, 642–658.

Chang, E. K. M., S. Lee, and K. L. Swanson (2002). Storm tracks dynamics. *J. Climate 15*(16), 2163–2183.

Chatfield, C. (2004). *The Analysis of Time Series: An Introduction* (6th ed.). Texts in Statistical Science. New York: Chapman & Hall/CRC.

Endlich, R. M., D. E. Wolf, D. J. Hall, and A. E. Brain (1971). Use of a pattern recognition technique for determining cloud motions form sequences of satellite photographs. *J. Appl. Meteor. 10*, 105–107.

Gong, D.-Y. and C.-H. Ho (2003). Arctic oscillation signals in the east asian summer monsoon. *Journal of Geophysical Research 108*(D2 - 4066), ACL 14–1:14–6.

Grønås, S. (2005). Vilhelm bjerknes′ vision for scientific weather prediction. Paper given by Prof. Grønås in the subject Introduction to Methods in Weather Forecasting (GEOF321 - Spring).

Grønås, S., N. G. Kvamstø, and E. Raustein (1994). Numerical simulation of the northern germany storm of 27-28 august 1989. *Tellus 46A*, 635–650.

Gulev, S., O. Zolina, and S. Grigoriev (2001). Extratropical cyclone variability in the northern hemisphere winter from the ncep/ncar reanalysis data. *Climate Dynamics* (17), 795–809.

Guterl, F. (2005, September 26 / October 3). Are more katrinas in our future? Newsweek Magazine.

Hansen, G. and T. Svenoe (2005). Multilinear regression analysis of the 65-year tromso total ozone series. *Journal of Geophysical Research-Atmospheres 110*(D10). D10103.

Hartmann, D. (1994). *Global Physical Climatology*, Volume 56 of *International Geophysics Series*. London: Academic Press.

Hodges, K. (1994). A general method for tracking analysis and its application to meteorological data. *Monthly Weather Review* (122), 2573–2586.

Hodges, K. (1995). Feature tracking on the unit sphere. *Monthly Weather Review* (123), 3458–3465.

Hodges, K. (1996). Spherical nonparametric estimates applied to the ugamp model integration for amip. *Monthly Weather Review* (124), 2914–2932.

Hodges, K. (1999). Adaptive constraints for feature tracking. *Monthly Weather Review* (127), 1362–1373.

Holton, J. (2004). *An Introduction to Dynamic Meteorology* (fourth ed.). International Geophysics Series. London,UK: Elsevier Academic Press.

Hoskins, B. and K. Hodges (2002). New perspectives on the northern hemisphere winter storm-tracks. *J. Atmos. Sci.* (59), 1041–1061.

Hoskins, B. and P. Valdes (1990). On the existence of storm tracks. *J. Atmos.* (47), 1854–1864.

Hurrell, J. W. (1995). Decadal trends in the north-atlantic oscillation - regional temperatures and precipitation. *Science 269*(5224), 676–679.

Jones, D. and I. Simmonds (1993). A climatology of southern hemisphere extratropical cyclones. *Clim. Dynam. 9*, 131–45.

Kalnay, M. K., R. Kistler, W. Collins, D. Deaven, L. Gandin, M. Iredell, S. Saha, G. White, J. Woollen, Y. Zhu, M. Chelliah, W. Ebisuzaki, W. Higgins, J. Janowiak, K. Mo, C. Ropelewski, J. Wang, A. Leetmaa, R. Reynolds, R. Jenne, and D. Joseph (1996). The ncep/ncar 40-year reanalysis project. *Bulletin of the American Meteorological Society* (77), 437–471.

Key, J. and A. Chan (1999). Multidecadal global and regional trends in 1000 mb and 500 mb cyclone frequencies. *Geophys. Res. Lett. 26*(14), 2053–6.

Kistler, R., E. Kalney, W. Collins, S. Saha, G. White, J. Woollen, M. Chelliah, W. Ebisuzaki, M. Kanamitsu, V. Kousky, H. van den Dool, R. Jenne, and M. Fiorino (2001). The ncep-ncar 50-year reanalysis: Monthly means cd-rom and documentation. *Bulletin of the American Meteorologica Society* (82), 247–267.

Klein, W. (1957). Principal tracks and mean frequencies of cyclones and anticyclones in the northern hemisphere. *US Weather Bureau* (Res. Paper 40), 60 pp.

Kristjansson, J. (1990). Model simulations of an intense meso-beta scale cyclone. the role of condensation parameterization. *Tellus 42A*, 78–91.

Lamb, H. (1991). *Historic Storms of the North Sea, British Isles and Northwest Europe*. Cambridge: The Press Syndicate of the University of Cambridge.

Lee, W. and M. Mak (1996). The role of orography in the dynamics of storm tracks. *J. Atmos. Sci. 53*, 1737–1750.

Maindonald, J. and J. Braun (2005). *Data Analysis and Graphics Using R: an Example-based Approach*. Cambridge Series in Statistical and Probabilistic Mathematics. New York: Cambridge University Press.

Meier, W., J. Stroeve, F. Fetterer, and K. Knowles (2005, September). Reductions in arctic sea ice cover no longer limited to summer. *EOS 86*(36), 326.

Murray, R. and I. Simmonds (1991). A numerical scheme for tracking cyclone centres from digital data. *Austral. Met. Mag. 39*, 155–66,167–80.

NOAA. Teleconnection pattern calculation procedures.

NOAA-CIRES (2004, September, 2004). Climate indices: Monthly atmospheric and ocean time series.

NOAA-CPC (2005). National weather service: Climate prediction center - introduction. Retrieved April 27th, 2006, from *http : //www.cpc.ncep.noaa.gov/data/teledoc/teleintro.shtml.*

Orlanski, I. and J. Katzfey (1991). The life cycle of a cyclone wave in the southern hemisphere. *J. Atmos. Sci. 48*, 1972–1998.

Overpeck, J., M. Sturm, J. Francis, D. Perovich, M. Serreze, R. Benner, E. Carmack, F. Chapin III, S. Gerlach, L. Hamilton, L. Hinzman, M. Holland, H. Huntington, J. Key, A. Lloyd, G. MacDonald, J. Fadden, D. Noone, T. Prowse, P. Schlosser, and C. Vörösmarty (2005, August). Arctic system on trajectory to new, seasonally ice-free state. *EOS 86*(34), 309,312.

Petterssen, S. (1950). Some aspects of the general circulation of the atmosphere. *Centen. Proc. Roy. Met. Soc.*, 120–55. London.

Rogers, J. C. (1990). Patterns of low-frequency monthly sea-level pressure variability (1899-1986) and associated wave cyclone frequencies. *Journal of Climate 3*(12), 1364–1379.

Serreze, M. (1995). Climatological aspects of cyclone development and decay in the arctic. *Atmosphere-Ocean 33*, 1–23.

Serreze, M., J. Box, R. Barry, and J. Walsch (1993). Characteristics of arctic synoptic activity. *Met. Atmos. Phys. 51*, 147–64.

Serreze, M., J. Maslanik, R. Preller, and R. Barry (1990). Sea ice concentrations in the canada basin during 1988: Comparisons with other years and evidence of multiple forcing mechanisms. *J. Geophys. Res. 95*(C12), 22253–67.

Sinclair, M. (1994). An objective cyclone climatology for the southern hemisphere. *Mon. Wea. Rev. 122*, 2239–2256.

Smith, B. (2002). Effects of a severe summer storm at serc. *Smithsonian Environmental Research Center 9*, 1,5–6. Newsletter.

Sorteberg, A., N. G. Kvamstø, and O. Byrkjedal (2004). Wintertime nordic seas cyclone variability and its impact on oceanic volume transports into the nordic seas.

Stephenson, D. B. (2005). Data analysis methods in weather and climate research.

Sutton, R. T. and D. L. Hodson (2005, May). Atlantic ocean forcing of north american and european summer climate. Paper submitted to Science magazine.

Thompson, D. W. J. and J. M. Wallace (1998). The arctic oscillation signature in the wintertime geopotential height and temperature fields. *Geophysical Research Letters 25*(9), 1297–1300.

Uccellini, L. (1990). Processes contributing to the rapid development of extratropical cyclones. extratropical cyclones. In *The Erik Palmn memorial volume*, pp. 81–106. Boston: Amer. Meteor. Soc.

Wallace, J. and M. Blackmon (1983). Observations of low-frequency atmospheric variability. In B. Hoskins and R. Pearce (Eds.), *Large-scale Dynamical Processes in the Atmosphere*, pp. 55–94. London: Academic Press.

Wallace, J. and D. S. Gutzler (1981). Teleconnections in the geopotential height field during the northern hemisphere winter. *Mon. Wea. Rev. 19*, 784–812.

Walpole, R., R. Myers, S. Myers, and K. Ye (2002). *Probability & Statistics for Engineers & Scientists* (Seventh edition ed.). Upper Saddle River, New Jersey: Prentice Hall.

Washington, R., A. Hodson, E. Isaksson, and O. MacDonald (2000). Northern hemisphere teleconnection indices and the mass balance of svalbard glaciers. *International Journal of Climatology 20*(5), 473–487.

Whittaker, L. and L. Horn (1984). Northern hemisphere extratropical cyclone activity for four mid-season months. *J. Climatol. 4*(3), 297–310.

Williams, B. J. I. (2002). Weather magic. PageWise. Retrieved June 19th, 2004, from $http://momo.essortment.com/weathermagic\_rmqf.htm.$

Xie, L., T. Z. Yan, L. J. Pietrafesa, J. M. Morrison, and T. Karl (2005). Climatology and interannual variability of north atlantic hurricane tracks. *Journal of Climate 18*(24), 5370–5381.